

Muthu, Priya., Study of Cross bridge Kinetics in Hypertrophic Ventricular Muscle. Doctor of Philosophy (Biochemistry and Molecular Biology), May, 2009, 185 pp, 8 tables, 64 illustrations, 102 bibliography.

Cardiovascular diseases are the leading cause of mortality worldwide; with heart failure being highly prevalent in most affluent parts of the world. There is a need for a better understanding of the mechanism underlying these diseases. Familial hypertrophic cardiomyopathy (FHC), one such disease, is a genetic disorder of the heart characterized by increased growth or hypertrophy in the thickness of the wall of the left ventricle, the largest of the four chambers of the heart. This research project is focused on one kind of FHC, the D166V mutation in the regulatory light chain in myosin, which is associated with a particularly malignant form of the disease. The overall goal of this project was to study cross bridge kinetics (contraction and ATP utilization) in cardiac muscle from transgenic mice and to develop assays to apply this to human samples.

The real time orientation changes of myosin and actin during a single cross bridge cycle beginning in a state of rigor was studied by Fluorescence anisotropy. Rabbit psoas fibers were isolated and used to achieve imaging of a few fluorophores or cross bridges. This technique was then applied to study cardiac myofibrils from transgenic mice, carrying the mutation causing the disease (FHC). Methods to achieve single molecule detection to aid studying

human samples suffering from this disease were developed using silver island films, monolayers of nanoparticles and surface plasmon coupled emission.

The conclusions of this dissertation were that a mutation in a light chain in myosin cause changes in the cross bridge kinetics. Myofibrils from the mutated mice displayed a significant slower rate of detachment during contraction as well as increased ATPase activity, which if severe enough could cause the heart to compensate by increasing wall thickness (hypertrophy).

Despite significant clinical advances in the treatment of various cardiovascular diseases, mortality rates remain high. No therapy currently exists to treat or delay progression from hypertrophy to heart failure. This proposal help answer an important question regarding the molecular basis of FHC-mediated pathology in the heart. Also, achieving imaging of a single fluorophore has numerous implications in the biological field, like studying ligand-receptor interactions in live cells, involvement of protein molecules in internalization of bacteria by cells, monitoring the conformational fluctuations of DNA, diagnosis of prion diseases and also in detection of viruses at an early phase of infection.

STUDY OF CROSS BRIDGE KINETICS IN HYPERTROPHIC VENTRICULAR MUSCLE

DISSERTATION

Presented to the Graduate Council of the
Graduate School of Biomedical Science
University of North Texas
Health Science Center at Fort Worth
in Partial Fulfillment of the Requirements

For the Degree of
Doctor of Philosophy

By

Priya Muthu, M.S

Fort Worth, Texas

May 2009

ACKNOWLEDGEMENTS

As I write my acknowledgement, I realize how many people have contributed to my PhD project – not all of whom I can do full justice here. Without their help, I certainly wouldn't have been able to complete this thesis.

First and foremost, I thank my advisor, Dr. Julian Borejdo for his supervision, advice, and guidance from the very early stage of this research. He supported me throughout my project, with his pool of patience and knowledge, whilst allowing me the room to work in my own way. His true scientist intuition and genius has made him a constant oasis of ideas and passion in science, which never ceased to inspire and enrich my growth as a student. I could never wish for a better or friendlier supervisor.

I gratefully acknowledge the members of my committee - Drs. Harlan Jones, Ladislav Dory, Ignacy Gryczynski, and my university member, Dr. Patricia Gwartz for their valuable advice and time. Their comments and suggestions inspired and directed my research. Special thanks to Prasad Mettikola, Rafal Luchowski, Nils Calander and Irina Akopova for all their help and support throughout my project. I would also like to thank all the members of CCFT for their valuable discussions and encouragement and all those beautiful memories. I am also sincerely grateful to Dr. Szczesna and her lab members for their willingness in providing us with samples and readiness in answering all our doubts and questions.

I would like to express my love and gratitude to my parents for always being my inspiration. I am the person I am today because of them, their unconditional love. I can't thank

them enough for all the support, and for all the opportunities they have afforded me I cannot write enough about my sister, Narmada, for being there whenever I needed a friend around. Words fail me to express my appreciation of my fiancé, Sarang, who has always been there supporting me with every step I took. Thank you for being my best friend and for the love and persistent confidence in me.

I would like to thank all my friends. Each one of them has played a very important role in my life and to the successful realization of this thesis.

Last but not the least; I would like to thank God for giving me this opportunity to do my PhD and blessing me through every step in life.

TABLE OF CONTENTS

ACKNOWLEDGEMENTS.....	iii
TABLE OF CONTENTS.....	v
LIST OF ILLUSTRATIONS.....	vi
LIST OF TABLES.....	xi
LIST OF ABBREVIATIONS.....	xii
CHAPTER	
1. INTRODUCTION TO THE STUDY.....	1
2. MATERIALS AND METHODS.....	25
3. CENTRAL HYPOTHESIS AND SPECIFIC AIMS.....	41
4. STUDY OF CROSS BRIDGE KINETICS IN HEALTHY MUSCLE.....	43
5. UNDERSTANDING THE MOLECULAR MECHANISMS INVOLVED IN CARDIAC MUSCLE.....	89
6. DEVELOPING METHODS TO IMAGE SINGLE MOLECULE IN BIOLOGICAL SYSTEMS.....	113
7. CONCLUSION.....	173
REFERENCES.....	179

LIST OF ILLUSTRATIONS

Chapter I

Figure 1. Sarcomeric proteins associated with FHC.....	4
Figure 2. Schematic representation of D166V mutation in myosin RLC.....	8
Figure 3. Skeletal muscle at increasing magnification.....	10
Figure 4. Myosin structure	12
Figure 5. Cross bridge cycle.....	15
Figure 6. Orientation signal from a single cross-bridge	17
Figure 7. Schematic showing why it is crucial to measure kinetics of single heads.....	19
Figure 8. Principle of total internal fluorescence reflection	21
Figure 9. Concept behind SPCE microscope	23

CHAPTER II

Figure 1. Prismless confocal SPCE microscope.....	32
---	----

Chapter IV

Figure 1. Calculated relative detected intensity from a point-like fluorescent sphere.....	54
Figure 2. Defining area on the sample plane conjugate to image plane	55
Figure 3. Polarization signal obtained from oriented PVA film	56

Figure 4. Calibration curve used to estimate the number of fluorescent cross-bridges in the detection volume	57
Figure 5. TIRF image of myofibril in rigor	58
Figure 6. Polarization signal obtained from rigor (A) and contracting (B) myofibril.....	59
Figure 7. Average polarization excess power spectra and t-test significance level.....	60
Figure 8. Cross-linked myofibrils in rigor solution and after adding contracting solution.....	61
Figure 9. Comparison of polarized intensities and polarization of fluorescence	74
Figure 10. Decay of anisotropy of fluorescein phalloidin and fluorescein phalloidin bound to F-actin.....	75
Figure 11. The time course of photobleaching of heavily labeled rigor myofibril.....	76
Figure 12. Time course of photobleaching of contracting myofibril: 3 fluorophores	77
Figure 13. Time course of photobleaching of contracting myofibril: 1 fluorophore.....	78
Figure 14. Histogram of the peak frequencies of the first 40 s of signals of contracting muscle.....	79
Figure 15. Polarized intensity of actin	80
Figure 16. Histogram of the times anisotropy of actin was high.....	81

Chapter V

Figure 1. A typical Tg-D166V cardiac myofibril during contraction	99
Figure 2: Image of a myofibril in rigor labeled with fluorescent phalloidin.....	100
Figure 3. Oscillation of fluorescence intensity of single actin molecule in contracting myofibril.....	101

Figure 4. Histogram of times during which intensities were high and histogram of durations of cycle in Tg-WT muscle	102
Figure 5. Oscillation of intensity of actin molecule contracting Tg-D166V cardiac myofibril.....	103
Figure 6. Histogram of times during which intensities were high and histogram of durations of cycle in Tg-D166V muscle	104
Figure 7. Time course of polarized intensity of contracting and rigor myofibril	105
Figure 8. Correlation function of contracting and rigor myofibril in WT myofibrils	106
Figure 9. Histogram of the ON-OFF times in Tg-WT and D166V muscle.....	107
Figure 10. Relationship between molecular events, correlation function and observed signal calculated from the autocorrelation function	108
Figure 9. Best fit of the experimental autocorrelation function to the ideal saw tooth function.....	109

Chapter VI

Figure 1. Concept behind confocal SPCE microscope	122
Figure 2. SPCE signal from skeletal myofibrils as a function of the illumination angle.....	123
Figure 3. SPCE image of myofibril in rigor	124
Figure 4. Electric field of the evanescent wave at the surface.....	125
Figure 5. Calculated power flow to the objective in SPCE	126
Figure 6. Comparison of the dependence of the transition moment angle for TIRF and SPCE.....	127
Figure 7. Fluorescent image of the overlap zone	128

Figure 8. Confocal SPCE signal from rigor myofibril	129
Figure 9. Enhancement of fluorescence by SIF	138
Figure 10. Confocal image of myofibrils contributing to fluorescence.....	139
Figure 11. Enhancement of fluorescence by SIF using TIR fluorescence	140
Figure 12. Comparison of lifetime signals from myofibrils on glass and SIF	141
Figure 13. Comparison of the rate of photobleaching of myofibrillar overlap zone on glass and glass coated with SIF.....	142
Figure 14. Comparison of the rate of photobleaching of myofibrillar overlap zone on sapphire and sapphire coated with SIF	143
Figure 15. Comparison of the rate of photobleaching of myofibrillar overlap zone on Olympus coverslip with and without SIF	144
Figure 16. SEM Images of NML.....	155
Figure 17. AFM images of the NML surface	156
Figure 18. Representative images of myofibrils on glass	157
Figure 19. Demonstration that the quality of images is not degraded by the presence of colloid.....	158
Figure 20. Image of myofibrils on NML	159
Figure 21. Enhancement of fluorescence by colloid monolayers	160
Figure 22. Decrease of fluorescence lifetime by mixed-size NML	161
Figure 23. Decrease of fluorescence lifetime by small and large NML	162
Figure 24. Photobleaching of myofibrils in the bulk solution	163
Figure 25. Comparison of the rates of photobleaching of the myofibrillar overlap zone on small NML	164

Figure 26. Schematic diagram of a myofibril on a glass coverslip with NML-coated surface...165

Figure 27. Intensity enhancement of silver spheroid particles in water.....166

Figure 28. Calculations to mimic the experimental setup167

Figure 29. Calculation of fluorescence (left) and bleaching (right) lifetimes.....168

LIST OF TABLES

Chapter I

Table 1. Disease causing genes in hypertrophic cardiomyopathy.....	3
--	---

Chapter IV

Table 1. Polarizations of samples	49
---	----

Chapter V

Table 1. Rate of duty cycle in transgenic WT and D166V muscle fibers.....	95
---	----

Table 2. Ton and Toff times of transgenic WT and D166V muscle fibers.....	97
---	----

Chapter VI

Table 1. Comparison of TIRF and SPCE images of muscle.....	117
--	-----

Table 2. Effect of NML on enhancement of fluorescence	149
---	-----

Table 3. Effect of NML on lifetime	151
--	-----

Table 4. Effect of NML on half-times of bleaching	153
---	-----

LIST OF ABBREVIATIONS

ADP	Adenosine diphosphate
DTT	Dithiothreitol
EDC	1-ethyl-3-(3'-dimethylaminopropyl) carbodiimide
EDTA	Ethylene-diamine-tetra-acetic acid
EGTA	Ethylene glycol-bis(β -aminoethyl) ether
ELC	Essential light chain
FHC	Familial hypertrophic cardiomyopathy
MHC	Myosin heavy chain
MLC	Myosin light chain
MyHC	Myosin heavy chain
NML	Metal nanoparticles
PMSF	Phenylmethylsulfonyl Fluoride
RLC	Regulatory light chain
RP	Rhodamine phalloidin
SIF	Silver island films
SPCE	Surface plasmon coupled emission
TIRFM	Total internal reflection fluorescence microscope
UP	Unlabeled phalloidin

CHAPTER 1

INTRODUCTION TO THE STUDY

Cardiovascular diseases are the leading cause of mortality worldwide; with heart failure being highly prevalent in most affluent parts of the world. In this proposal we study one such disease, familial hypertrophic cardiomyopathy (FHC). Despite significant clinical advances in the treatment of various cardiovascular diseases, mortality rates remain high. No therapy currently exists to treat or delay progression from hypertrophy to heart failure. We examine the kinetics (rate of contraction and ATPase activity) in cardiac muscle with the hope that this study may establish certain links to solve the reason the heart muscle goes into hypertrophy and ultimately heart failure

Familial Hypertrophic cardiomyopathy:

FHC is one of the hypertrophic cardiomyopathies, a group of cardiac diseases which also includes hereditary ventricular hypertrophy, asymmetrical septal hypertrophy, and hypertrophic sub aortic stenosis. It is a genetic disorder of the heart characterized by increased growth or hypertrophy in the thickness of the wall of the left ventricle, the largest of the four chambers of the heart (53). Although FHC has been largely regarded as a relatively uncommon cardiac genetic disease, the prevalence of echocardiographically defined hypertrophic cardiomyopathy in a large cohort of apparently healthy young adults selected from a community based general population was reported 3 years ago to be as high as 1 in 500 (64). It is currently the leading cause of sudden death in apparently healthy people under the age of 35. Clinical symptoms

include left and/or right ventricular hypertrophy, myocyte disarray, fibrosis, and cardiac arrhythmias that may ultimately lead to premature sudden death (52).

The importance of recognizing this disorder in patients as early as possible is highlighted by the high rate of sudden cardiac death in young people. Premature death can occur even in completely asymptomatic patients, as the first manifestation of the disease. Myocardial hypertrophy generally develops during adolescence; however in severe cases it can occur in infants or during fetal life. Simultaneously with hypertrophy, some patients become symptomatic, while others exhibit no symptoms over long periods. Clinical heterogeneity of the disease makes it difficult to predict the outcome of the disease and to diagnose subjects who are at high risk of premature death.

Genetic basis of the disease:

As a heterogeneous disease, it is inherited as an autosomal dominant trait. The first large pedigree of FHC was reported in 1960 (49). Molecular genetic studies have defined this disease as a disease of the sarcomere, the contractile unit within the cardiac myocyte that is comprised of thick and thin filaments. Mutations in genes encoding the sarcomeric proteins can impair normal protein function, which could ultimately lead to the morphological and physiological manifestations observed in FHC.

However, the exact mechanisms by which these sarcomeric genetic mutations lead to FHC are not completely understood. Recent studies have revealed functional defects of the sarcomere such as mutation dependent decreases or increases in force generation, disturbances in Ca^{2+} cycling and abnormal ATP use (5). In both animal models of FHC and humans affected with the disease, it is seen that the diastolic dysfunction precedes the development of

hypertrophy (1). Diastolic dysfunction is characterized by elevated diastolic pressure in the left ventricle despite normal or sub-normal diastolic volume which maybe the reason for the thickening of the left ventricle, which is a characteristic of this disease.

The first gene mutation to be identified for this disease was a missense mutation in the β -myosin heavy chain gene, which cosegregated with the disease in a large French Canadian family. Since then, over 450 mutations in 20 sarcomere related and myofilament related genes have been identified (Table 1) (40).

Table 1: Hypertrophic cardiomyopathy: Disease causing genes:

Gene	Protein	Frequency
<i>MYH7</i>	β -Myosin heavy chain	25-30%
<i>MYBPC3</i>	Myosin-binding protein C (cardiac type)	20-30%
<i>TNNT2</i>	Troponin T (cardiac muscle)	3–5%
<i>TNNI3</i>	Troponin I (cardiac muscle)	<5%
<i>TPM1</i>	Tropomyosin 1 α	<5%
<i>MYL2</i>	Regulatory myosin light chain 2 (ventricular/cardiac-muscle isoform)	<5%
<i>MYL3</i>	Essential myosin light chain 3	Rare
<i>ACTC</i>	α -Cardiac actin 1	Rare
<i>TTN</i>	Titin	Rare
<i>TNNC1</i>	Troponin C	Rare
<i>MYH6</i>	α -Myosin heavy chain	Rare
<i>CSRP3</i>	Muscle LIM protein	Rare
<i>MYLK2</i>	Myosin light chain kinase 2	Rare
<i>LDB3</i>	LIM binding domain 3	Rare
<i>TCAP</i>	Telethonin	Rare
<i>VCLV</i>	includin/metavinculin	Rare
<i>ACTN2</i>	α -actinin 2	Rare
<i>PLN</i>	Phospholamban	Rare
<i>MYOZ2</i>	Myozenin 2	Rare
<i>JPH2</i>	Junctophilin 2	Rare

Severe phenotypes have been reported in families with mutations in FHC-causing genes other than *MYH7*, *MYBPC3*, *TNNT2* and *TNNI3*. It has been seen that patients harboring mutations in *ACTC* (α -cardiac actin 1), and in *MYL2* and *MYL3* (regulatory and essential myosin light chains 2 and 3) have unusual patterns of hypertrophy (2). The cardiac phenotype that was observed in most of the cases was massive hypertrophy of the ventricular muscle and adjacent papillary muscle, causing a mild cavity obstruction. In this work we deal with the *MYL2* mutation. Shown below is the schematic organization of sarcomeric proteins associated with FHC (Fig 1).

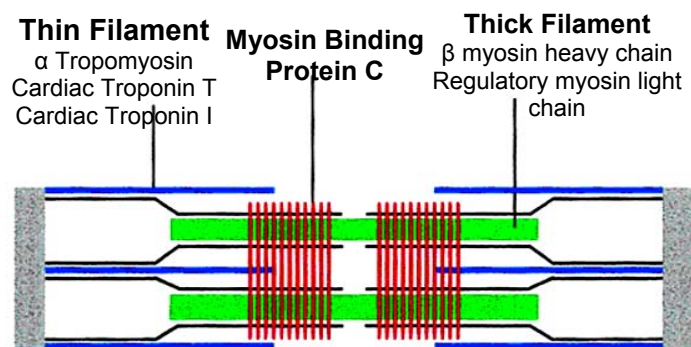


Fig. 1: The disease genes encode contractile proteins of the thick filament (in green), associated proteins of the thin filament (in blue), and a myosin binding protein (in red). The Z lines and the titin filament are indicated in gray and black, respectively.

These genes certainly do not represent the whole spectrum of FHC disease genes, and one might reasonably hypothesize that disease genes yet to be identified include additional components of the sarcomere. One of the major challenges is to decipher the mechanisms

through which the disease results from sarcomeric gene defects. The recent developments of animal models and in vitro analyses have allowed a better understanding of the pathophysiological mechanisms associated with FHC. Based on recent studies, one can tentatively draw the following cascade of events: The mutation leads to a poison polypeptide that would be incorporated into the sarcomere. The mutation may cause an interference with a crucial protein: protein interaction could make the mutated myosin a true poison polypeptide. This would alter the sarcomeric function that would result (1) in an altered cardiac function and thus (2) in the alteration of the sarcomeric and myocyte structure. The poison polypeptide hypothesis is also supported by a variety of results obtained in vitro and by findings in nematodes in which missense mutations produce stable polypeptides that are incorporated into myofibrils and disrupt the sarcomere assembly (2, 10, 11).

Genetic testing in familial hypertrophic cardiomyopathy:

It is possible to perform mutation analysis for genetic testing, but this is not feasible due to the high cost. Some research centers in national healthcare systems (UK, Netherlands) offer testing on a selected basis, and it is commercially available via several private companies. Recent studies show a correlation between the morphological shape of the cardiac septum and the presence of sarcomeric gene mutations. In particular, Binder et al. reported that septal morphological subtype can predict the presence or absence of such mutations (13). This technique has not yet, however, been applied to patient screening.

The most accurate method for the diagnosis of FHC is currently DNA analysis. Recently, Priori and Napolitano presented a novel scoring system to compare the value of genetic analysis in terms of cost: benefit ratio in different cardiomyopathies and ion channel diseases. Their system is based on a number of technical and clinical criteria, such as size of genes to be

screened, success rate of genotyping, and the clinical benefits patients and their relatives derive from the identification of a mutation. According to this system, genetic testing is indicated in diseases achieving a score of at least 3, whilst a score of 1 or less indicates that genotyping should be performed for research purposes only, as identification of the underlying mutation has limited clinical application. FHC falls into the high-score category, which highlights the suitability of genetic analysis for diagnosis of this disorder. The clinical diagnosis of familial hypertrophic cardiomyopathy is usually made on the basis of a physical examination, electrocardiogram, and echocardiogram. It is generally considered that echocardiography is a more accurate technique than ECG for diagnosis in adults. Analysis of a large genotyped population recently showed that, in fact, ECG and echocardiography have similar diagnostic values for FHC in adults, with an excellent specificity and a lower sensitivity (31). As for penetrance, it is a much-debated issue. Before molecular genetic analyses, several studies have indicated either a full penetrance or an incomplete one. The penetrance of FHC in a large genotyped population was recently reassessed and was found that it is incomplete, age-related, and greater in males than in females (31). These latter data have very important implications for genetic counseling, especially for women under the age of 50.

Unraveling the rationale behind the reason a mutation affects the working of the heart and lead to a malignant disorder, could open doors towards novel therapeutic approaches to treat this disorder in the future. With this motive, in this project we look at a particularly malignant mutation in myosin regulatory light chain (MYL2).

Mutation in the regulatory light chain in FHC:

Several mutations in the myosin regulatory light chain (RLC) have been implicated in FHC. The RLC wraps around the alpha helical neck of the myosin head by binding to a 35 amino acid IQ motif, a structural domain that mediates interactions with calmodulin, on the myosin heavy chain. The neck region of the myosin heavy chain has been proposed to act as a lever arm, amplifying small conformational changes that originate at the catalytic site in the myosin head into large movements, allowing myosin to generate motion and force (39). Furthermore, this neck region has been proposed to serve as the compliant element in the myosin cross bridge with the RLC playing a structural role, modulating the stiffness of the lever arm (89). The RLC also contains a highly conserved phosphorylatable serine that plays an important role in the activation and modulation of myosin. In addition to a phosphorylation site, the RLC also contains an N-terminal divalent cation binding site. The absence of bound cation in the RLC binding site has been shown to alter the structural properties of the RLC and consequently, the contractile properties of the cation-free myosin. Furthermore, binding of nucleotides to the myosin head has been shown to alter the conformation of the RLC. Given the important role of RLC in muscle contraction, one can hypothesize that FHC mutations in the RLC could affect myosin mechanics or kinetics. In this project, we look at the mutation D166V or Asp166Val in the myosin RLC. We study the transgenic (Tg) animal model for this malignant FHC mutation using freshly skinned and intact muscle fibers from mouse hearts expressing ~95% D166V transgene (Tg-D166V). The results will be compared with those for fibers from hearts of transgenic wild-type (Tg-WT) mice expressing ~100% of normal the human ventricular RLC (91). Generation and characterization of transgenic mice has been illustrated in the materials and methods section.

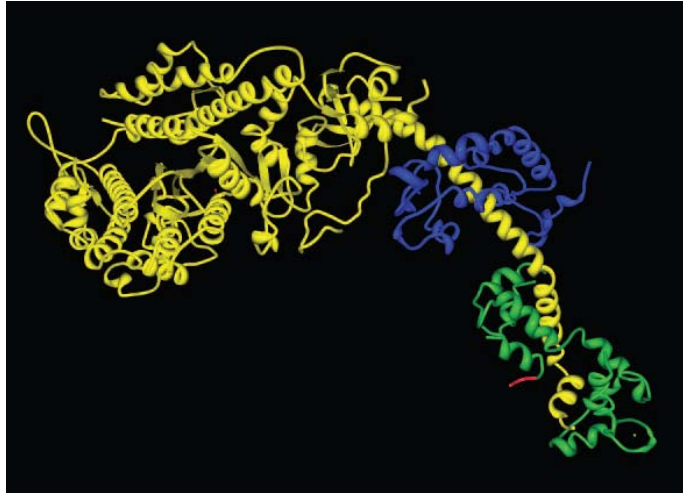


Fig 2: Schematic representation of the D166V mutation (labeled in red) in the myosin RLC. The heavy chain of myosin is labeled in yellow, the ELC in dark blue, and the RLC in green.

Although genetic studies have yielded compelling evidence that myosin mutations are responsible for FHC, not much is known about this disease at the molecular level. We explore this unknown facet of FHC by studying the kinetics of the disease. We speculate that a change in the kinetics of cross bridge interaction would alter the kinetics of a cross bridge motion, thereby affecting the efficiency of utilization of ATP during contraction, ultimately leading to FHC. This hypothesis has been specifically addressed in Chapter 5.

However, to grasp the working kinetics of muscle better, it is necessary to first understand the physiology of muscle.

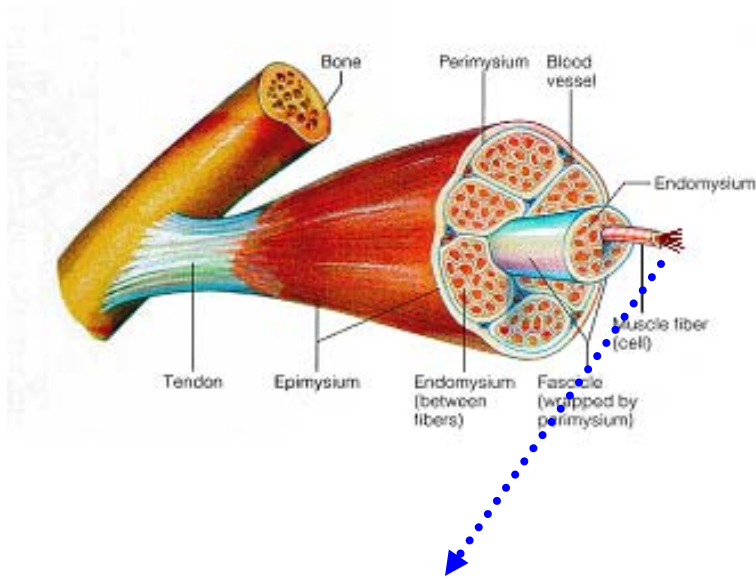
Structure and function of skeletal muscle:

Skeletal muscle is simpler and much more organized than cardiac muscle. Cardiac muscle resembles skeletal in that it is striated and each cell contains sarcomeres with sliding filaments of actin and myosin. The major differences between the two are that the myofibrils of each cell in cardiac muscle are branched in contrast to skeletal muscle where the myofibrils are

organized. The branches interlock with those of adjacent fibers by adherens junctions to enable the heart to contract forcefully without ripping the fibers apart. Due to its organized nature, we chose skeletal muscle as the working model of choice to study the basic kinetics of muscle. It will be used in the first specific aim to study the working in a healthy muscle. Because it is organized in nature, we believed it would be easier to detect a single cross bridge. The methods established in skeletal muscle will be applied to achieve aim 2 using cardiac muscle. The rationale behind studying a single cross bridge has been explained towards the end of this chapter.

a) Structure: Muscle is composed of cells or fibers embedded in a matrix of collagen. At either end of the muscle belly, this matrix becomes the tendon that connects the muscle to the bone (Fig 3a). An individual skeletal muscle may be made up of hundreds, or even thousands, of muscle fibers bundled together and wrapped in a connective tissue covering, called the epimysium. Portions of the epimysium project inward to divide the muscle into compartments. Each compartment contains a bundle of muscle fiber. Muscle fibers are in turn grouped into bundles (of up to 150 fibers) called fascicles. Each individual fiber consists of a membrane (sarcolemma) and can be further broken down into thousands of myofibrils. Myofibrils are surrounded by sarcoplasm and together they make up the contractile components of a muscle. Each myofibril in turn is composed of repeating sarcomere units separated by Z disks. It consists of both thick and thin filaments. The thick filaments are composed of several myosin molecules assembled together. Myosin has tiny globular heads protruding from it at regular intervals. These are called cross bridges and play a pivotal role in muscle action. The thin filaments are composed of actin, troponin and tropomyosin.

a)



b)

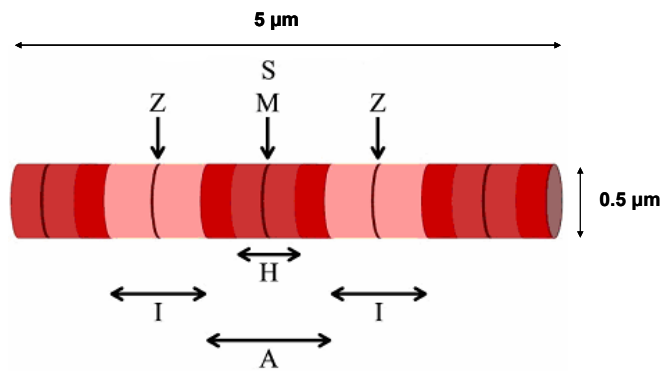


Fig. 3: Skeletal muscle at increasing magnification. a) Muscle; b) Single myofibril

In fig 3.b, the sarcomere has been divided into different zones to show how it behaves during muscle action. S denotes a single sarcomere which is bound on both sides by the Z line. The Z-line separates each sarcomere. The two proteins, actin and myosin overlap at the A band, while I band contains only the actin protein. Myosin filaments extend throughout the A-band. During muscle contraction, the H-zone and I-band both decrease as the Z-lines are pulled towards each other.

b) Myosin (Structure and chemistry): Despite the common belief that myosin is only present in muscle cells, different isoforms of myosin are also present in the cytoplasm. Myosin I plays an important role in cytoskeletal reorganization and organelle translocation. Various isoforms have been identified in the cytoplasm, plasma membranes, lamellipodia, brush border of the microvillus, mitochondria of photoreceptor cells and membranes of neuronal cell bodies and dendrites (90). Myosin V is associated with transport of cargo along with actin filaments and is classified as a processive motor. For each encounter with actin, myosin V goes through multiple ATPase cycles, travels long distances, and carries cargo without dissociating from actin. While myosin V transports cargo toward the barbed end, myosin VI, another class of myosin, transports cargo toward the pointed end of actin. Myosin VI serves as an intermediary motor, transferring clathrin coated pits onto cytosolic actin filaments during endocytosis. Myosin VIIb is normally expressed in the receptor cells of the inner ear and the pigment epithelium of the retina.

However, the most common type or conventional myosin is myosin II. This class of myosins is present in the smooth, cardiac and skeletal muscle, the latter two being the focus of this thesis. They are used to contract muscle tissue, thereby giving organism mobility (Fig 4).

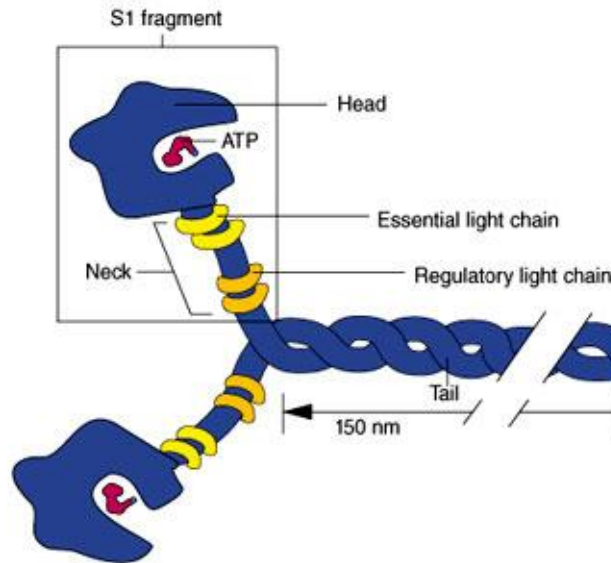


Fig. 4: Myosin structure: There are three major and functionally different domains in the myosin molecule: a motor domain, a lever arm domain - both located in the myosin head (S1), and a tail region.

Myosin molecule contains two heavy chains. Each heavy chain continues into a tail domain in which repeat sequences promote dimerization by interacting to form a rod-like α -helical coiled coil. It is a hexamer with a total molecular weight of 520 KD and is composed of two heavy chains and four light chains. The two heavy chains each weigh 220 KD and begin with a globular head at the N-terminal and end with an alpha-helix at the C-terminal. The tail (C-terminal) region is periodically interspersed with hydrophobic residues to give a “coiled coil” type rod. The tails are connected to the heads at the neck, which is the location of the hinge area. The myosin motor domain contains a catalytic site, also called an ATP binding site, and an actin binding region. The four light chains are about 20 KD each and are paired into two regulatory light chains (RLC) and two essential light chains (ELC). The RLC is wrapped around the heavy chain and stabilized by a group of hydrophobic residues, including methionines, tryptophans, and

phenylalanines. It is also the site of phosphorylation by myosin light chain kinase. The light chains bind the heavy chain at an IQ motif consisting of Ile-Gln-x-x-x-Arg-Gly-x-x-x-Arg.

RLC is 171 amino acids long and is non covalently bound to the heavy chain at the lever arm or hinge region of the myosin head. ELC exists in two isoforms which are alternatively spliced from one gene, ELC-1 and ELC-2. Both ELC and RLC belong to a family of EF hand calcium binding proteins and display the characteristic folding of other EF hand proteins, like calmodulin, troponin C and parvalbumin.

ATP binds to the myosin head adjacent to a 7- β stranded β -sheet. Loops extending from β -strands interact with the adenine nucleotide. The nucleotide-binding pocket of myosin is opposite a deep cleft that bisects the actin-binding domain. Opening and closing of the cleft is proposed to cause the head to pivot about the neck region, as occupancy of the nucleotide-binding site changes and as myosin interacts with and dissociates from actin.

c) Actin myosin cross bridge cycle: In the 52 years since A. F. Huxley (1957) first proposed a quantitative model of how the myosin cross-bridges in muscle act to produce shortening, it has proved difficult to determine precise values for the amount of filament movement generated by one cross-bridge during an interaction with actin filament (i.e. the cross-bridge working stroke) and the load dependence of the working stroke (54). These are important parameters because they characterize the basic process underlying muscle contraction. Explained below is the historical overview of the cross bridge cycle.

There are three main events that occur in skeletal muscle contraction; electrical excitation of a muscle fiber, excitation contraction coupling, and muscle fiber contraction due to the sliding filament mechanism.

Electrical excitation of a muscle fiber: Skeletal muscle fibers can be stimulated by a motor neuron in the body. This results in depolarization of the sarcolemma. If this depolarization reaches the threshold, an action potential (electrical signal) is initiated.

Excitation-contraction coupling: The action potential is transmitted along the sarcolemma and down the T-tubules. This action causes calcium ions to be released from the terminal cisternae of the sarcoplasmic reticulum. Calcium ions couple electrical excitation to muscle fiber contraction by binding to troponin, which is attached to the actin filament and tropomyosin. Troponin changes shape and pulls tropomyosin away from the myosin-binding sites on the actin filament.

Muscle fiber contraction: When the myosin binding site on the actin filament is exposed, a contraction cycle consisting of 4 steps begins (Fig 5). A muscle fiber contracts due to thin filaments (actin) sliding past the thick filaments (myosin). The four steps of the contraction cycle are; i) ATP hydrolysis - Myosin heads contain an ATP binding pocket. When ATP binds to the ATP-binding pocket, the ATPase hydrolyzes ATP forming ADP and inorganic phosphate. Hydrolysis of ATP energizes the myosin head. ii) Next is the attachment of myosin to actin to form cross bridges. Energized myosin heads bind to the unblocked myosin-binding site on actin and the inorganic phosphate is released from the myosin head. iii) Power stroke - The release of the inorganic phosphate starts the power stroke, which is the rotation of the myosin head that pulls the thin filament toward the center of the sarcomere. During the power stroke, ADP is released from the myosin head, but the myosin head remains attached. iv) Detachment of myosin from actin – Another ATP molecule binds to the myosin ATP-binding pocket, releasing the myosin head from actin, and the contraction cycle begins again.

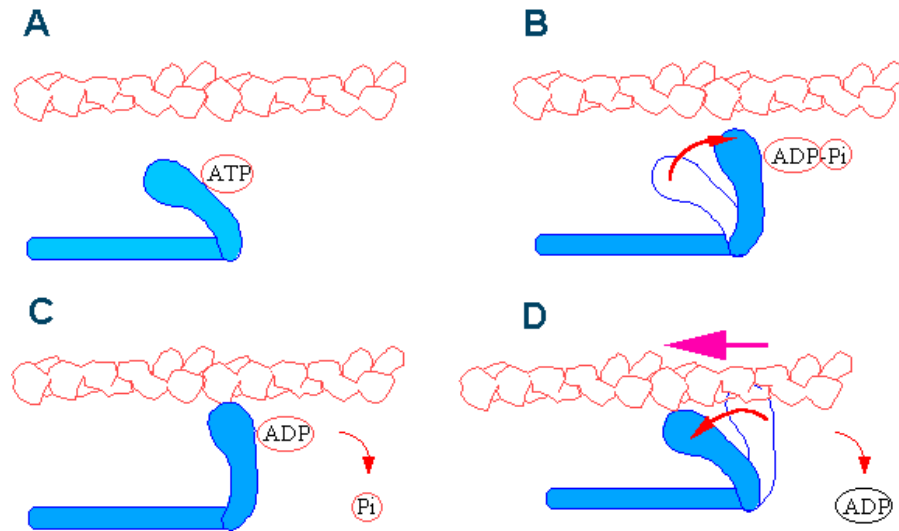


Fig. 5: Cross bridge cycle: The essential mechanochemical steps are shown lettered a to d. a) ATP binding to a cleft at the “back” of the head causes a conformation which cannot bind actin. b) As the ATP is hydrolyzed, the head swings back about 5nm to the “cocked” position the ADP and Pi remain bound. c and d) The force generating stages. When the Pi leaves the myosin, the head binds the actin and the “power stroke” is released as the head bind actin. ADP is released to continue the cycle. At this stage the head in bound to actin in the “rigor” or tightly bound state.

The contraction cycle continues as long as the intracellular calcium levels remain high. As the intracellular calcium levels drop, tropomyosin blocking of the myosin-binding sites on actin return, energized myosin is prevented from binding, and the muscle fiber relaxes.

To study the cross bridge kinetics, the anisotropy of a fluorescent molecule attached to actin will be followed through the cross bridge cycle. Anisotropy is a popularly used technique in biophysics which allows the observation of the orientation of a fluorescently labeled molecule over time, e.g., during one cross bridge cycle. A fluorescent dye is attached to a specific molecule such as actin, and anisotropy follows, by virtue of the dye, the movement of actin. By

nature, fluorescent dyes exhibit a dipole moment. Dipole moment measures the polarity of a polar covalent bond and is the direction of the dipole that is measured. This would reveal information regarding rotation during muscle contraction from a small number of molecules.

d. Method of measuring kinetics:

Fig 6 shows the signal that is expected from a single fluorophore attached to actin. The signal is shown in red in the bottom panel and is the anisotropy of fluorescence of a dye attached to actin. Starting at the left, the cross bridge is unbound and an anisotropy of 0 is seen. When it strongly attaches to actin, force is produced and the anisotropy is increased because the cross-bridge is now immobilized. Phosphate release is followed by the dissociation of ADP and the onset of rigor. Its end is marked by the binding of a fresh molecule of ATP, detachment of myosin from actin and the associated decline of the anisotropy signal. Finally, ATP is hydrolyzed to ADP and phosphate, and the cycle repeats.

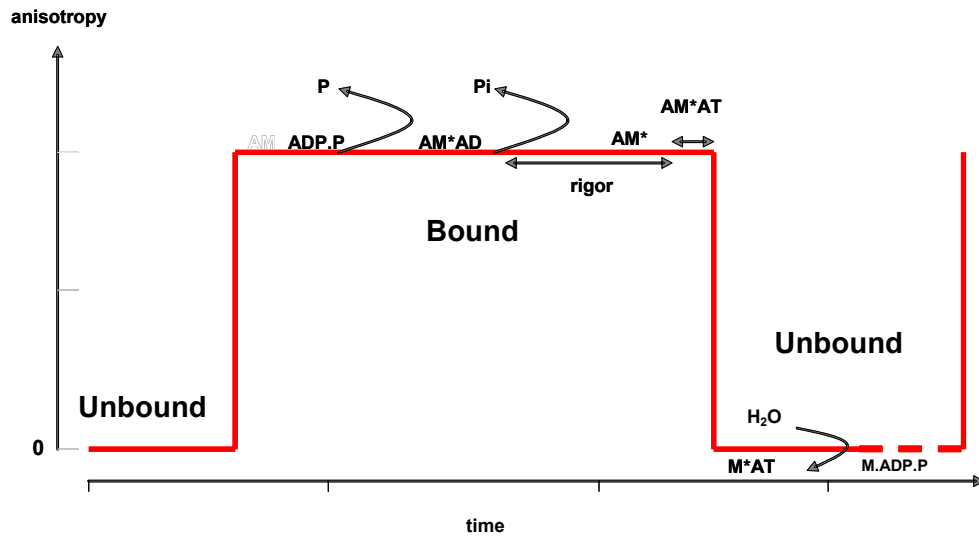


Fig. 6: The scheme illustrates how the orientation signal from a single cross-bridge of contracting muscle is expected to look. The anisotropy of fluorescence of a probe attached to the lever arm of myosin acts as an indicator of cross-bridge orientation (red).

Structure and function of cardiac muscle:

Cardiac muscle is found only in the heart, where it forms a muscular bag, the myocardium in the atria and in the ventricle. The cells are uninucleate cylinders with a diameter of 10-20 μm . They are short (50 -100 μm) but are often branched, and joined to each other end-to-end to form an interlacing meshwork. The junctions between cells are partly tight junctions for strong adherence, and partly low resistance gap junctions. The gap junctions allow free spread of small molecules and electrical currents between the fibers. These fibers are cross-striated like skeletal muscle fibers. This muscle gives spontaneous, forcible contractions, repetitively throughout life.

Cardiac myosin is a conventional class II myosin that consists of 2 heavy chains (MyHCs) and 2 pairs of light chains (MLCs). The multigene families of heavy chains (HC) and

light chains (LC) generate different isoforms that occur at various stages of heart development. The two HC isoforms are known as α - and β -isoforms. First it was thought that the functional properties of heart muscle are determined by their LC composition, but recent studies show that the heavy chains determine the myosin ATPase activity *in vitro* and the shortening velocity in the intact heart (59).

Cardiac muscle contraction:

Cardiac muscle is rich in mitochondria and myoglobin and is highly dependent on a good oxygen supply. In cardiac muscle, the mechanism of contraction is essentially the same as in skeletal, but the excitation-contraction coupling mechanism differs slightly. T-tubules invaginate at the level of the Z-lines. The sarcoplasmic reticulum is relatively poorly developed (cisternae are small or absent) and provides insufficient Ca^{2+} to fully activate the contractile apparatus. Unlike those in skeletal muscle, the channels in cardiac muscle are activated by Ca^{2+} in the cytosol (calcium activated calcium release) and Ca^{2+} entry through dihydropyridine channels is an important trigger of Ca^{2+} release.

Cardiac contraction occurs when calcium binds the troponin complex and tropomyosin, making possible the myosin-actin interaction. Actin stimulates ATPase activity in the globular myosin head and results in the production of force along actin filaments. Cardiac myosin-binding protein C, arrayed transversely along the sarcomere, binds myosin and, when phosphorylated, modulates contraction. In hypertrophic cardiomyopathy, mutations may impair these and other protein interactions, result in ineffectual contraction of the sarcomere, and produce hypertrophy and disarray of myocytes. After contraction, Ca^{2+} is pumped back into the SR by a Ca^{2+} - Mg^{2+} -

ATPase pump, and back to the extra-cellular fluid by a Na^+ -dependent Ca^{2+} pump in the sarcolemma (these two pumps compete with each other).

To understand the complexities of contraction, it is important to investigate as few molecules as possible as each molecule behaves differently and a large population would only provide gross information about a whole muscle and not individual molecules. Fig 7 explains this concept in detail.

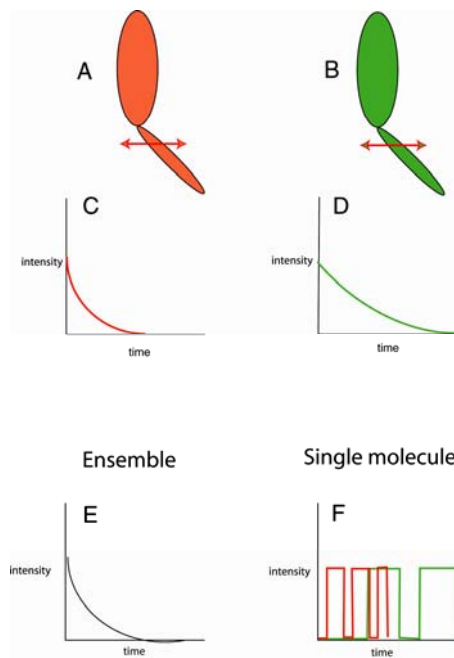


Fig. 7. Schematic showing why it is crucial to measure kinetics of single heads. Suppose wild type (WT) heads are fast (A, red) and mutated heads are slow (B, green). The relaxation of fast heads, as measured by the orientation of the transition dipole of the dye attached to the light chain (arrow) is fast (C), and the relaxation of slow heads is slow (D). The rate of relaxation of a large ensemble of heads will be a weighted average of slow (E) and fast relaxations (F).

It is impossible to tell from such a curve whether relaxation of mutated and non-mutated heads is different.

Most of the experiments in specific aim 1 and 2 have been performed using total internal reflection fluorescence microscopy and this has been mentioned as and when used.

Total internal reflection fluorescence (TIRF):

Total internal reflection fluorescence microscopy (TIRFM) is a powerful technique for studying events that occur near a cell surface. The technique allows selective imaging of fluorescent molecules that are closest to a high refractive index substance such as glass.

Principle: Light directed from a material of high refractive index (n_1) to one of lower refractive index (n_2) is totally reflected at angles equal to or greater than the critical angle, α_c . At these angles an electromagnetic "evanescent field" is formed in the lower refractive index medium (Fig. 8). This wave decays exponentially with distance from the interface with length constants that can be much shorter than the wavelength of illumination light. TIRFM (also known as evanescent field fluorescence microscopy) uses the thin evanescent wave to selectively excite fluorescent molecules in the portion of the lower refractive index medium nearest the interface of the two media. In cell biological or neurobiological studies, the low refractive index medium is usually the cytoplasm of a cell adherent to a higher refractive index coverslip.

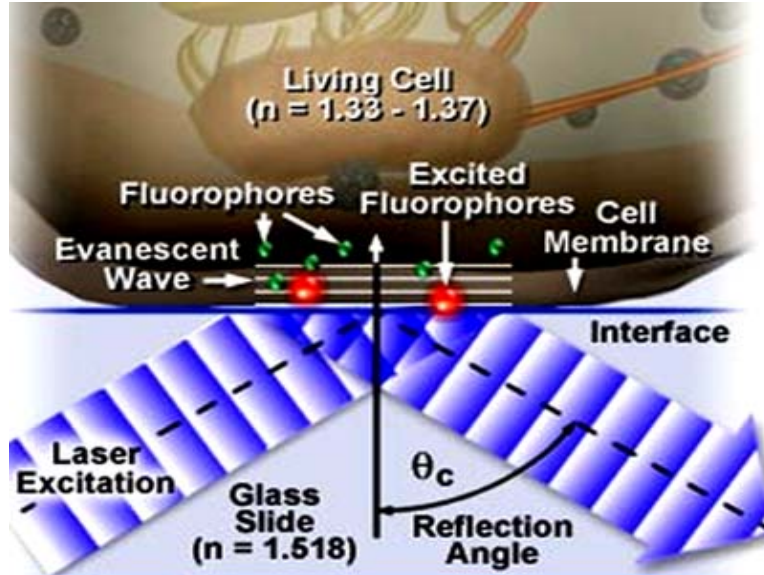


Fig. 8: Schematic of the principle of total internal fluorescence reflection. Total internal reflection fluorescence microscopy (TIRFM) employs the unique properties of an induced evanescent wave to selectively illuminate and excite fluorophores in a restricted specimen region immediately adjacent to a glass-water (or glass-buffer) interface. The excited fluorophores are shown in red.

For example, when a cell with fluorescently labeled secretory vesicles is firmly attached to a coverslip, the dye molecules will be excited only in those vesicles that lie within the thin evanescent field, thereby providing a high signal-to-noise ratio for vesicles within this region. In addition, the exponential drop in light intensity with distance allows small movements relative to the coverslip to be monitored by tracking object fluorescence. Using this method, single vesicles near (less than ~ 100 nm) the plasma membrane can be monitored as they travel to the membrane and undergo exocytosis.

In our third specific aim, we apply our work in previous two specific aims to human patients. Human patients are normally heterozygous for FHC mutations, so their myosin containing thick filaments are composed of wild type myosin heads interspersed with FHC mutant heads. Any large observational volume thus contains a mixture of WT and FHC molecules, making the comparison between kinetics of healthy and diseased muscle impossible. Therefore, the unambiguous determination of myosin cross-bridge kinetics requires that the experiments are carried out at the level of a single molecule to avoid averaging over ensembles of molecules with different kinetics. However, single molecule detection requires that the muscle be illuminated with intense laser light. This causes bleaching and muscle photodamage. Surface plasmon coupled emission (SPCE) has been used in Chapter 3 to aid achieving decrease of photobleaching; the principle of which has been illustrated below.

Surface plasmon coupled emission (SPCE):

The coverslip on which the sample is imaged is covered with metal. At the SPCE angle (close to the surface plasmon resonance or SPR angle), the incident light penetrates the metal and induces surface plasmons to propagate along the coverslips. Surface plasmons create an evanescent wave which excites the fluorophores in the sample. The fluorescent light couples with the traveling plasmons with the result that fluorescent light is transmitted (down) on a surface of a cone (Fig. 9).

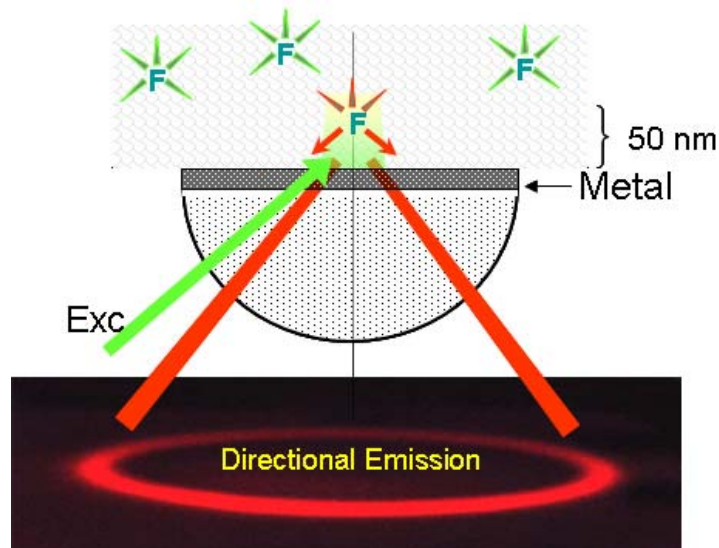


Fig. 9: Concept behind SPCE microscope.

The fluorescence is quenched at the metal interface (up to approximately 10 nm), which limits the thickness of the fluorescent volume to approximately 50 nm. The fluorescence is detected through a confocal aperture, which limits the lateral dimensions of the detection volume to approximately 200 nm. The resulting volume is approximately 2×10^{-18} liter. The method is particularly sensitive to rotational motions because of the strong dependence of the plasmon coupling on the orientation of excited transition dipole. We show that by using a high-numerical-aperture objective and high-refractive-index coverslips coated with gold, it is possible to follow rotational motion of 12 actin molecules in muscle with millisecond time resolution.

Using the above techniques, we propose to look at a single cross bridge kinetic in working muscle. Our hypothesis is that the FHC RLC mutation (D166V) (Fig 2) will affect the physiological properties of cardiac muscle. The results of this study could contribute to development of targeted cellular therapeutic approaches to limit FHC related cardiac dysfunction.

This proposal establishes certain links to solve the reason the heart muscle goes into hypertrophy and ultimately heart failure. In addition, development of methods to image a single fluorophore in tissue, which is addressed in the first specific aim, would have numerous implications in the biological field. Observing a single fluorophore would help monitor ligand-receptor interactions in live cells, involvement of protein molecules in internalization of bacteria by cells, conformational fluctuations of DNA, diagnosis of prion diseases and also in detection of viruses at an early phase of infection.

CHAPTER II

MATERIALS AND METHODS

Chemicals and solutions

Rhodamine-Phalloidin (RP) and 5'-iodoacetamido-tetramethyl-rhodamine (5'-IATR) were from Molecular Probes (Eugene, OR). Fluorescein phalloidin, unlabeled phalloidin, phosphocreatine, creatine kinase, glucose oxidase and catalase were from Sigma (St Louis, MI). All other chemicals including 1-ethyl-3-(3'-dimethylaminopropyl) carbodiimide (EDC), phosphocreatine, creatine kinase, glucose oxidase, catalase and ATP were from Sigma. EDTA-rigor solution contained 50 mM KCl, 2 mM EDTA, 1 mM DTT, 10 mM Tris-HCl buffer pH 7.5. Ca-rigor solution contained 50 mM KCl, 4 mM MgCl₂, 0.1 mM CaCl₂, 1 mM DTT, 10 mM Tris-HCl buffer pH 7.5. Mg-rigor solution contained 50 mM KCl, 4 mM MgCl₂, 1 mM DTT, 10 mM Tris-HCl buffer pH 7.5. Contracting solution was the same as Ca-rigor, except that it contained in addition 2 mM ATP.

Coverslips

Glass coverslips No.#1 were from Fisher. Sapphire coverslips were purchased from MPA Crystal Corp. (San Francisco, CA). Olympus coverslips, specially designed for TIRF experiments using NA = 1.65 objective, were made from high-refractive-index material. Olympus would not reveal its composition.

Preparation of coverslips for the Surface Plasmon coupled experiments

High refractive index cover glasses from Olympus, or quartz slides (spectrosil 1, Starna Cells, Inc.) were coated by vapor deposition by EMF Corp. (Ithaca, NY). A 52 nm thick layer of silver and 48 nm layer of gold was deposited on the coverslips. 2 nm chromium undercoat was used as an adhesive background.

Preparation of silver island films

Coverslips were incubated with poly-L-lysine solution (Sigma 0.1%) for 1 h and rinsed thoroughly with water. The 500 mg AgNO₃ (99% Aldrich) was dissolved in 60 mL water and 5% NaOH was added until brown precipitate formed. Next 30% NH₄OH was added to dissolve the precipitate and then the solution was cooled in ice for 3 min. 15 mL of glucose was added to this solution and the coverslips were inserted in it. The solution was then heated for 2 min followed by cooling at room temperature for 3 min. Coverslips were removed when the solution turned cloudy.

Preparation of nanoparticle monolayers

All necessary glassware were soaked in a base bath overnight and then washed with deionized water. A solution of 18 mg/mL silver nitrate (200 mL) was heated and stirred in a 250-mL Erlenmeyer flask at 95°C. A 0.5-mL aliquot of 34 mM trisodium citrate solution was added dropwise. The solution was stirred for 20 min and warmed to 96–98°C. Five aliquots (0.7 mL each) of 34 mM trisodium citrate were then added dropwise to the reaction mixture every 15–20 min. Stirring was continued for 25 min until the milky yellow color remained. Then, the mixture was cooled in an ice bath for 15 min. The colloids were separated by centrifugation at 3500 rpm

for 6 min. The residues were collected and dissolved in 1 mM trisodium citrate. The nanoparticles were then covalently attached to glass coverslips. The glass coverslips were washed with Alconox soap and rinsed with distilled water. They were then soaked for 2 h in 0.1 M NaOH to activate the surface, rinsed copiously with distilled water, and soaked overnight at 80–90°C in a solution of 5% (v/v) amino-propyl-triethoxy-silane buffered with 0.1 M acetic acid (pH 5.5). Next, the coverslips were rinsed with deionized water, air dried, and placed in a petri dish for drop-coating with the solutions of small or large silver colloids. About 300 mL of the colloidal silver sols were drop-coated on the desired area of the glass coverslip. After incubation for 2 h at room temperature, the excess of colloidal silver solution was rinsed with deionized water. The glass coverslips with attached silver nanoparticles were air-dried and stored in vials.

Generation and characterization of transgenic mice

The D166V-mutated human RLC cDNA was cloned into the *SalI* site of the plasmid, α -myosin heavy chain (α -MHC) clone 26 (provided by Dr. J. Robbins, Cincinnati Children's Hospital Medical Center, Cincinnati, OH, USA). The resulting construct contained ~5.5 kb of the mouse α -MHC promoter, including the first two exons and part of the third, followed by the D166V (498 bp) and a 630-bp 3' untranslated region from the human growth hormone transcript. The founder mice have been bred to NTg B6SJL mice.

Isolation of cardiac muscle

After euthanasia, the hearts from 6-month old Tg-D166V and Tg-WT mice were quickly removed and rinsed briefly (no more than 30 s) with ice-cold 0.9% NaCl. Muscle strips from left ventricles and papillary muscles were dissected at 4°C in a cold room in ice-cold pCa 8 solution (10^{-8} M $[Ca^{2+}]$, 1 mM $[Mg^{2+}]$, 7 mM EGTA, 2.5 mM $[MgATP^{2+}]$, 20 mM MOPS (pH 7.0), 20 mM creatine phosphate and 15 units/mL creatine phosphokinase, ionic strength) 150 mM adjusted with potassium propionate) containing 30 mM 2,3-butanedione monoxime (BDM) and 15% glycerol. After dissection, muscle strips were transferred to a calcium solution mixed with 50% glycerol and incubated for 1 h on ice. Then, the muscle strips were transferred to fresh pCa 8 solution mixed with 50% glycerol and containing 1% Triton X-100, for 24 h at 4°C. Muscle strips were finally transferred to a fresh batch of pCa 8 solution mixed 1:1 with glycerol and kept at -20°C until used for the preparation of myofibrils.

Preparation of skeletal myofibrils

Rabbit psoas muscle was first prewashed with cold EDTA-rigor solution (50 mM KCl, 2 mM EDTA, 10 mM DTT, 10 mM Tris-HCl, pH 7.6 for 0.5 h, followed by Ca-rigor solution. Myofibrils were then obtained from fibers by the following procedure: a 0.3 g strip of muscle fiber was transferred from the glycerinating solution to a solution containing 50mM KCL, 2 mM EDTA, 5 mM Na-P buffer (pH 7) for 0.5 h at 0°C. EDTA was used to inhibit the contraction when the MgATP in the relaxing solution is washed out. The muscle was then cut into small strips and homogenized in a Heidolph Silent Crusher S with 10 ml of solution containing 80mM KCL, 5 mM Na-P buffer (pH 7). Myofibrils were then centrifuged at 2000 revs/ min and gently resuspended in a solution containing 80 mM KCL, 5 mM Na-P buffer.

Preparation of Cardiac Myofibril

Myofibrils from Tg-WT and Tg-D166V mouse papillary muscles and left ventricles were prepared from glycerinated fiber bundles stored at -20°C in glycerinating solution. The muscle fibers were first incubated in EDTA-rigor solution until they turned white (~ 1 h). The fiber bundle was then homogenized using a Heidolph Silent Crusher S homogenizer for 20 s (with a break to cool after 10 s) in Mg^{2+} -rigor solution. It was important that the fibers were not homogenized in the EDTA rigor buffer to avoid foaming. All fluorescence lifetime experiments were performed on freshly prepared myofibrils. Labeled myofibrils (25 μL) were applied to a 20 mm diameter (19 mm \times 19 mm) glass bottom coverslip (Menzel-Glaser 20 \times 20 mm #1). The sample was then incubated on the coverslip for 3 min to allow the myofibrils to adhere to the glass. The bottom coverslip was covered with a small (5 mm in diameter) top glass coverslip, and the cover slips were separated from each other by Avery Hole Reinforcement Stickers. Labeled myofibrils were washed with at least five volumes of the Ca^{2+} -rigor solution by applying the solution to one end of the sandwich and absorbing the excess solution with #1 filter paper at the other end.

Cross-linking of myofibrils

In order to prevent shortening during contraction, as this would interfere with the collection of data, ctin myofibrils were lightly cross-linked with water-soluble cross-linker EDC. 1 mg/mL myofibrils were incubated with 2 mM EDC for 10 min at room temperature. The reaction was stopped by 20 mM DDT. The lack of shortening was checked in a phase microscope.

Labeling of myofibrils

1 mg/mL of myofibrils were labeled by 5' incubation with 0.1 μ M fluorescein- or rhodamine-phalloidin + 9.9 μ M unlabeled phalloidin. After labeling myofibrils were washed by centrifugation on a desktop centrifuge at 3000 rpm for 2 mins followed by resuspension in rigor solution. The 15 μ L of myofibrillar suspension was placed on uncoated or coated coverslips. A narrow channel was created by applying a thin layer of Vaseline along the edges of the coverslip. To align myofibrils as much as possible along the long axis of the coverslip, the sample was applied by streaking the pipette along the long axis. The sample was left on a coverslip for 3 min to allow myofibrils to adhere to the coverslip. The coverslip was covered with a small (5 mm diameter) glass coverslip and washed with at least 5 volumes of Ca-rigor solution (containing phosphocreatine, creatine kinase, glucose oxidase and catalase to remove oxygen and maintain, where needed, ATP concentration) by applying the solution to one end of the channel and absorbing with #1 filter paper at the other end.

Atomic force microscopy and scanning electron microscopy

Atomic force microscopic (AFM) imaging was performed on the AFM Explorer (ThermoMicroscopes/Veeco Instruments, New York) in contact scanning mode with a nonconductive silicon nitride probe (Veeco Instruments). Images were acquired at a rate of 2–5 mm/s with a resolution of 300 pixels/line. The images were processed with WSxM Ver 4.0 software for 3D analysis and with the Veeco SPMLab Ver 6.0.2 software for 2D analysis. Scanning electron microscope (SEM) images were recorded with JEOL JSM 648OLV microscope.

Bulk sample preparation

Rhodamine 6G (laser grade) was deposited on the surface by spin-coating at 3000 rpm a 0.5% solution of low-molecular weight PVA (poly-vinyl alcohol, molecular weight 13000-23000, Aldrich) in water. The PVA solution contained Rhodamine 6G (Rh6G). The thickness of the sample (Rh6Gdoped PVA layer) was estimated from the comparison of reflectance measured for a metalized quartz slide before and after the sample deposition. For silver coated substrates, a 532 nm, p-polarized laser beam shows SPR angles of 49 and 52 degrees for the slides without and with the sample. Such a change in the SPR angle corresponds to a ~20 nm thick layer of dielectric with refractive index $n = 1.5$. As a background fluorescence, ethanol solution of DCM (4-(dicyanomethylene)-2-methyl-6-(p-dimethylaminostyryl)4H-pyran, Kodak) which was attached to the slide with sample using a demountable cuvette (100 micron path way) was used. It was checked that ethanol does not dissolve PVA.

Bulk fluorescence measurements

The sample was positioned in the sample compartment of the Varian Eclipse Spectrofluorometer (Varian, Inc.) in the front-face configuration. The excitation was at 530 nm, and on the observation a 540 nm long wave pass filter was used. Under these conditions, there was no detectable signal from either a bare glass slide or a SIF reference slide. Fluorescence lifetimes were measured by a time-domain technique using the FluoTime 200 fluorometer (PicoQuant, Inc.). The sample was positioned in front-face configuration inside the fluorometer chamber. The excitation was by a 475-nm laser-pulsed diode, and the observation was through a monochromator at 575-nm with supporting 550 nm long wave pass filter. The intensity decays were analyzed in term of a multiexponential model using FluoFit software (PicoQuant, Inc.).

Microscopic measurements for SPCE experiments

The schematic of the microscope is shown in Fig. 1. Excitation light from an expanded Diode Pumped Solid State laser beam (Compass 215M, Coherent, Santa Clara, CA) enters the epi illumination port of the inverted microscope (Olympus IX51).

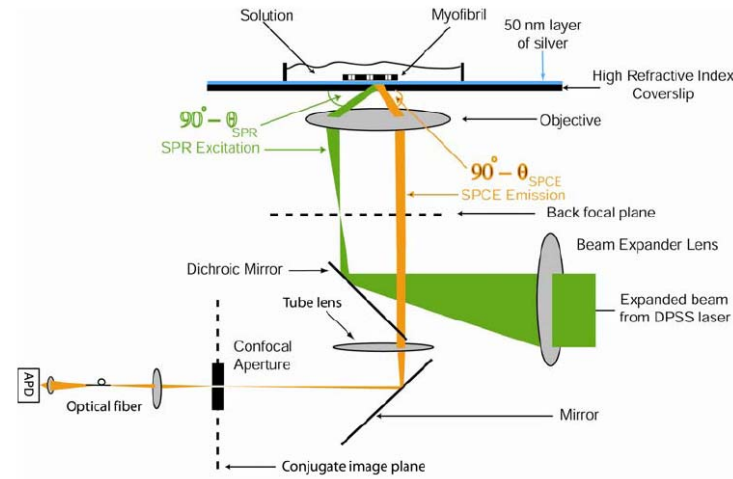


Fig. 1: Prismless confocal SPCE microscope. Not to scale.

The expanded laser beam, focused at the back focal plane of the objective, is directed by the movable optical fiber adapter to the periphery of the objective (Olympus Apo 100x, 1.65 NA), where it refracts and propagates towards the high-refractive-index glass metal/ buffer interface. When the incidence angle is equal to the SPR angle, the light is able to penetrate the metal and illuminate a cell. Excitation light produces an evanescent wave on the aqueous side of the interface at the surface of a sample. Normally, the evanescent field decays exponentially in the z-dimension with a penetration depth, $d = \lambda_0 / (4\pi(n_g^2 \sin^2 \theta - n_w^2)^{1/2})$, where λ_0 is the wavelength of the incident light, n_g is glass refractive index, and $n_w (=1.33)$ is the refractive index of water. In our case, however, the detection volume is a composition (product) of evanescent wave penetration depth and distance-dependent coupling with surface plasmons. In addition, the

detection volume is further reduced by a metal quenching of excited fluorophores at a close proximity (below 10 nm). We show below that the height of the detected volume is 40-70 nm, depending on the orientation of the excited dipoles. The fluorescent light, emitted at SPCE angle, is collected by the objective. The sample rests on a moveable piezo stage (Nano-H100, Mad City Labs, Madison, WI) controlled by a Nano-Drive. This provides sufficient resolution² to place the region of interest (ROI) in a position conjugate to the aperture. The fluorescent light is collected through the same objective and projected onto a tube lens, which focuses it at the conjugate image plane. A confocal aperture or an optical fiber (whose core acts as a confocal aperture) is inserted at this plane. An Avalanche Photodiode (APD, Perkin-Elmer SPCM-AQR-15-FC) collects light emerging from the aperture.

Microscopic measurements for TIRF experiments

The excitation light from an expanded DPSS laser beam (Compass 215 M, Coherent, Santa Clara, CA) enters the epi illumination port of the Olympus IX51 inverted microscope. TIRF illumination is provided by the commercial adapter (Olympus, Center Valley, PA). The expanded laser beam, focused at the back focal plane of the objective, is directed by the movable optical fiber adapter to the periphery of the objective where it refracts and propagates toward the interface at incidence angles greater than the critical angle. In the experiments using glass coverslips, the Olympus PlanApo 60^o, 1.45 NA objective was used. In the experiments on sapphire and Olympus coverslips, Olympus Apo 100, 1.65 NA objective was used. Excitation light totally internally reflects at the interface and produces an evanescent wave on the aqueous side of the interface. Excitation light was s-polarized (perpendicular to the incidence plane) resulting in the same linear polarization of the evanescent field. The evanescent field decays

exponentially in the Z dimension with penetration depths of ~200 nm (for 1.45 objective) and ~65 nm (for 1.65 objective). Despite the higher refractive index of the muscle (~1.37), TIR occurs where the glass substrate meets the myofibril because the incident angles utilized are $>70^\circ$ (for 1.45 objective). The sample rests on a moveable piezo stage (Nano-H100, Mad City Labs, Madison, WI) controlled by a Nano-Drive. This provides sufficient resolution to place the region of interest in a position conjugate to the aperture. The fluorescent light is collected through the same objective and projected onto a tube lens, which focuses it at the conjugate image plane. A confocal aperture or an optical fiber (whose core acts as a confocal aperture) is inserted at this plane. The aperture was 50 or 4 μm in diameter for NA 1.45 and 1.65 objectives, respectively. An Avalanche Photodiode (APD, Perkin-Elmer SPCMAQR-15-FC) collects light emerging from the aperture.

Size of the confocal aperture

The confocal aperture should be as large as possible to maximize the signal, but it makes no sense to make its projection on the sample plane smaller than the optical resolution (~0.25 μm) of the objective used here (NA 1.45). The diameter of the projection of the aperture on the object plane is equal to the diameter of the confocal aperture (D) divided by the magnification of the objective ($M = 60$), making the optimal size of the confocal aperture $D = M \times R = 15 \mu\text{m}$. Since there are no commercial optical fibers of this size, we used the closest available size: 8 μm single-mode fiber.

Fluorescence measurements

The quartz slide with sample (or sample with background) was attached to a semi-cylindrical glass prism using glycerol ($n=1.475$) as an index matching fluid. This combined sample was positioned on a precise rotary stage, but equipped with a longer (20 cm) arm for a detection fiber mount. The arm has a possibility of movement in vertical axis. This modification increased the angular resolution (below 0.1 degree) and allowed a better adjustment for the signal optimization.

Fluorescent lifetime measurements in solution

Fluorescence lifetimes were measured by the time-domain technique using the FluoTime 200 fluorometer (PicoQuant, Inc.). The sample contained 1 μM F-Actin labeled with 100 nM Alexa488 dye. The measured concentration of dye was 0.1 μM . The excitation was by a 470 nm laser pulsed diode, and the observation was through a monochromator at 510 nm with supporting 550 nm long wave pass filter. The intensity decays were analyzed in terms of the multiexponential model using FluoFit software (PicoQuant, Inc.).

Fluorescent lifetime measurements in cardiac muscle

Fluorescence lifetimes were measured by the time-domain technique using a MicroTime 200 Instrument coupled to an Olympus IX71 Microscope (PicoQuant, GmbH, Berlin, Germany). Excitation was achieved using a 470 nm pulsed laser diode, and the observation was made through a 500 nm long wave pass filter. FWHM of pulse response function was 68 ps (measured by PicoQuant, Inc.), while the time resolution was better than 10 ps. The intensity decays were analyzed in terms of a multiexponential model using SymPhoTime v. 4.3 software (PicoQuant,

Inc.). The intensity-average lifetime was calculated as $\tau_j = \sum_i (f_i \tau_i)$ where $f_i = (R_i \tau_i) / (\sum_i R_i \tau_i)$ and R_i is the fractional contribution of the i -th lifetime, τ_i . The amplitude average lifetime was calculated as $\langle \tau \rangle = \sum_i R_i \tau_i$. The lifetimes of free and bound Alexa488-phalloidin in water and glycerol were measured with/in a FluoTime 200 fluorometer (PicoQuant Inc.) equipped with a microchannel plate and 470 nm pulsed laser diode (76 ps half-width).

Anisotropy and lifetime measurements

Anisotropies were measured by time-domain technique using FluoTime 200 fluorometer (PicoQuant, Inc.). The excitation was by a 475-nm laser pulsed diode, and the observation was through a monochromator at 575 nm with a supporting 550-nm long wave pass filter. FWHM of pulse response function was 68 ps (measured by PicoQuant, Inc.). The intensity decays were analyzed in terms of a multi-exponential model using FluoFit software (PicoQuant, Inc.).

Spatial Sampling

The pixel size of the camera is 16 μm x 16 μm . For the 100x NA 1.65 objective with 532 nm illumination, the Rayleigh resolution limit was ~ 200 nm. According to the Nyquist sampling theorem, the ideal spatial sampling rate should have been $200/2.3 \approx 90$ nm. The back projected size of the pixel of the camera was $16 \mu\text{m}/100 = 160$ nm. Therefore the images are under-sampled by a factor of $160/90 \approx 1.8$. For the 60x NA 1.45 objective, the back projected size of the pixel of the camera was 267 nm and the images are under-sampled by factor of ~ 3 . Under-sampling allows the light to be concentrated on fewer pixels. Under the present low-light conditions, this creates a signal that has greater amplitude relative to the background noise, and therefore boosts Signal-to-Noise (S/N) ratio.

Temporal Sampling

The whole field (512 x 512 pixels) was collected at time intervals τ . The choice of τ is crucial in Single Molecule Detection (SMD). Decreasing τ increases time resolution but decreases the number of fluorescent photons detected from each half-sarcomere. Increasing τ improves S/N ratio but decreases time resolution. We used $\tau=200$ ms, a reasonable compromise since the characteristic time for ATP hydrolysis by glycerinated skeletal myofibrils is in the 0.5 – 2 sec range (25). Five hundred (500) images (100 s) of data were collected.

Photon counting

The quantum efficiency of the APD is ~65% at 500 nm, the dark count is ~10 cps and it can count up to 107 counts/sec. The APD's TTL pulses were counted by a counter/timer on an plug-in card (National Instruments PCI-6601) controlled by a custom LabVIEW program using DAQmx software drivers. The PCI-6601 was a timing and digital I/O device with four 32-bit counter/timers and up to 32 lines of TTL/CMOS-compatible digital I/O. The 6601 card was a completely switchless/jumperless device and required only software configuration. It derived most of its functionality from the NI-TIO, a counter and digital I/O Application Specific Integrated Circuit (ASIC) developed by NI. To attain complete hardware timing and synchronization, multiple successive measurements were made in a buffered even counting mode. In this mode counters were read “on the fly” with sampling rates approaching 1 MHz. The result of each measurement was saved in the Hardware Save Register on each active edge of the GATE signal. The GATE signal indicates when to save the current counter value. A buffered measurement generates a data stream, which is transferred to a PC via Direct Memory Access (DMA) or is interrupted. Counting continued uninterrupted regardless of the GATE activity.

Photon counting eliminated the need for a frame-grabber and allowed direct 32-bit counting by a PC. Two counters were read simultaneously at the rising edge of the GATE signal provided by the Nano-Drive controller.

SMD measurements

The experiments were carried out in a SMD microscope, operating in either total internal reflection fluorescence (TIRF) or a transmitted (T) light mode. An experimental chamber was made by placing a sample on an NML-coated coverslip, sealing the sides around it with Vaseline, and covering it on top with a 24 x 24-mm glass coverslip (Fisher Scientific, Pittsburgh, PA). The chamber was placed on a moveable piezo stage (Nano-H100, Mad City Labs, Madison, WI) that was installed on the stage of an Olympus IX71 microscope. Experiments in TIRF mode were done using a commercial Olympus TIRF adaptor (Olympus, Center Valley, PA). The sample was placed NML-coated coverslip down. Experiments in T mode were done using a 1 mW beam of 543 nm light from an HeNe laser (LGP-193-249, Melles Griot, Carlsbad, CA), which entered through the back port of an Olympus IX71 microscope and was focused by the objective (Olympus PlanApo 603, 1.45 NA) on a sample plane. The sample was placed NML-coated coverslip up. The focal spot was $\sim 0.5 \mu\text{m} \times 0.5 \text{mm}$. This spot was made to overlap with the projection of the confocal aperture on the sample plane by adjusting the xy position of the focal spot with a pair of micromanipulators attached to the beam-steering post. The piezo stage was used to place the ROI in a position conjugate to the confocal aperture. The same objective collected fluorescent light, which was then projected onto a tube lens. The lens focused light at the conjugate image plane. An optical fiber (whose core acted as a confocal aperture) was

inserted at this plane. An avalanche photodiode (APD) (SPCM-AQR-15-FC, PerkinElmer, Wellesley, MA) collected light emerging from the aperture.

Measuring ATPase activity

Myofibrillar ATPase activity was measured using Inorganic Phosphorus Reagent Kit (Pointe Scientific, Canton, OH); Reaction was initialized with adding 5 mM ATP to 50 μ L of 3 mg/ml myofibrils in Ca-rigor solution. Myofibrils were intensively shaken using a vortex mixer for 1 min at room temperature. Reaction was stopped with 0.95 ml of Pi-reagent, filtered through 1 ml pipette tip closed with cotton ball and dissolved in 2 mM SDS. Concentration of [Pi] in μ M was calculated as $A_{\text{sample}} \cdot 10 / A_{\text{standard}}$, where $A_{\text{standard}}=0.34$ is the absorption of a standard sample of 10 μ M Pi.

Calculations

The calculation of the electric field at the surface was done by ordinary Fresnel refraction theory. The calculation of the average power into the objective was done by first calculating the square of the electric field component at the fluorophore along its transition moment to find out its excitation rate. This rate was then multiplied by the emission from the fluorophore into the objective, calculated in the same way as before, i.e. by expressing the fields from the fluorophore in terms of sums of plane waves, and then applied to Fresnel theory.

Imaging

In the TIRF experiments, the Hamamatsu ImagEM CCD camera (Hamamatsu, Bridgewater, NJ) was mounted in the right exit port (model IX2 RSPC-2) of the microscope. The

left exit port contained a confocal aperture and Avalanche Photodiode to measure the number of photons emitted by muscle. Excitation light from an expanded DPSS laser beam (Compass 215M, Coherent, Santa Clara, CA) was projected by a polarization-preserving-fiber to a commercial TIRF attachment (Olympus) and high NA objective (Olympus 100X NA=1.65 or 60X NA=1.45). The totally internally reflected light produced an evanescent wave on the aqueous side of the interface. The sample rested on a moveable piezo stage (Nano-H100, Mad City Labs, Madison, WI) controlled by a Nano-Drive. The fluorescent light was collected through the same objective, projected onto a tube lens and to a calcite prism (Melles Griot, Carlsbad, CA) which split the fluorescent light into two orthogonally polarized components. The light was focused on the photosensitive area of the camera. The insertion of the calcite prism did alter by a few mm the position of the conjugate image plane, but it made a negligible difference to the focus because the high magnification objective (with long back focal distance) was used.

Image analysis

HCIImage software (Hamamatsu) was used. In a 512 x 512 image, a 4x4 pixels rectangular Region-of-Interest (ROI) was created containing one O-band. The Intensity Measurement tool was used to measure mean gray value of all the defined ROI's in all 500 images. This data was saved as tabbed text file. The ASCII file was plotted in Sigma Plot (Systat, San Jose, CA).

Data analysis

Data was analyzed by Sigma Plot 10 (SPSS, Chicago, IL).

CHAPTER III

CENTRAL HYPOTHESIS AND SPECIFIC AIMS

FHC is the leading cause of sudden death in athletes and young people with an estimated prevalence of about 1 in 500. It is transmitted in an autosomal dominant mode and is characterized by ventricular hypertrophy and sudden cardiac death. Clinically, it is characterized by an increase in cardiac muscle mass and disorganization of muscle cells and myofibrils. Extensive research has been carried out to identify the genes that cause the disease. It is a monogenic disease with a high level of genetic heterogeneity. Over the past 15 years, at least 9 genes, which cause FHC, have been identified. All the proteins encoded by these genes are sarcomeric proteins of the heart muscle. Hence, FHC is considered a disease of the sarcomere. However, relatively little is known about the molecular steps leading from the gene defect to the clinical phenotype. In this proposal, we look at one particular mutation, D166V, in the ventricular regulatory light chain 2. It was identified in 2003 by Richard et al and is a particularly malignant form of the disease with a poor prognosis rate. This mutation occurs at the last amino acid residue of the human cardiac RLC where valine replaces the normally occurring aspartic acid. One can hypothesize that the lever arm swing is inhibited by steric interference originating from the valine residue that replaces the negatively charged aspartate in the mutant heart muscle. The negative charge of the aspartic acid may be necessary for the elbow of the myosin lever arm to efficiently execute its swinging motion, enabling the power stroke, and replacement of this residue with a bulky valine prevents the efficient interaction of myosin with actin. Thus, the D166V mutation may exert its action through changes in the kinetics of myosin cross-bridges

leading to an inefficient utilization of ATP by the mutated myocardium. This dysfunction can be caused by an increased or decreased rate of cross bridge detachment, whereby FHC myosin heads will be forced to detach from actin early, or have a delayed detachment rate. Early/delayed detachment implies consumption of ATP without contributing to force generation or excessive consumption of ATP to generate force, i.e. decreased efficiency. The myofilament incorporation of mutant sarcomeric proteins may change contractile function and, as a consequence, the heart would try to compensate. Because the human heart has a limited capacity for increasing cell number, any increase in cardiac performance must occur by the enlargement of existing cardiomyocytes, or hypertrophy. Also, if slow detachment rate of the fibers could start to fuse with the next contraction when heart rates are high, contributing to diastolic dysfunction. If severe enough, this factor could affect diastolic filling of the heart sufficiently to result in systolic dysfunction, *i.e.*, a decrease in stroke volume. This ultimately would cause the heart to compensate by increasing wall thickness (hypertrophy).

We hypothesize that the D166V mutation of RLC leads to alterations in myosin cross bridge kinetics and ultimately affects the interaction of the thick and thin filaments during cardiac muscle contraction.

Our objective is to study the functional consequences of this FHC RLC mutation. Also, methods will be devised towards testing this in human patients with high efficiency and accuracy.

To test the hypothesis, we propose the following specific aims:

Specific Aim 1: Study the kinetics of single cross bridge in healthy working muscle (skeletal).

Specific Aim 2: Study the molecular mechanisms involved in contraction in cardiac muscle carrying the FHC mutations in myosin RLC.

Specific Aim 3: Develop methods to improve imaging in muscle.

CHAPTER IV

SPECIFIC AIM 1

Specific Aim 1: Study the kinetics of single cross bridge functioning in healthy muscle.

Rationale:

We aim towards studying the dynamics of cross bridge interaction in muscle and not in solution, as the behavior of proteins in muscle are quite different than in muscle. The reasons being that in solution, the proteins are loosely packed, whereas in muscle, they are crowded. Molecular crowding influences the protein solubility and conformation in solution, which may impose constraints affecting both the structure and function of enzymes. In addition, it is important to study as few cross bridges as possible. The reason for it is that myosin cross bridges act asynchronously, i.e., at any time during muscle contraction each one is in a different part of the mechanochemical cycle. Therefore measurement taken from an assembly of cross-bridges at any time during contraction will be an average value and likely to obscure details of cross-bridge kinetics. The effect of crowding is particularly severe in muscle, as the concentrations of actin and myosin are 0.6 μM and 0.24 μM , respectively. These proteins are meant to operate in such crowded environments, as evidenced by the fact that their K_m value is in the micro molar range. Crowding imposes constraints affecting both their structure and function. Also, actin and myosin

are arranged in regular arrays of thin and thick filaments where the kinetics of their interactions depends on their relative position.

In this specific aim, a single cross bridge has been studied to understand the kinetics that occur during contraction in muscle. The objective of project is to examine the molecular determinants of the D166V induced malfunction of the heart. To do so, it is necessary that we first understand the working in a healthy muscle, specifically, skeletal muscle.

Due to its organized nature, we expect to get a better grasp on the working of muscle as well as in achieving detection of a single cross bridge.

To understand the kinetics, we study the a) rotation of actin monomers during isometric contraction and the b) duty cycle in muscle.

a) Rotation of actin monomers during isometric contraction

Introduction

Muscle contraction is caused by cyclic interaction of myosin heads with actin filaments driven by hydrolysis of ATP. The question arises whether, during steady-state isometric contraction in muscle (where no global work is produced), myosin heads perform a mechanical cycle at all. While the crystal structure of subfragment-1 (S1) (51) indicates a potential for large conformational change, and there is solid evidence that the C-terminal part of S1 rotates during translation of myosin along actin in vitro, (92, 41) the situation may be quite different during steady-state isometric contraction of muscle. Under truly isometric steady-state conditions, the extent of the power stroke may be limited. In the extreme case, where there is no series elasticity, the rotation may be prevented altogether (54).

There are two ways of studying cross-bridge mechanics in muscle under isometric conditions. The first way is to use mechanical transient methods, during which a rapid step is applied to synchronize the cross-bridges, and to follow relaxation back to steady state (14, 15, 47, 50). The second way is to passively observe the dynamics of a few cross-bridges without disturbing the steady-state condition. In muscle the two ways are not equivalent. In transient methods, rotation of cross-bridges is measured while they act against series elasticity, which is rapidly decreased following transient relaxation. In truly isometric contraction however, series elasticity is constant and equal to active tension. This is a more accurate reflection of behavior of muscle proteins during isometric state-state.

It is thus preferable to study cross-bridge dynamics in isometric muscle by the passive time-resolved method. Conventional steady-state measurements are not time-resolved (12, 15, 18, 85). This specific aim introduces such a method. It is based on fluctuation analysis of rotational anisotropy. In fluctuation analysis, signal-to-noise ratio is proportional to $N^{-1/2}$, where N is the number of detected rotating molecules (63). For this reason we seek to limit contributing molecules to just a few. The measurement of individual molecules in muscle is a complex task because concentration of myosin or actin in muscle is large (e.g. one cm long single muscle fiber contains $\sim 10^{13}$ myosin molecules). To observe just a few molecules in muscle it is necessary to decrease the number of active cross-bridges, or to collect data from an extremely small volume. The conventional wide-field microscope cannot be used for this purpose because its detection volume is much too large ($\sim 10^{-9}$ L) containing $\sim 10^{11}$ myosins. High aperture objectives forming diffraction-limited illuminated spots and confocal detection made it possible to limit the detection volume to ~ 0.5 femtoliter (10^{-15} L) and eliminate much background, (36) but half of a femtoliter is still far too large to optically isolate just a few myosin molecules.

An application utilizing Total Internal Reflection (TIR) has been described here. The method has never been applied before to the whole tissue.

In this work, the orientation changes of actin filaments labeled with fluorescent phalloidin were studied.

Phalloidin attaches to actin rigidly and rotates in synchrony with an interacting cross-bridge (15). Studying actin rotation has four critical advantages:

1. Labeling of actin with phalloidin, in contrast to labeling myosin at Cys707, does not affect enzymatic properties of muscle (28, 73). Myofibrils are well preserved, because labeling does not require harsh conditions, such as raising the temperature to label myosin light chains.
2. Phalloidin labels the overlap zone (80). Redistribution of phalloidin to the I-band takes several hours, (3) so only those actin protomers that are located in the region where interactions with myosin occurs are studied.
3. By saturating all actins with a mixture of labeled and unlabelled phalloidins, the final concentration of label is easily controlled. For example, in the present experiments we used 0.01 μM fluorescent-phalloidin and 9.99 μM unlabeled phalloidin, i.e. we could be sure that on average only 1 in 100 actin monomers in a thin filament carried fluorescent probe.
4. Fluorescence of phalloidin increases upon binding to actin. This increases S/N ratio. To avoid shortening during contraction, myofibrils were lightly cross-linked with 1-ethyl-3-[3-dimethylamino)-propyl]-carbodiimide (EDC). The results support the view that during isometric contraction cross-bridges undergo mechanical cycles.

Results

The size of the observed volume

Fluorescent intensity at the microscope image plane is the convolution of the excitation and emission intensity profiles (95). The light intensity profiles are derived from geometrical optics and given by the Fraunhofer diffraction patterns from a circular aperture. Detected fluorescence is the intensity at the image plane integrated over the confocal pinhole. Thus the size and shape of the detection volume depends on the excitation beam profile, diffraction of emitted light through the microscope optics, and the size and shape of the confocal pinhole.

In CTIR the spatial distribution of the excitation field intensity decays exponentially in the dimension normal to the glass/water interface (Z -dimension) and is uniform in the lateral (XY) dimensions. The point spread function integrated over the pinhole aperture in image space (integrated PSF or IPSF) as a function of point source position sets boundaries for the detection volume appropriate for a point-like diffusing fluorescent sphere. Fig. 1A shows the IPSF for a NA 1.45, 60 X objective and a 3.5 μm confocal pinhole as a function of point source position in the object plane (XY -plane on the water side of the interface). Fig. 1B shows the IPSF for the same objective and pinhole but for the point source position in an axial plane (YZ -plane on the water side of the interface). The Z -dimension dependence is exponential with a depth of field of ~ 100 nm.

The effective detection volume was calculated by deploying a rectangular solid lattice of identical chromophores in object space. The lattice filled the volume occupied by water and sample in a real experiment. A single chromophore, the principal chromophore, occupies the point of maximum intensity of the IPSF in Fig. 1. Fluorescence detected from each chromophore was summed. The minimum unit cell volume is defined as that dimension when the principal

chromophore fluorescence accounts for more than half of the total fluorescence collected. The IPSF shown in Fig. 1 has a minimum unit cell with XYZ-dimensions of 186 x 186 x 86 nm. Four unit cells surround the principal chromophore defining the void to be filled by the effective detection volume. IPSF symmetry suggests the void be filled with the largest possible ellipsoid forming the effective detection volume of ~ 7 attoL.

Determining the position of the conjugate area

In experiments on muscle it is important to place the A-band of myofibrils exactly at the sample plane position that is conjugate to the detector. To determine the exact position of conjugate area, a sharp edge was translated through a projection of 3.5 μm aperture onto the sample plane. A razor edge was mounted on the moveable stage driven by a servo motor. To determine the Y coordinate, the edge was translated in the X direction in 0.1 μm steps. Light was detected only when the edge was near the line defined by the Y coordinate. To determine the X coordinate, the edge was translated in the Y direction along the line defined previously by the Y coordinate. Fig. 2 shows a contour map of the normalized intensity profile when the edge was translated in X and Y directions. Red and violet colors correspond to the maximal and minimal intensity of transmitted light, respectively. The intersection of the profile lines defines a position of conjugate area with respect the center of the eyepiece reticle. The coordinates of this area were X=1 μm , Y=1 μm . The A-band was placed within this area.

Measuring TIRF polarizations

We measured the polarized fluorescence of standard samples with known polarizations and compared it with polarization obtained with TIRF illumination. The sample was poly(vinyl

alcohol) (PVA) film doped with N-methyl-4-(pyrrolidinyl)-styrylpyridinium iodide (MSSPI) dye, in which transition dipoles are aligned in one direction by stretching the PVA film during polymerization. MPSPI has a large Stokes shift and high polarization across absorption and emission spectra. Fig. 3 shows the signal from a typical film. The elongated shape of MPSPI allows good orientation in stretched samples. Polarization values are listed in Table 1 below.

Table 1. Polarizations of samples.

Sample	P_{\parallel} (EPI)	P_{\perp} (EPI)	P_{\parallel} (TIRF)	P_{\perp} (TIRF)
Oriented film	0.834	-0.396	0.749	-0.409

Polarization of solid PVA film doped with MSSPI dye, in which transition dipoles are aligned in one direction by stretching the PVA film during polymerization. The average horizontal and vertical polarizations are defined as $P_{\parallel}=(F_{\parallel}-F_{\perp})/(F_{\parallel}+F_{\perp})$ and $P_{\perp}=(F_{\perp}-F_{\parallel})/(F_{\perp}+F_{\parallel})$, where F_{\parallel} & F_{\perp} are fluorescence intensities obtained with light polarized parallel and perpendicular to muscle axis.

Horizontal and vertical (EPI) polarizations were comparable to the values obtained by a dedicated apparatus using low numerical aperture (0.15) objective ($P_{\parallel}=0.903\pm 0.003$ and $P_{\perp}=-0.630\pm 0.005$, respectively), consistent with the value reported earlier (45).

The other samples with known polarizations were rhodamine B in 100% glycerol (theoretical $P=0.5$, observed $P=0.501$), un-stretched (immobile) PVA doped with rhodamine B (theoretical $P=0.5$, observed $P=0.333$) and rhodamine B in water (theoretical $P=0.056$, observed $P=0.111$). The deviation from the ideal value is caused by unequal sensitivity of the APD and by the microscope optics.

Number of observed actin monomers

Since $\sim 20\%$ of muscle weight is actin, the concentration of actin in a solution of 1 mg/mL myofibrils is $\sim 4.6 \mu\text{M}$. We used $0.01 \mu\text{M}$ phalloidin. Since there is ~ 400 actin protomers in a filament, there is on average ~ 1 phalloidin molecule per actin filament. If the phalloidin was uniformly distributed, $0.3 \mu\text{m}$ wide detection volume would have contained ~ 0.3 phalloidins/filament. However, because of non-homogeneous distribution of phalloidin (Fig. 5) most of the fluorophores are located in distal $\sim 1/3$ of a filament. We therefore detect signal from ~ 1 phalloidin/filament. Spacing between actin filaments is $\sim 30 \text{ nm}$. Since the thickness of the detection volume is $\sim 100 \text{ nm}$, we observe ~ 3 layers of thin filaments. There are ~ 4 filaments in each layer. We conclude that we observe ~ 12 actin monomers labeled with phalloidin.

To verify this number experimentally, we constructed a calibration curve relating the intensity of fluorescence to the number of molecules contributing to a signal. 1 mg/mL myofibrils were labeled for 5 mins at room temperature with a mixture containing 0.01, 0.05, 0.1 or $0.5 \mu\text{M}$ rhodamine-phalloidin complemented with 9.99, 9.95, 9.90 and $9.5 \mu\text{M}$ unlabeled-phalloidin, respectively. Assuming that actin is distributed continuously throughout the experimental volume, the number of rhodamine-phalloidin molecules in 7 attoL volume is 4, 20, 40 and 200 for myofibrils labeled with 0.01, 0.05, 0.1 and $0.5 \mu\text{M}$ rhodamine-phalloidin, respectively. The average number of photon counts of parallel polarized intensity was measured for each concentration of the dye. The result is shown in Fig. 4. The number of observed molecules was estimated from this calibration curve by measuring the average fluorescence emanating from labeled sample. In general, the number varied between 4-20 fluorescent actin monomers.

The data of Fig. 4 allowed to estimate Signal-to-Noise (S/N) ratio in the experiment. The S/N ratio is determined by the rate of detection of fluorescent photons per molecule of the dye during one bin width $\delta\tau$ (62). We detected on average ~ 2.5 counts/bin/molecule for parallel component of polarization signal. Perpendicular component is ~ 0.8 x parallel component, giving a total of ~ 4 photons/molecule/bin. Assuming Poisson distributed shot noise as the sole noise source, the S/N ratio is ~ 2 .

Fluctuations of contracting myofibrils

Myofibrils were placed on a cover slip and thoroughly washed with Ca-rigor. The flow removes free floating myofibrils and those that are weakly attached to the glass, leaving only those that are strongly adhering to the top or bottom surfaces. A myofibril attached to the bottom surface is shown in Fig. 5A. To visualize the size of the confocal aperture, the fifth sarcomere from the bottom was magnified 10x and is shown in Fig. 5B. The projection of 4 μm aperture onto the sample plane is shown as a black dot. The schematic diagram of detection volume is shown in Fig. 5C.

Typical signals obtained from the detection volume placed in the overlap zone of rigor and contracting myofibril are shown in Fig. 6A & B, respectively. The bleaching resulted in loss of all signal within ~ 50 -60 sec. The background was ~ 50 cpb. It is due to auto fluorescence from glass, and could be decreased ~ 2 -fold by using quartz coverslips. The time course of polarization ratio for rigor and active myofibrils were formed using the formula $P_{\parallel} = (F_{\parallel} - F_{\perp}) / (F_{\parallel} + F_{\perp})$. From each time-course is subtracted a best fitting line to remove the zero frequency (DC) component of its power spectrum leaving time-courses that have zero mean polarization ratio (the AC component or P_{ac}) and fluctuations characterized by the root mean squared (rms) deviation

$(\langle \Delta P^2 \rangle)^{1/2}$. We investigated frequency dependence in the polarization fluctuations with the power spectrum (PS) computed from Pac using fast Fourier transform (FFT) with a Bartlett window (Mathematica, Wolfram Research, Champaign, IL). Spectral intensities were binned in 0.5 Hz intervals. The difference PS, constructed by subtracting rigor PS from active PS, defines excess PS from active myofibrils. Excess PS characterizes the rate of orientation change of the phalloidin transition dipole. Average excess PS computed from 23 myofibrils along with error bars indicating standard error of the mean (n=23) is shown in Fig. 7 (top). The average excess PS was > 0 at every frequency detected and relatively flat. Paired, two sided, t-test shows that excess PS differs significantly from zero (i.e., $P \leq 0.05$) at every frequency (Fig. 7, bottom).

The ATPase of uncrosslinked myofibrils was $f_{\text{ATP}} = 131 \pm 2$ $\mu\text{molePi}/\mu\text{mole myosin}/\text{min} = 2.2$ Hz. Cross-linking increased ATPase of uncross-linked myofibrils 1.2 ± 0.07 fold.

Controls

(i) We have considered the possibility that the difference between contracting and rigor muscle is due to the movement artifact, i.e. that the cross-linking was not sufficient to inhibit shortening. To make sure that this was not the case, myofibrils were always tested for shortening after cross-linking. Fig. 8 shows a typical example of two fluorescent images of the same myofibril in rigor (Fig. 8A) and few minutes after adding contracting solution (Fig. 8B). The mean \pm SD sarcomere length of rigor and contracting myofibrils was $2.77 \mu\text{m} \pm 0.14 \mu\text{m}$ and $2.78 \mu\text{m} \pm 0.12 \mu\text{m}$, respectively. The paired t test showed that the difference was not statistically significant ($t=0.42$, $P=0.68$, 8 degrees of freedom).

(ii) To rule out the possibility that cross-linking affects polarized fluorescence, we measured the degree of cross-linking. Cross-linking increased ATPase of myofibrils 1.2 ± 0.07 fold. In solution, cross-linking of skeletal rabbit S1 to F-actin accelerates ATPase 200-300 fold (68) suggesting unlabeled cross-linked myofibril preparation contains 1-2% cross-linked cross-bridges.

FIGURES

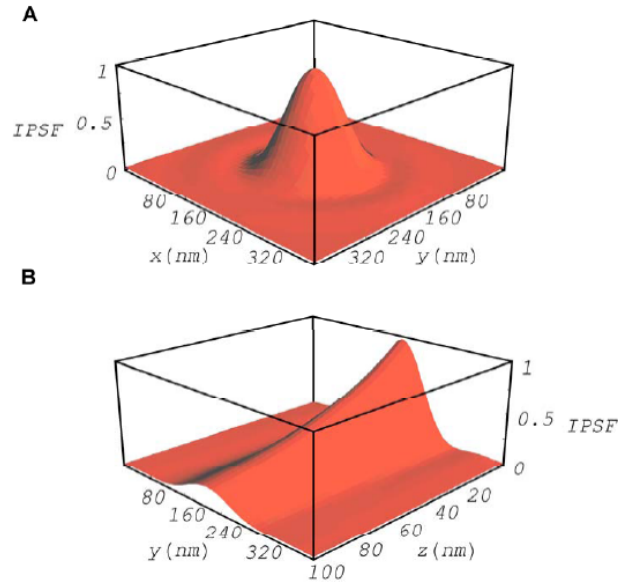


Fig. 1. The calculated relative detected intensity from a point-like fluorescent sphere (FS) near the focus of a NA 1.45, 60X objective as a function of FS position in lateral (X,Y) and axial coordinates (Z). Calculation utilizes the point spread function integrated over the 3.5 μm confocal pinhole aperture to give the integrated point spread function or IPSF. Panel A is the IPSF for lateral FS position. Panel B is the exponentially decaying IPSF for the axial FS position. The IPSF defines the effective detection volume using arguments outlined in the text. For this IPSF, the effective detection volume is ~ 7 attoL.

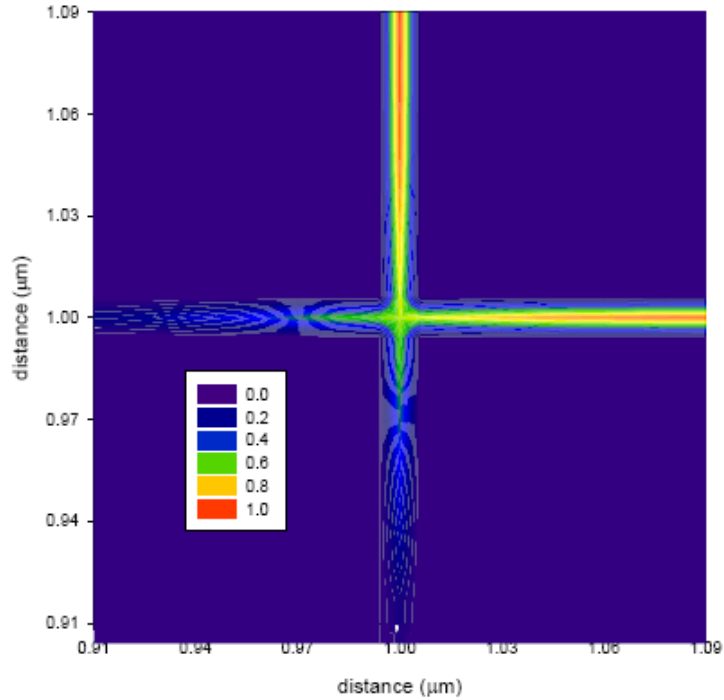


Fig. 2. Defining area on the sample plane conjugate to image plane. Contour map of the normalized intensity profile of the sharp edge translated in X and Y directions in 0.1 μm steps. Red and violet colors correspond to the maximal and minimal intensity of transmitted light, respectively. The intersection of the profile lines defines position of the conjugated area relative to the center of the eyepiece reticle.

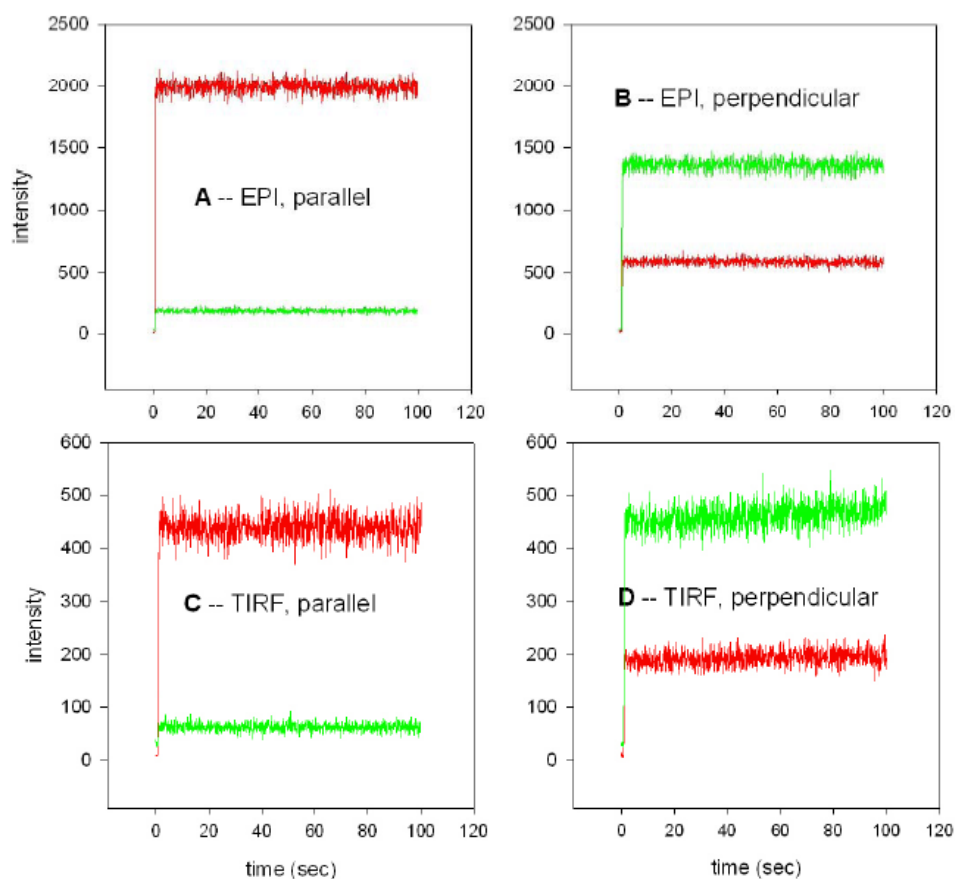


Fig. 3. Polarization signal obtained from oriented PVA film. A) polarization of the excitation laser beam parallel to the axis of the film, emission parallel- (red) and perpendicular to the axis of the film (green); B) polarization of the excitation laser beam perpendicular to the axis of the film, emission colors as before; C ; D) same as in A, B with TIRF excitation, laser beam at $\sim 69^\circ$ to the plane of the film. The excitation intensity was attenuated 1000 times (to $25 \mu\text{W}$).

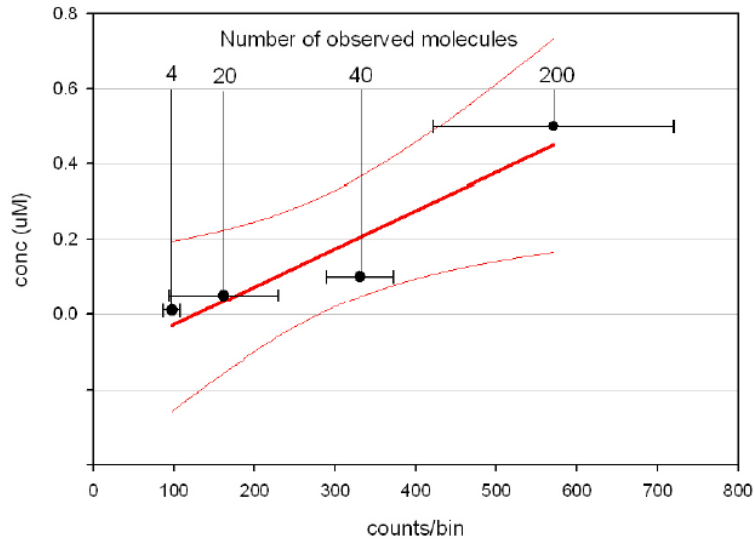


Fig. 4. The calibration curve (thick red line) that is used to estimate the number of fluorescent cross-bridges in the detection volume. The horizontal axis is the average \pm SEM intensity of the parallel intensity component of a fluorescence signal. The vertical axis is the corresponding concentration of fluorophores. The numbers point to the calculated number of fluorescent molecules in the detection volume. The narrow red lines denote 95% confidence limits.

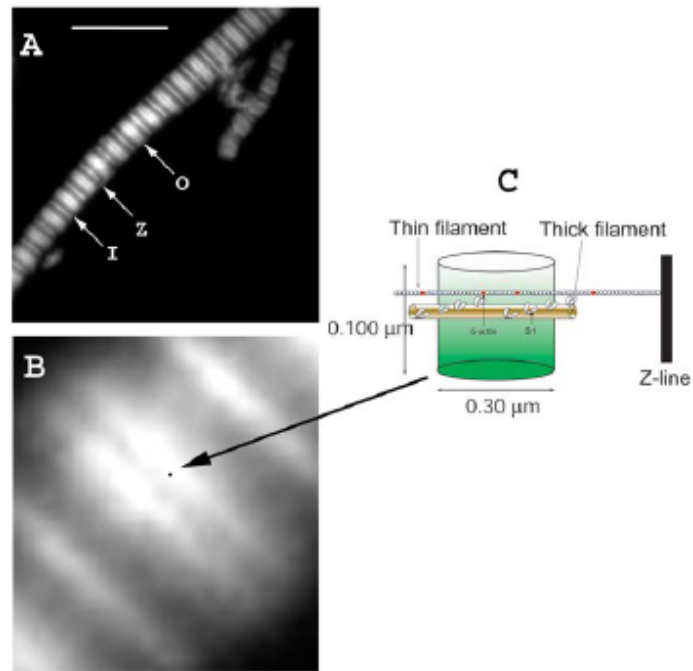


Fig. 5. TIRF image of myofibril in rigor. A) myofibril labeled with 0.1 μM fluorescein phalloidin on actin filaments. Z is the Z-line, O is the overlap zone, I is the I-band. Bar is 10 μm. B) fluorescent image magnified 10x. The black dot is a projection of the confocal pinhole on the image plane. C) schematic diagram of the detection volume. The fluorescently labeled actin monomers are red.

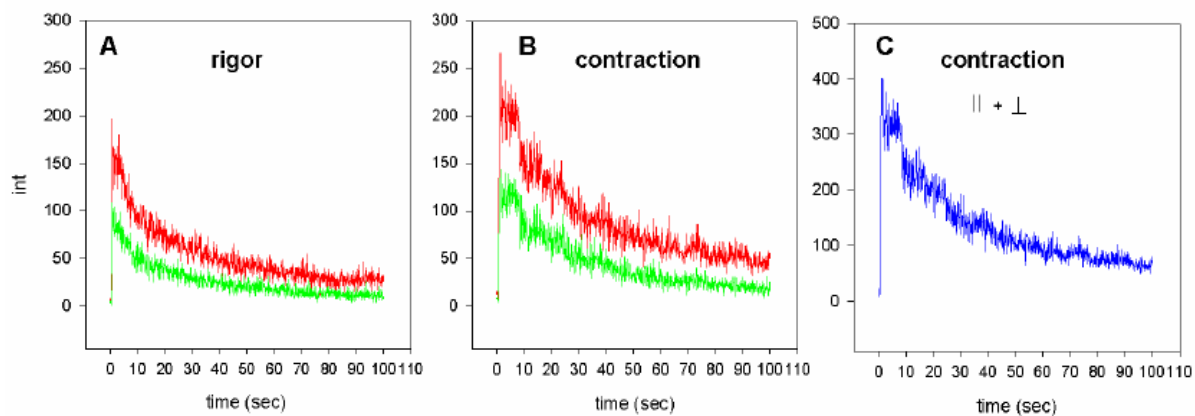


Fig. 6. Polarization signal obtained from rigor (A) and contracting (B) myofibril. Polarization of the excitation laser beam parallel to the axis of the myofibril. Emission parallel (red) and perpendicular (green) to the axis of the myofibril. 0.01 μM phalloidin. C) Sum of parallel and perpendicular intensities.

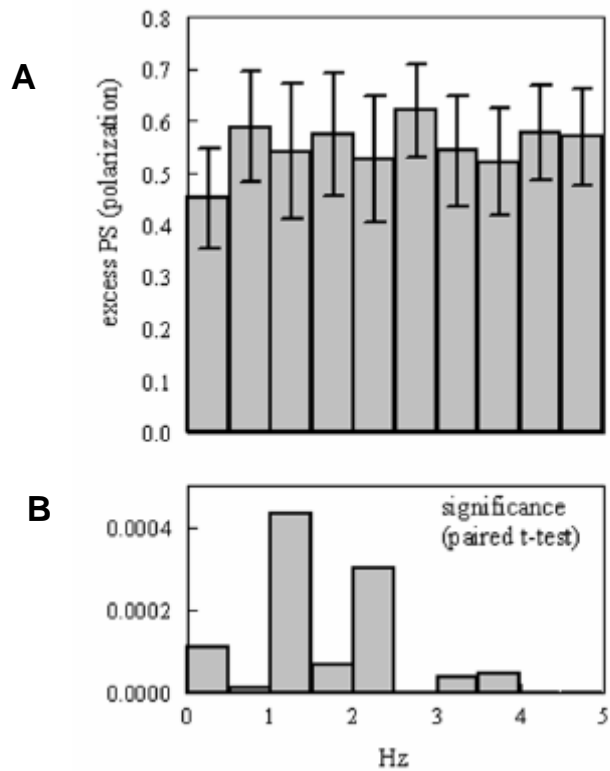


Fig. 7. Average polarization excess PS (A) and the t-test significance level that data in A is not different from zero (B) for experiments on 23 different myofibrils . Error bars show SEM for n=23.

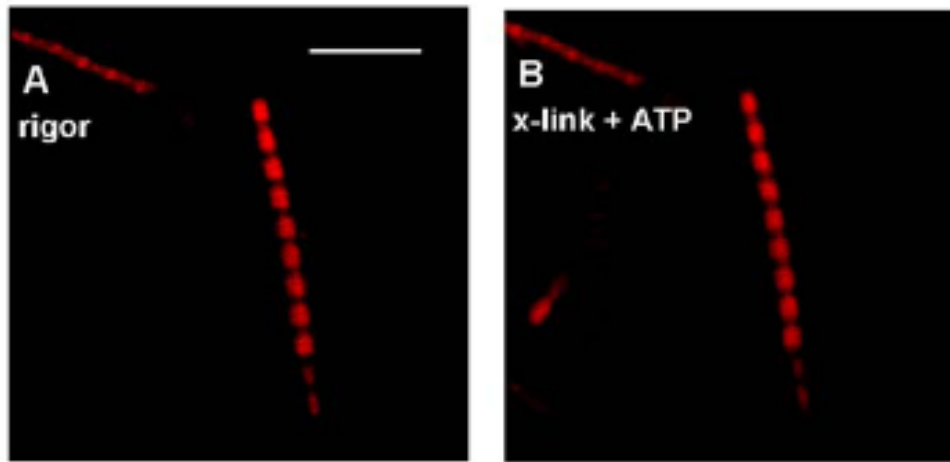


Fig. 8. Cross-linked myofibrils in rigor solution (A) and after adding contracting solution (B).

Bar=20 μm .

Discussion

The main finding of this part of the specific aim is that actin monomers rotate during isometric contraction of myofibrils. Since rotation of actin is a result of interaction with myosin heads, (15) the present results suggest that cross-bridges rotate during isometric contraction, just like in muscle or during translation along actin filaments. We recognize that rotation of the head does not necessarily mean that the C-terminal part of myosin undergoes power stroke, because the C-terminal part is separated from the head by a flexible link (66).

We excluded 4 possible reasons why observed fluctuations could be artifactual:

1. *The spectra represent spurious contributions such as diode shot noise, other instrumental noise or vibrations of the microscope.* This may not be the case as the power spectra that was taken into account represented the excess power of contracting over rigor muscle.

2. *The oscillations reflect movement artifact.* It is an established fact that cross-linking effectively eliminates shortening. 1-2% cross-linked cross-bridges probably do not affect the polarized fluorescence power spectrum since spectrum amplitude is most likely linear with the number of cross-bridges. In all 23 experiments lasting 100 sec, we did not note any shortening or change in the position of the observed overlap zone. We would easily have been able to detect translation of 0.5 μm , i.e. to escape detection, shortening would have to be less than 5 nm/sec. The distance between actin monomers is 5.5 nm and 1 in 100 actins were fluorescently labeled. We observe ~ 3 layers of filaments, i.e. the translation would have resulted in light spikes every 30 sec (frequency 0.03 Hz), well below frequency range of interest. Besides, we measure polarization; so any change in translational motion should not influence the results.

3. *The oscillations result from gradients of ATP concentration.* The experiments performed were steady-state experiments, i.e. contraction was initiated by addition of ATP. Gradients could have

been generated when imposing rapid increase in ATP concentration by rapid photolysis of caged ATP, but not in our steady-state experiments.

4. *The oscillations result from photobleaching.* This is not very likely, because photobleaching was eliminated from analysis by subtracting DC component before taking Fourier Transform. There are two additional reasons why photobleaching is unlikely to cause excess power in signal of contracting muscle. First, bleaching results from the stepwise loss of fluorescence of ~12 fluorophores in ~50 sec (e.g. data of Fig. 7). Therefore frequency associated with bleaching should be $\sim 12/50 \text{ sec} \sim 0.24 \text{ Hz}$, well below frequency range of interest. Second, fluorescence of rigor myofibrils bleached at about the same rate as the fluorescence of contracting myofibrils.

The steps visible in data of Fig. 7B could arise either from photobleaching of rhodamine or reflect rotational motion of the transition moment. We think that the former is the case for the following reasons: First, the intensity steps in both orthogonal components of fluorescence occurred in synchrony, suggesting that they do not reflect rotational motion. Second, steps occurred as well in rigor muscle, where no rotational motion took place. Third, the number of steps roughly corresponded to the number of fluorophores in the detection volume.

Each step lasted ~10 sec and led to the loss of ~100 cpb (Fig. 7C), i.e. we observed ~10,000 photons from a fluorophore before it photobleached. The geometrical collection efficiency of the instrument is ~2%, i.e. a fluorophore emitted total of 0.5×10^6 photons before irreversible bleaching. This is consistent with known photostability of Rhodamine (35).

The ability to measure properties of a small number of molecules in a live cell is important because it probes molecules in their native crowded environment. This may be responsible for observations which suggest that the motility in solution may be accomplished differently than in muscle. Thus, the sliding distance in an *in vitro* assay (near zero load) was

reported to be greater than 100 nm during one ATP hydrolysis cycle. Force generation did not coincide with the release of ADP and instead myosin head *in vitro* was shown to produce force several hundreds of milliseconds after bound nucleotide was released. In relaxed scallop muscle, the rotation of the regulatory domain was not coupled to a specific step in the ATPase cycle. Our results suggest that individual molecules can be studied in working muscle.

b) Duty cycle in muscle

Introduction

From the analysis of crystal structures of different forms of myosin, single-molecule studies, spectroscopic experiments, and X-ray diffraction of muscle fibers, a picture of the cross-bridge cycle emerges that suggests that during muscle contraction a cross-bridge assumes at least two distinct conformations: strongly attached to actin and dissociated from it (76, 78, 82). It is believed that a strongly attached cross-bridge produces contractile force.

Cross-bridge is in a strongly attached state for a period of time t_s , after which the contractile cycle continues with a release of phosphate followed by the dissociation of ADP and the onset of rigor. Its end is marked by the binding of a fresh molecule of ATP and detachment of myosin from actin. Finally, ATP is hydrolyzed to ADP and phosphate, and the cycle repeats with the period t_c . In this scheme, the motion of switch I (a loop in the upper 50K domain of S1) is coupled to the actin binding cleft, and the motion of switch II (the loop which contains invariant glycine that forms a hydrogen bond with γ -phosphate of ATP) is coupled to the lever arm. The opening of switch I provides an exit route for Pi. The power stroke is initiated by actin binding to a myosin that contains hydrolysis products, via closure of the 50 kDa cleft. This is followed by opening of switch I, thereby reducing its interactions with switch II. This allows

switch II to open. It is possible that the power stroke occurs in two steps: the initial generation of force associated with the weak to strong transition of actomyosin (containing products of hydrolysis). This leads to the rotation of the whole myosin head before the internal structural change of switch II occurs. The motion of the head is followed by the swing of the lever arm that is associated with Pi release (84).

In vitro evidence, based on observation of the individual steps of skeletal actin, smooth myosin (74, 92) and myosin V, (41, 100) suggests that the duty cycle DC,1 defined as the ratio of t_s/t_c , is small for cross-bridges acting against zero load (48, 57, 89). Here we report the attempt to measure DC of a single cross-bridge in muscle. We were motivated by realization that DC could be measured directly if the individual impulses could be visualized during isometric contraction. Individual impulses can only be visualized if single molecules were observed. Observation of individual molecules in a tissue is not a simple matter, especially in muscle where the concentration of protein is very large. The observation of a single molecule in muscle is reported here for the first time.

To illustrate how important it is to know the DC, consider a consequence of assuming that DC in isometric contraction is low (say 0.05). This is the value determined for a single myosin molecule in vitro. The value of DC is calculated as the ratio of maximal isometric tension (P) to tension developed by one cross-bridge (p), normalized by the number of cross bridges in a cross-section of muscle (N), $DC = P/(pN)$ or $p = P/[(DC)N]$. Taking isometric tension as $4.1 \times 10^5 \text{N/m}^2$ and the number of myosin heads in one half-sarcomere as 1.76×10^{17} in 1 m^2 cross-section of muscle gives $p = 47 \text{ pN}$. This is 8 times larger than the value determined experimentally (5.7 pN). It also implies that the step size is 30 nm, whereas reported value is 10 nm. The value of DC which would have been consistent with measured P and p is $DC = 0.41$.

This value is close to the one determined experimentally by stiffness measurements. An intermediate value was obtained by Cooke et al. using electron spin resonance data. They observed that only 20% of the spin labeled myosin were bound to actin in isometrically contracting muscle. Similar results were obtained by Duong and Reisler, who showed that 25% of the myosin heads in calcium activated EDC-cross-linked myofibrils (not modified at SH1) were protected from tryptic digestion at the 50/20 kDa junction in the myosin heavy chain. Berger and Thomas confirmed these results and showed that this value increased to 37% at low ionic strength, presumably due to additional contributions from weakly bound cross-bridges. Berger and his collaborators estimated that close to 1/3 cross-bridges are active during isometric contraction. Thus, experiments that can directly measure the actomyosin interaction of a single cross-bridge under isometric conditions within the myofilament lattice are clearly needed to resolve these important issues.

In a strongly bound state the rotational freedom of a cross bridge is inhibited as demonstrated by the high anisotropy of cross-bridges in rigor (85). In a dissociated state, the rotational freedom is restored, as demonstrated by the low anisotropy of relaxed muscle (18). The same changes of anisotropy are observed in actin. Observing actin has a number of essential advantages that make study of single molecules in muscle possible. First, actin can be labeled specifically and stoichiometrically with fluorescent phalloidin, which allows strict control of the degree of labeling. Second, labeling with phalloidin has the advantage that, in skeletal muscle (in contrast to cardiac muscle); only the ends of thin filaments are initially labeled (80). This is the region (overlap zone, O-band) where actin and cross-bridges interact. Third, phalloidin does not alter enzymatic properties of muscle and does not impair the regular structure of a myofibril, like the less gentle labeling of myosin does.

Actin was labeled with a $10^5:1$ mixture of nonfluorescent: fluorescent phalloidin, assuring that on average less than one molecule of actin per half-sarcomere was fluorescent. The orientation was measured by monitoring intensities of the polarized TIRF images of half-sarcomere that contained no more than 3 actin molecules. Polarization could be measured because fluorescent phalloidin was partly immobilized by actin filaments. The polarized intensity closely followed polarization of fluorescence, which is an established probe of the orientation (87). During isometric contraction, but not during rigor, actin orientation oscillated between two values, corresponding to the actin-bound and actin-free state of the cross-bridge. The average cycle time t_c was 6 s. The cross bridge stayed attached to actin on average $t_s = 3.4$ s. These results suggest that in isometrically working muscle cross bridges spend about half of cycle time attached to actin, and that the bulk of the energy of ATP hydrolysis is used for purposes other than performance of mechanical work.

Results

Polarized intensity is a good measure of orientation

The established measures of orientation are polarization of fluorescence (P) or anisotropy (A) defined as $P=(I_{\parallel} - I_{\perp}) / (I_{\parallel} + I_{\perp})$ and $R=(I_{\parallel} - I_{\perp}) / (I_{\parallel} + 2I_{\perp})$ where I_{\parallel} and I_{\perp} are the fluorescence intensities of the vertically (\parallel) or horizontally (\perp) polarized emission when the sample is excited with vertically polarized light (87). In the present experiment, however, we found it convenient to measure only I_{\parallel} , because P and R are noisy due to division of two noisy signals. Moreover, the noise of P or R measurements is increased because regions-of-interest placed over corresponding orthogonally polarized sarcomeres are often slightly out of register. It is therefore essential to demonstrate that I_{\parallel} behaves like P or R . The inset to Fig.9A shows two orthogonal

images of a myofibril. Figure 1 compares the time course of horizontal intensity (A) with parallel polarization of fluorescence (B) defined as $[(I_{\text{left}} - I_{\text{bckl}}) - (I_{\text{right}} - I_{\text{bckr}})] / [(I_{\text{left}} - I_{\text{bckl}}) + (I_{\text{right}} - I_{\text{bckr}})]$ where I_{left} and I_{right} are the intensities of the corresponding half-sarcomeres in the left and right images, respectively, and I_{bckl} and I_{bckr} are the intensities of the left and right background immediately adjacent to a myofibril. It is seen that horizontally polarized intensity closely follows the polarization of fluorescence signal and is therefore a good measure of orientation.

For quantitative measurement of orientation, one needs to know whether the probe is at least partially immobilized by the protein so that the transition dipole of the fluorophore reflects the orientation of the protein. Fig. 10 shows that this is the case for fluorescent phalloidin labeling F-actin. The decay of anisotropy of fluorescein phalloidin is shown in Fig. 10A. 93% and 7% of the signal was contributed by the decay times of 0.444 and 0.093 ns, respectively. The longer correlation time is due to the rotation of phalloidin, and the shorter one to the independent rotation of fluorescein moiety. Thus the free rotation of fluorophore contributes negligibly to the signal. Fig. 10B shows the decay of anisotropy of fluorescein phalloidin coupled to F-actin. 28%, 69% and 3% of the signal was contributed by the decay times of 17.140, 0.421 and 0.087 ns, respectively. The longest correlation time is due to the rotation of F-actin oligomers, intermediate one to the rotation of phalloidin, and the shortest one to the independent rotation of fluorescein moiety. Thus a significant fraction of fluorescent phalloidin is immobilized by F-actin, and therefore contributes to the anisotropy of muscle (non immobilized phalloidin does not, because it rotates rapidly on the time scale of the measurement).

The fluorescent lifetime of phalloidin could be best fitted by three exponentials with lifetimes of 3.471, 1.708 and 0.044 ns and relative contributions of 63%, 33% and 4%,

respectively. The amplitude weighted lifetime was 2.156 ns. Binding to F-actin changed lifetimes by less than 1%.

Concentration of fluorophores needed to observe a single molecule in muscle

To establish conditions necessary to observe a single molecule of actin in muscle, we followed the course of photobleaching of a half-sarcomere containing actin labeled with fluorescent phalloidin. We first demonstrated that if the number of fluorophores is large enough, photobleaching occurs with the expected exponential time course. We reasoned that ~100-500 fluorophores in a half-sarcomere would be needed to ensure smooth decay of fluorescence. The typical height, width and length of a sarcomere are 0.1 μm , 0.8 μm and 2.5 μm , (65) respectively, so its volume is $0.2 \mu\text{m}^3 = 0.2 \times 10^{-15} \text{ L}$. Since the concentration of actin in muscle is 0.6 mM, (7) this volume contains 0.7×10^5 actin monomers. Therefore to ensure that ~1 in 10^2 molecules are labeled, we have to label with 100 nM RP (+9.9 μM non fluorescent label), i.e. fix the ratio of fluorescent to non fluorescent phalloidin as 1:100. The top panel of Fig. 11 shows the time course of photobleaching of the myofibrils labeled with 100 nM RP + 9.9 μM UP. The images were captured every 200 ms; only the first, 10th, 50th, 100th, 200th, 300th and 500th frames are shown. The time course of photobleaching of the O-band (spot number 29 in the entire image) pointed to by the arrow in the top panel is plotted in gray in the left bottom panel of Fig. 11. Photobleaching of the adjacent background area (spot number 19) of the same size (4×4 pixels) pointed to by the arrowhead in the top panel is plotted in black. This signal probably originates from fluorophores that are washed out from the muscle and become stuck to the coverslip. The difference between the two is plotted in the right bottom panel. As expected, the time course of

photobleaching is smooth. The fit to the three parameter exponential (shown in white) $y = 2806 + 11577e^{-4.4 \times 10^{-3}t}$ is good. The halftime is ~ 40 s.

Single Molecule Measurements

On the basis of this experiment, we estimate that in order to see individual molecules we need a 1000-fold smaller concentration of phalloidin. The top panel of Fig. 12 shows the time course of photobleaching of contracting myofibril labeled with 0.1 nM RP + 10 μ M UP. Only the first, 10th, 50th, 100th, 200th, 300th, 400th and 500th frames are shown. The time course of photobleaching of the O-band pointed to by the arrow in the top panel is plotted in the left middle panel (gray). The time course of photobleaching of the 4 \times 4 pixel background immediately adjacent to the analyzed O-band, pointed to by the arrowhead in the top panel, is plotted in black. The time course of photobleaching of the difference between the intensity of the O-band and adjacent background is plotted in the right middle panel of Fig. 12. In this case we observed 3 molecules, because photobleaching occurred in three steps. The stepwise decrease in signal is visible even though the 3 fluorophores are most likely localized at different distances from the surface of the coverslip, and therefore bleach with different efficiencies.

Fluctuations in orientation of actin in the O-band are greater before than after photobleaching step. The power in the first 20 s part of the signal (before photobleaching) is shown in the bottom panel of Fig. 12 in black. The power in the last 20 s part of the signal (after photobleaching) is shown in the bottom panel of Fig. 12 in gray. On numerous occasions, there was only a single fluorophore in the O-band. A typical example is shown in Fig. 13. The top panel shows the time course of photobleaching of contracting myofibrils labeled with 0.1 nM RP + 10 μ M UP. The time course of photobleaching of the O-band pointed to by the arrow in the top

panel is plotted in the left middle panel (gray). The time course of photobleaching of the 4×4 pixel background pointed to by the arrowhead in the top panel is plotted in black. The time course of photobleaching of the difference between the intensity of the O-band and adjacent background is plotted in the right middle panel of Fig. 13 (black). The bottom panel shows the 24 s of head and tail parts of the signal on the expanded time scale (left) and the corresponding power spectra (right).

To analyze fluctuations statistically, the amount of power in the signal before and after the photobleaching event was compared. The signal was divided into two parts: the head part consisting of the signal collected during the beginning of the experiment before the first photobleaching event (containing useful signal + random noise and lasting typically 20-40 s), and the tail part consisting of the signal collected after the second photobleaching step (containing random noise and lasting $\sim 20-40$ s). Fig. 14 compared the power before and after the photobleaching event in 19 experiments where oscillations were pronounced. In all cases, the peak frequencies of intensity changes were < 0.2 Hz. The mean frequency was defined as $\Sigma fN / \Sigma N$, where f is a given frequency and N is the number of measurements at this frequency (ΣN is the total number of measurements). The mean frequency was 0.17 Hz, giving mean $t_c \approx 6$ s.

In an attempt to determine t_s , we analyzed in detail 48 experiments as illustrated in Fig. 15. The theoretical upper and lower limits were set by the bounds of variation due to random noise $N \pm \sqrt{N}$ (mean \pm square root of mean). These are drawn as gray lines. It is clear that these limits were rarely exceeded for the background noise (bottom trace). In contracting muscle, on the other hand, the limits were often exceeded (top trace). Actin was judged to contain bound cross bridge when this limit was exceeded by at least 100%. The arrows indicate full width at half-height (fwhh) of the impulses which satisfied this condition. The histogram of duration of

the impulses is plotted in Fig. 16. The mean duration, defined as $\Sigma t_s N / \Sigma N$, where t_s is a given duration and N is the number of measurements with this duration (ΣN is the total number of measurements). The mean duration was 3.4 s.

Discrete photobleaching occurred even though the fluorophores were bleaching with different efficiencies. In spite of this, it was possible to estimate the average duration of a step as ~ 20 s. Each step led to the decrease of gray level by ~ 4000 . The number of photons corresponding to this gray value was measured by taking advantage of our ability to direct the signal either to the EM CCD camera or to the Avalanche Photodiode. We determined that the gray value drop of 4000 corresponds to a loss of ~ 800 photons/s. In 20s we therefore observed $\sim 16,000$ photons from a fluorophore before it photobleached. The geometrical collection efficiency of the instrument is $\sim 2\%$, (19), thus a fluorophore emitted a total of 0.8×10^6 photons before irreversible bleaching. This is consistent with known photostability of rhodamine.

Control Experiments

We considered three possible reasons why phalloidin labeling could lead to spurious signal generation. We found them impossible or unlikely: (i) *The signal is not originating from 0.1 nM RP, but from higher concentration of dye because the ON-rate of RP binding is faster than the ON-rate of UP binding.* This is conceivable, in spite of the fact that fluorescent phalloidin is bulkier because it contains an additional rhodamine molecule. The consequence would be that the molar ratio of labeled to unlabeled phalloidin was larger than claimed. The following experiment convinced us that this was unlikely: we labeled myofibrils with a fixed molar ratio RP:UP of 10^3 and increased by the same factor the absolute concentration of both RP and UP (we used 10 nM, 100 nM and 1 μ M of RP and 10 μ M, 100 μ M and 1 mM of UP). If RP

bound faster than UP, more actins would get labeled when higher absolute concentrations were used, and the image would become progressively better. This was not the case. In fact, the image became progressively worse, suggesting that UP binds faster than RP.

(ii) The signal is not originating from 0.1 nM RP, but from higher concentration of the dye because the OFF-rate of UP is sufficiently fast for RP to displace it from thin filaments. As a consequence, the molar ratio of labeled to unlabeled phalloidin is larger than claimed 1:10⁵. However, this is unlikely because in a control experiment we first labeled 1 mg/mL (4 μM actin) myofibrils with an excess of UP. After brief incubation, we added 4 μM RP in an attempt to displace bound UP with RP. If the OFF-rate of UP were faster than RP, myofibril would have now become fluorescent. This was not the case, suggesting that the OFF-rate of UP is slow. This is consistent with the fact that the dissociation of phalloidin from actin is known to be slow ($4.8 \times 10^{-4} \text{ s}^{-1}$, i.e. phalloidin spends on the average 2,000s on actin before dissociating. (iii) Fluorescence is due to fluorescent contaminant in unlabeled phalloidin. This is impossible, because in a control experiment we saturated the myofibrils with 0.6 mM UP and observed no fluorescence whatever.

FIGURES

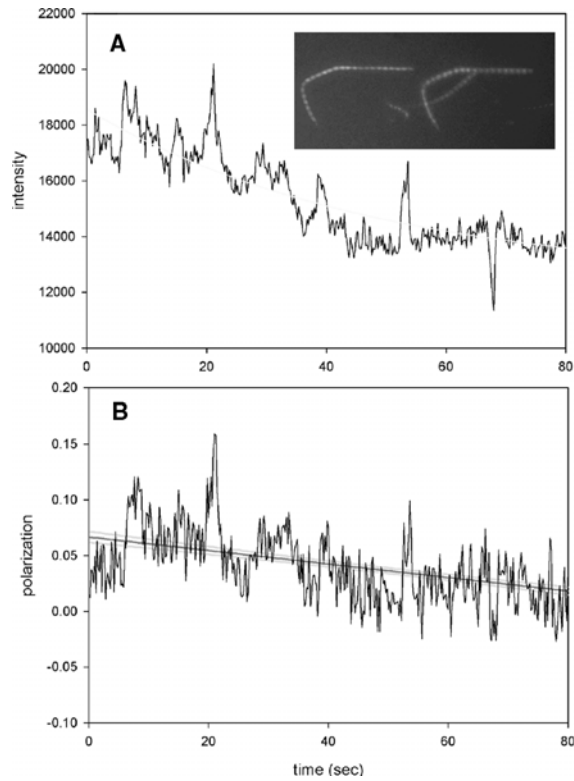
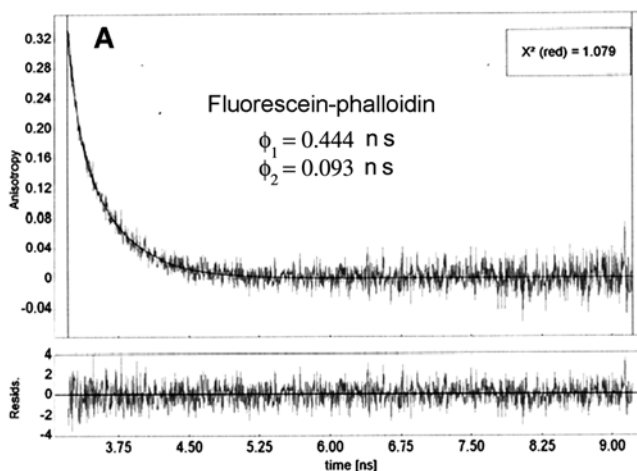
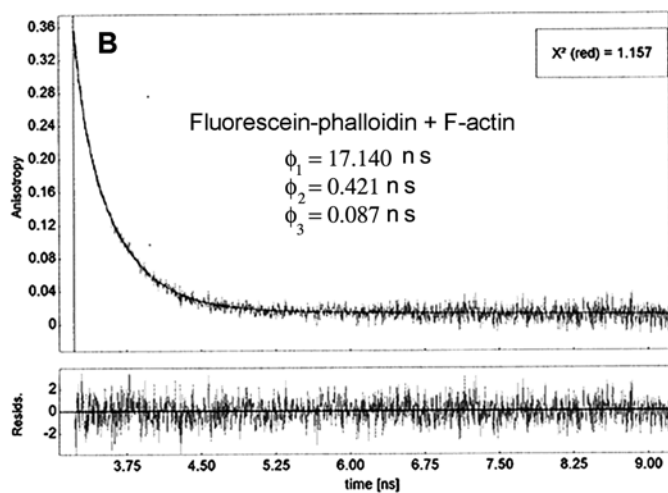


Fig 9: Comparison of polarized intensities and polarization of fluorescence. (A) Horizontal polarized intensity. Inset shows the two orthogonally polarized images: left, emitted light polarized parallel to the myofibrillar axis; right, emitted light polarized perpendicular to the myofibrillar axis. Exciting light polarized horizontally. White line is 3 parameter exponential function showing poor fit to the data. (B) Polarization of fluorescence. Myofibril labeled with 1 nM RP + 10 μ M UP. Thick line is the best linear fit; gray lines indicate 95% confidence limit.

Main Plot



Main Plot



$$r(t) = R_{INF} + \sum_{i=1}^n R_i e^{-t/\tau_i}$$

$$r_{Exp.}(t) = \frac{I_1(t) - G I_2(t)}{I_1(t) + 2 G I_2(t)}$$

Fig 10: Decay of anisotropy of fluorescein phalloidin (A) and fluorescein phalloidin bound to F-actin (B). Binding of phalloidin to F-actin results in a significant immobilization of the probe. (A) 0.1 μ M fluorescein phalloidin, (B) 2 μ M F-actin containing 0.5 μ M fluorescein phalloidin. The equation shows the model to which anisotropy was fitted. R_{INF} was fixed at 0.

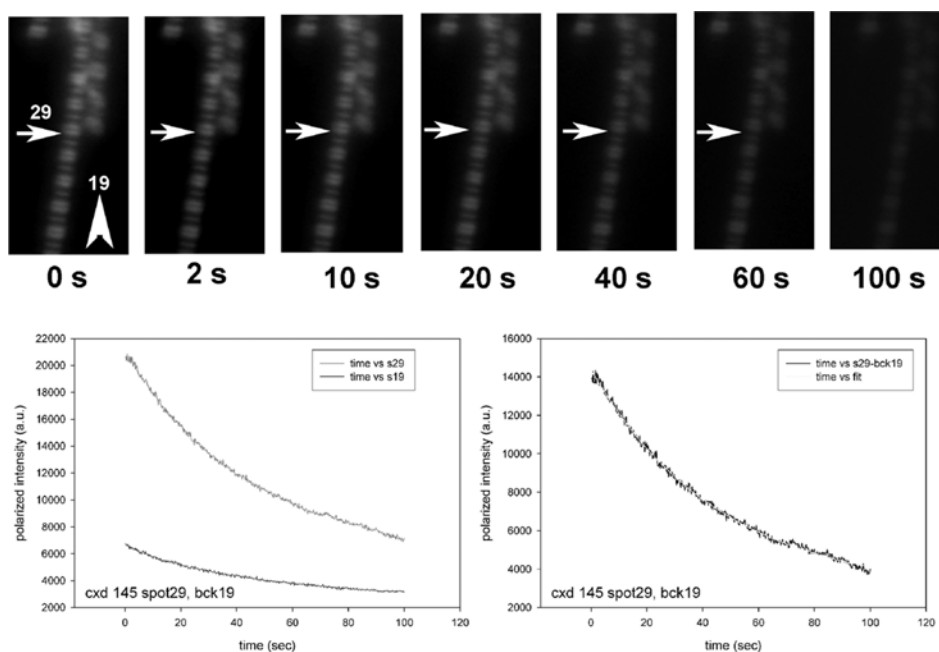


Fig 11: The time course of photobleaching of heavily labeled rigor myofibril. Top panel: Polarized images of a myofibril at times indicated below each frame ($s = 1$ s). Exciting light is polarized vertically, emitted light polarized horizontally with respect to the myofibrillar axis. Bottom left panel: The time course of photobleaching of the O-band pointed to by the arrow in the top panel (gray). The time course of photobleaching of 4×4 pixel background pointed to by the arrowhead in the top panel (black). Bottom right panel: The time course after background subtraction. The least-squares 3-parameter exponential fit (white) is $y = 2806 + 11577e^{-4.4 \times 10^{-3}t}$. Myofibril is labeled with 100 nM RP + 9.9 μ M UP. Myofibrils are on sapphire coverslip, viewed by 100X. NA = 1.65 objective.

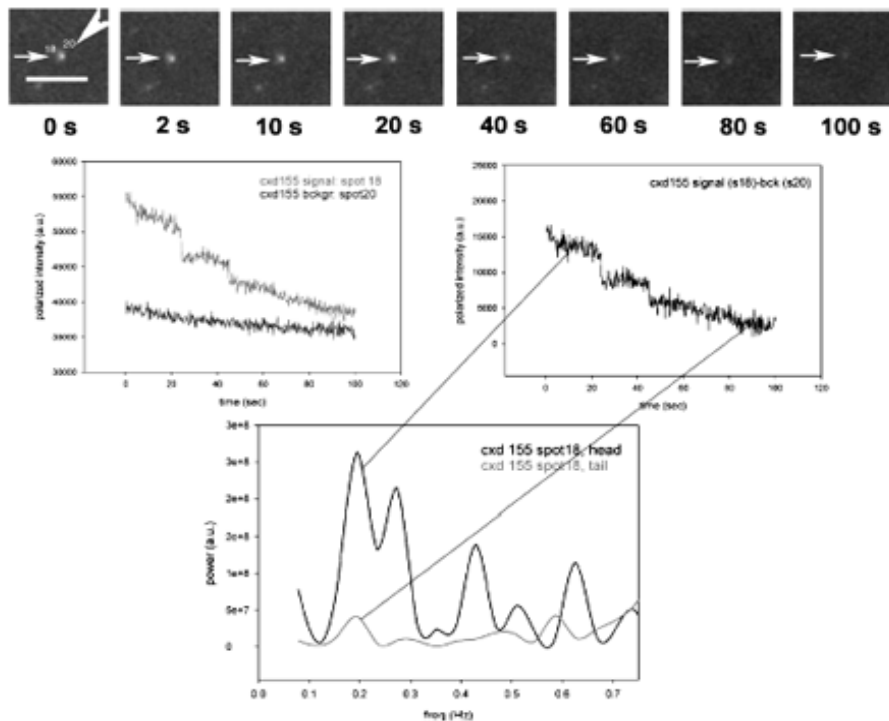


Fig 12: The time course of photobleaching of contracting myofibril: 3 fluorophores. Top panels: myofibril at times indicated below each frame ($s = 1$ s). Exciting light is polarized vertically, emitted light polarized horizontally with respect to the myofibrillar axis. The arrows point to the analyzed O-band. The arrowhead points to the 4×4 background pixels. Numbers indicate spot number of the image. The bar is $10 \mu\text{m}$. The O-band is $\sim 0.9 \mu\text{m}$ wide. Middle panel: The time course of photobleaching of the O-band pointed to by the arrow in the top panel. Left: Raw signals from the O-band (gray) and background (black). Bottom panel: Power spectra of the first 20 s (black) and the last 20 s (gray) of the polarized intensity. Myofibril on sapphire coverslip, labeled with $0.1 \text{ nM RP} + 10 \mu\text{M UP}$; viewed with 100X, 1.65 NA objective using 1.78 refractive index immersion liquid.

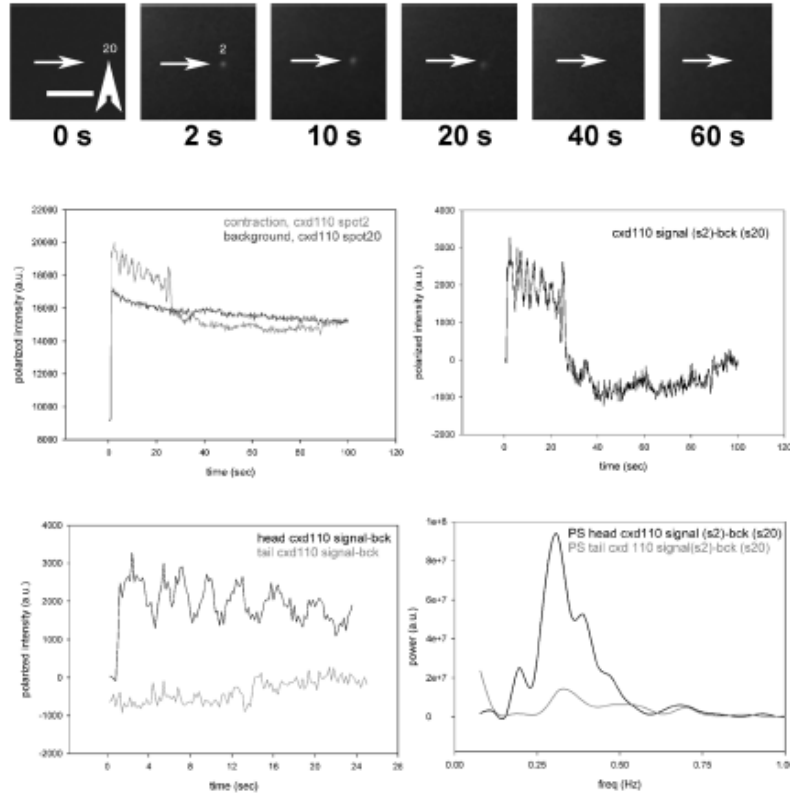


Fig 13: The time course of photobleaching of contracting myofibril: single fluorophore. Top panels: Images of contracting O-band. Numbers below each frame indicate the time ($t = 1$ s) after opening the shutter admitting the laser beam. Exciting light is polarized vertically, emitted light polarized vertically with respect to the myofibrillar axis. The bar in the first panel is $10 \mu\text{m}$. The O-bandwidth is $\sim 0.8 \mu\text{m}$. Arrows point to the O-band analyzed in the bottom panel. Arrowhead points to the background ROI (4×4 pixels). Middle panel: The time course of intensity change of the O-band pointed to by the arrow in the top panel. Gray: absolute intensity. Black: Background pointed to by the arrowhead above. Black in the right panel: the signal-background. Left bottom panel: 24 s of the head (black) and tail (gray) of the signal. Right bottom panel: Power spectra of the head (black) and tail (gray) part of the signal. Myofibrils are labeled with $0.1 \text{ nM RP} + 10 \mu\text{M UP}$.

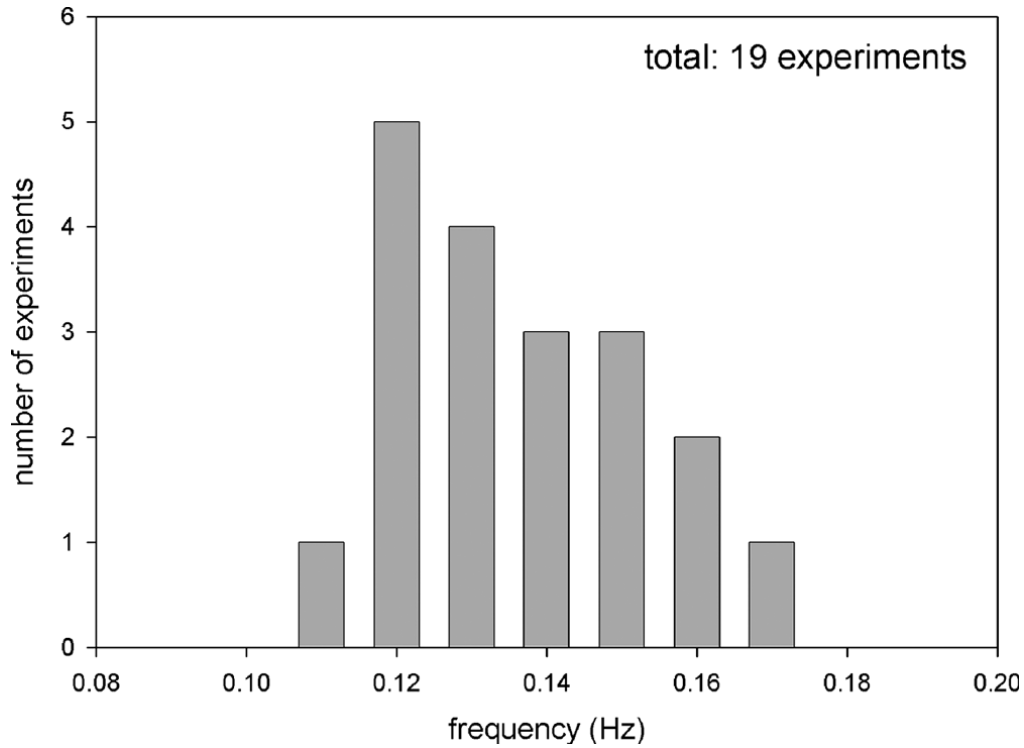


Fig 14: Histogram of the peak frequencies of the first 40 s of signals of contracting muscle. The mean frequency is defined as $\Sigma fN/\Sigma N$, where f is a given frequency and N is the number of measurements at this frequency. The total number of measurements was 19. The mean frequency was 0.14 ± 0.017 Hz. Analysis does not include experiments in which bleaching occurred in one step. Including these experiments, the average frequency was 0.14 Hz.

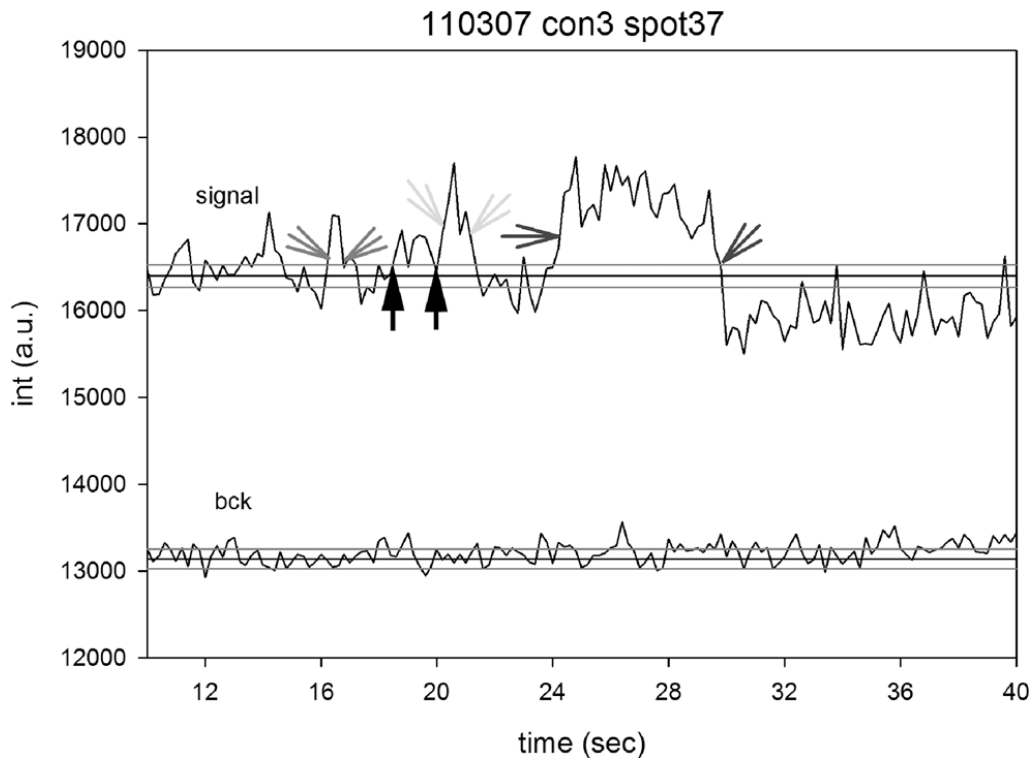


Fig 15: Polarized intensity of actin is high when the cross-bridge binds to actin, and low when it detaches from it. The duration of the actin in high state is defined as full width at half-height (fwhh) of the force impulses (indicated by arrows). Top trace: Contracting muscle. Bottom trace: The background. Gray lines indicate the limits of random variation of the noise. Some impulses, such as the one pointed to by the black arrows, were not included in the analysis.

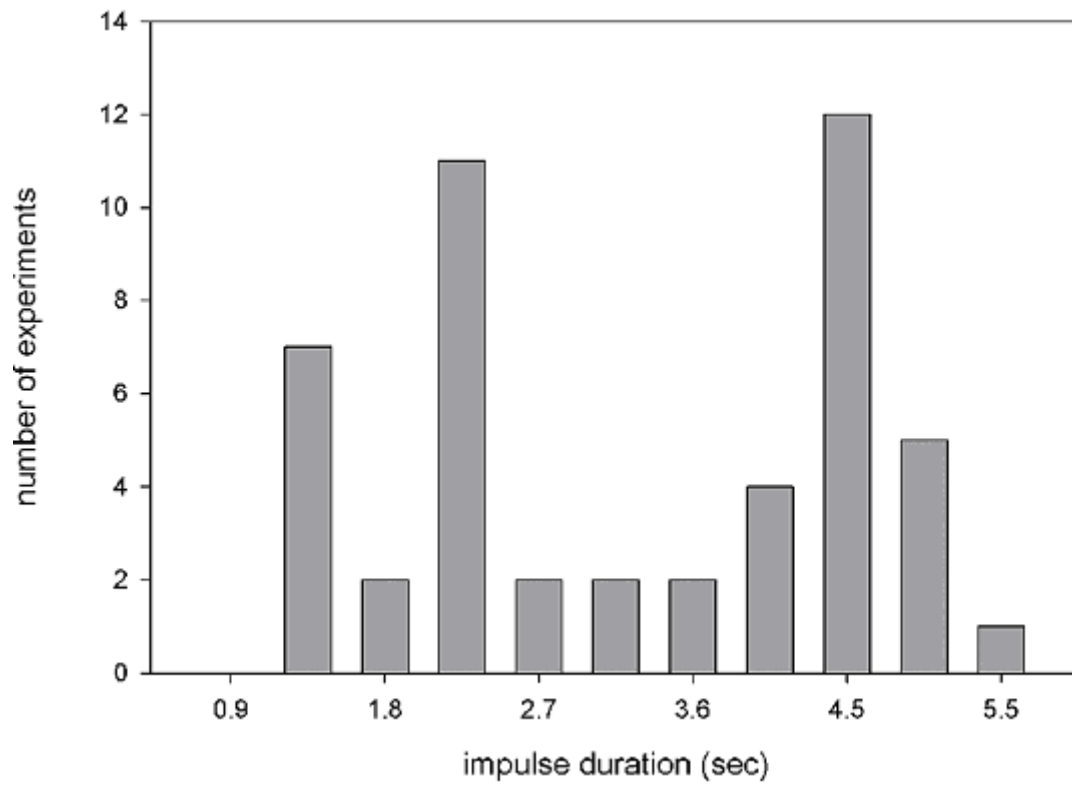


Fig 16: The histogram of the times anisotropy of actin was high. The mean duration is defined as $\Sigma t_s N / \Sigma N$, where t_s is a given duration and N is the number of measurements with this duration. The total number of experiments was 49. The mean duration was 3.4 s.

Discussion

Stepwise Photobleaching

Observation of individual molecules in muscle is complicated by the fact that the concentration of contractile protein is large (7) (1 cm long skeletal muscle fiber contains $\sim 10^{13}$ cross-bridges). Even if this number is reduced to a few hundred by the use of confocal (14) or two-photon microscopy (15), the averaging makes it impossible to distinguish individual impulses. Recent developments in confocal total internal reflection microscopy (CTIR) allowed observation of actomyosin interactions in a volume small enough to contain only a few molecules (20). Muscle was observed on metallic surfaces or on glass (19, 29). However, those were indirect measurements that relied on autocorrelation of APD signals. Here we demonstrated cross-bridge cycle by directly observing orientational state of actin.

A significant advantage of the present method is that it probes molecules in muscle. It is possible that cross-bridges in functioning muscle behave differently than in solution due to molecular crowding (67) and the organization of actin and myosin into regular arrays imposes restrictions on a cross bridge depending on its position relative to the actin “target site” (37).

Measuring t_s (dwell time)

The observed change of actin orientation was similar to the one predicted by the simple model where a cross-bridge is either bound to actin filament or dissociated from it. The average duration of high anisotropy of actin was 3.4 s. We attempted to see if t_s increases with concentration of ATP, like it does in in vitro experiments (8). We carried out 13 experiments using 10 μ M ATP to stimulate contraction. The analysis of t_s did not yield consistent results. However, we could estimate t_c rather accurately. The average frequency during the first 20 s was

0.095 ± 0.015 Hz. The average frequency during the first 20 s using 2 mM ATP was 0.14 ± 0.017 . The difference between two means is statistically significant ($t=5.14, P = 2.4 \times 10^{-4}$).

Measuring t_c

It is believed that splitting of one molecule of ATP leads to a single impulse (88). In vitro evidence, based on observation of the individual steps of smooth myosin, myosin V (74, 92), myosin VI (41, 86, 100) and kinesin (86, 100, 101) suggests that it is indeed so under unloaded conditions. But this does not necessarily have to be so in isometrically working muscle where a significant external load is applied to cross-bridges and where no gross mechanical work is performed (96). Here, splitting of one ATP molecule could lead to multiple mechanical cycles (98). Conversely, the energy of hydrolysis could be used for purposes other than performance of mechanical work. Our results suggest that this is indeed the case, because the observed average rate of change of actin orientation was 0.14 Hz, much smaller than myofibrillar ATPase activity. The ATPase activity of our un-cross-linked myofibrils was 89 μmol of Pi/ μmol of myosin/min = 1.5 Hz (labeling with phalloidin or cross-linking did not change ATPase: it was within experimental error of this value). The present results support the idea that the observed rotation of cross-bridges is a result of “slippage”, i.e. that cross-bridges that rotate do so only because they are not rigidly held in place. If the conditions were ideally isometric, no rotation would have occurred at all and all the energy of hydrolysis would have been used for maintenance or wasted as heat.

Duty Ratio

The ratio $DC = t_s/t_c$ in isometric contraction was therefore nearly 60%, much larger than measured *in vitro* (57, 92). Under isometric conditions, a cross-bridge acts against maximum load

(equal to isometric force), whereas under isotonic conditions it acts initially against a small load. The load increases in time as the muscle is stretched. This is consistent with the fact that isometric force and quick tension recovery seemed to result from two distinctly different molecular processes. Isometric force resulted from a structural change in the actomyosin complex associated with the transition from a weakly bound configuration to a strongly bound configuration (before the reaction steps in the Huxley-Simmons model), whereas a major component of quick tension recovery originated from transitions among the subsequent strongly bound states (26). It is also consistent with the fact that the tension fluctuations were present only in isometrically held actin filaments (98), that the sliding distance of the myosin head while it interacts with actin per ATP molecule hydrolyzed decreased with load (48), that increasing the stiffness of the optical trap holding actin filament led to shorter duration of actomyosin attachment events (82), and that step size may be zero in isometric muscle.

We considered eight possible artifacts that may have given rise to this observation, and concluded that none are likely:

1. *The oscillations are an artifact resulting from spurious sources* such as EM CCD readout noise, other instrumental noise, laser instability, air currents on the microscope stage or building vibrations. It is also possible that faster oscillations are missed because the time resolution of the method is too slow to observe fast motions. This is unlikely, because rigor myofibrils, imaged under identical conditions, showed no oscillations. Time resolution is sufficient; because one frame was collected in 200 ms giving frequency resolution of 5 Hz. Oscillations would have to be much faster than ATPase for the present method to miss them.
2. *The oscillations are an artifact resulting from gradients of ATP concentration.* This is unlikely, because ours were steady-state experiments, i.e. contraction was initiated by

addition of ATP. ATP was added to one side of the experimental chamber, and sucked with a filter paper at the other end. The few minutes necessary to focus was plenty of time to equilibrate the ATP concentration across the chamber. This is the advantage of steady-state experiments, which avoid production of the gradients which could be generated when imposing rapid increase in ATP concentration by rapid photolysis of caged ATP (23).

3. *The oscillations are an artifact resulting from photobleaching.* This may not have been the case, because the fast Fourier transform was applied either before or after the photobleaching event.
4. The oscillations are an artifact due to movement of myofibrils. It is unlikely that oscillations were due to the change in the number of fluorophores in the 4×4 pixel observational area due to shortening of myofibrils. We would have been able to detect shortening of $0.2 \mu\text{m}$ (limit of resolution) in 100 s, i.e. 2 nm/s. No such shortening occurred in cross-linked myofibrils. But even if it did occur, its frequency would have been negligible: the observational area is 4×4 pixels. The back-projected size of a pixel is $16 \mu\text{m}/100 = 160 \text{ nm}$, i.e. linear dimension of ROI is 640 nm. It would take, on average, $\sim 160 \text{ s}$ for a single fluorophore to leave this area to give rise to a fluctuation in intensity. Its frequency would have been 0.0006 Hz. When 3 fluorophores were observed, their escape from the area would lead to signal oscillating at 0.02 Hz, much below what was observed. It is also unlikely that oscillations were due to the change in the number of fluorophores in the observational area due to oscillatory motion of myofibrils. Ishiwata et al. found that the myosin II motors show nonlinear auto-oscillation, named SPOC (spontaneous oscillatory contraction). For cardiac muscle it occurred when the activation level was intermediate between those of contraction and relaxation. For skeletal muscle, it required the coexistence of MgATP, MgADP and

inorganic phosphate (Pi) at higher pCa (<7) (55). In our experiments, however, pCa was fixed at four.

5. Fluorescence oscillations are an artifact resulting from dissociation of phalloidin from thin filaments. The OFF-rate of UP is slow (see above and ref 43), but the OFF-rate of RP could, in principle, be faster. Its dissociation-association from actin could have been responsible for oscillations. However, this is unlikely, first because rigor myofibrils did not show any oscillations and second, because if this were the case, it would have been possible to wash out the fluorescent dye with prolonged washing. This has proven impossible: 15 min washing of myofibrils labeled with 1 nM RP + 10 μ M UP did not reduce fluorescence at all (in fact, it improved the contrast, probably because the background was reduced). Further, independent measurements of fluorescence correlation spectroscopy (FCS) of contracting myofibrils showed no translational motion of free phalloidin (data not shown).
6. The signal is not reflecting rhodamine concentration, but originates from Trp fluorescence of myofibrils. Even though Trp has practically no absorption at 532 nm, the concentration of RP (0.1 nM) is so much smaller than the concentration of protein (4 μ M) that the signal carries a significant contribution from auto fluorescence. However, this is unlikely, because unlabeled myofibrils had no auto fluorescence whatsoever, probably because the sample was only ~100 nm thick.
7. The signal is due to rotation of the edges of the O-bands of contracting muscle because the end of thin filaments may be fluttered or undergo tethered motion sometimes. Such motion does not occur in rigor because the end of thin filament are rigidly fixed by the binding of rigor cross bridges. This has been checked by FCS. In 9 independent measurements on ~10

molecules in an area near the edge of the I-band, the autocorrelation function was the same in rigor and in contracting myofibrils.

It is unlikely that our observations are due to the fact that the observed actin monomer is too far away from the nearest active cross-bridge to be touched by it. The molar ratio of actin:cross-bridges is ~2:1. In isometric contraction only ~1/3 of cross-bridges are active, so the excess of actin over active heads is about 6. This ratio implies that in ~15% of experiments we can expect to observe a monomer that is near the active cross-bridge. Such actin would be expected to rotate at the ATPase frequency. However, high frequencies were never observed in the total of 19 analyzed experiments. They were also never seen by visual inspection of many more unanalyzed experiments.

8. In relaxed muscle, cross-bridge cycling should stop. We have done 72 experiments on 4 different preparations of myofibrils in rigor, 72 experiments on 4 different preparations in relaxation, and 40 experiments on 4 different preparations during contraction. Myofibrils were labeled with 1 nM RP + 10 μ M UP and cross-linked as described to avoid shortening. Sarcomere lengths ranged from 1.73 μ m to 2.88 μ m. No shortening occurred within 100 s. Rigor myofibrils gave no fluctuations at all. In 56 experiments on relaxed myofibrils we observed no fluctuations at all. In 16 experiments on relaxed myofibrils we observed some fluctuations.

We think that this was due to the fact that some sarcomeres in those 16 myofibrils were not sensitive to Ca^{2+} . If a few troponin or tropomyosin molecules are damaged, than this sarcomere is going to contract even if there is EGTA in bathing solution. All 40 experiments on contracting myofibrils showed fluctuations. In all 40 experiments, the power during the last 20 s was on average 1.7 times smaller than during the first 20 s.

Our investigation showed that actin monomers rotate during isometric contraction of myofibrils and that in isometrically working muscle cross bridges spend about half of cycle time attached to actin. The bulk of the energy of ATP hydrolysis may be used for purposes other than performance of mechanical work.

CHAPTER V

SPECIFIC AIM 2

Specific Aim 2: Study the molecular mechanisms involved in contraction in cardiac muscle carrying the D166V mutation in myosin RLC.

Rationale:

FHC is an autosomal dominant disease originating from mutations in genes that encode for the major contractile proteins of the heart, including the ventricular myosin regulatory light chain (RLC) and myosin essential light chain (ELC). It has been proposed that FHC might be caused by an inefficient utilization of ATP by cardiac muscle due to mutation-mediated alteration of the kinetics of myosin cross-bridges (5, 77, 78). This specific aim will test this hypothesis by examining the kinetics of single actin and myosin molecules which carry the disease-causing mutation, D166V, in the regulatory light chain of myosin. Clinical studies have revealed that the D166V mutation in myosin RLC is associated with a malignant FHC disease phenotype. Being hydrophobic and C- β branched, valine may introduce more bulkiness near the protein backbone and put restrictions in the conformations that the main chain can adopt. Perhaps the negative charge of the aspartic acid is necessary for the elbow of the myosin lever arm to efficiently execute its swinging motion, enabling the power stroke, and replacement of this residue with a bulky valine prevents the efficient interaction of myosin with actin. We hypothesize that the D166V mutation of RLC leads to alterations in myosin cross-bridge kinetics, thus affecting the interaction of the thick and thin filaments during cardiac muscle contraction. We will monitor the cross bridge to study the kinetics in transgenic heart muscle,

where complications associated with the study of reconstituted tissue or isolated proteins will be avoided.

Introduction

Despite significant clinical advances in the treatment of various cardiovascular diseases, mortality rates remain high. No therapy currently exists to treat or delay progression from cardiac hypertrophy to heart failure. Familial hypertrophic cardiomyopathy (FHC) is one such pathological manifestation of the heart resulting from its inability to adequately pump blood, thus leading to premature fatigue, dyspnea, hypertrophy and/or cardiac failure. It is an autosomal dominant disease originating from mutations in genes that encode for the major contractile proteins of the heart, including the ventricular myosin regulatory light chain (RLC). It is characterized by ventricular and septal hypertrophy, myofibrillar disarray, abnormal ECG findings and frequent sudden cardiac death (SCD) at a young age. Clinical studies have revealed that the D166V mutation in myosin RLC is associated with a malignant FHC disease phenotype. Our objective is to examine the molecular determinants of the D166V induced malfunction of the heart.

Analysis of the crystal structures, X-ray diffraction patterns and spectroscopic experiments confirmed the original idea of Huxley that during isometric muscle contraction the myosin cross-bridges assume at least two distinct conformations, when they are strongly attached to- and dissociated from- thin filaments (54). It is believed that strongly attached cross-bridges produce contractile force (97). The environment of a strongly attached cross-bridge is different from the environment of a dissociated cross-bridge. In this aim, we study the strongly attached as well as the detached state of the cross bridge in an attempt to understand the disease.

Muscle contraction results from the cyclical interactions of actin and myosin. During this interaction myosin cross-bridge delivers force impulses to actin. Isometric force is the time average of those impulses. In the scheme originated by Huxley, a cross-bridge is either attached or detached from actin. The impulse begins when dissociated cross-bridge, containing products of hydrolysis of ATP, attaches to actin. It is believed that a cross-bridge is strongly bound to actin for a period of time t_{ON} (ON-time) during which it generates contractile force. The binding and force generation is followed by a release of phosphate, the dissociation of ADP and the onset of rigor state. In rigor state a cross-bridge assumes a well defined orientation. The end of an impulse is marked by the binding of a fresh molecule of ATP and dissociation of myosin from actin. Cross-bridge remains detached from actin for a period of time t_{OFF} (OFF-time) during which it is idle and disordered. Finally, ATP is hydrolyzed to ADP and phosphate, and the cycle repeats with the period $t_{ON}+t_{OFF}$. The fraction of a total cycle time that a cross-bridge remains attached to actin $\Psi = t_{ON} / (t_{ON}+t_{OFF})$ is known as the duty cycle. Huxley & Simmons suggested that a cross-bridge can attach to thin filament in a variety of conformations and that generation of force involves transition between these conformations.

Macroscopic measurements cannot provide information about cross-bridge kinetics because they ignore stochastic variations in the signal, which contain information about kinetic of individual events. They report an average of all impulses. Unless each impulse is the same, there is no way to extract information about the individual event from the average. In muscle, each contractile event is different, because its kinetics depends on the relative position of actin and myosin. This position is not constant, even during isometric contraction because of internal elasticity of a sarcomere. However, the extent of averaging is inversely related to the number of molecules under observation. Therefore, when only a single cross bridge is observed, the ON–

OFF times of a single molecule can be readily deconvolved from the signal. This is so called “mesoscopic regime” – the regime when only a few molecules contribute to the signal and stochastic fluctuations of a signal, in contrast to macroscopic measurements, become important.

In this specific aim, we chose to observe actin rather than myosin, because observing actin has five essential advantages. First, labeling actin with phalloidin preserves the regular structure of a myofibril, unlike the less gentle labeling of myosin. Second, phalloidin does not alter enzymatic properties of muscle. Third, it labels actin specifically and stoichiometrically, which allows strict control of the degree of labeling. Fourth, non-covalently but strongly attached phalloidin attaches to actin more rigidly than covalent probes. Finally, labeling actin with phalloidin allows observing events that occur only in the area where actin and cross-bridges interact. Observing actin is a valid way of observing effect of cross-bridges, because it has been known for a long time that actin changes orientation in response to cross-bridge binding. Those changes parallel changes of orientation of a cross-bridge.

RESULTS

Preventing shortening of contracting muscle

Our task was to compare the cross bridge kinetics between cross bridges in Tg-WT and Tg-D166V myofibrils during rigor and contraction. There is no difficulty in measuring the kinetics in rigor myofibrils. However, it is impossible to do so during contraction, because myofibrils shorten. To measure the lifetime of a contracting muscle, it is necessary to prevent myofibrils from shortening. This was done by cross-linking with the water-soluble cross-linker EDC. Cross-linking does not affect force development. Myofibrils were cross-linked for 20

minute room temperature with 2 mM EDC. The lack of shortening was checked by following the changes in the image in a microscope as described in. Fig 1.

Imaging

A typical lifetime image of a rigor myofibril irrigated with 0.1 nM RP + 10 μ M UP is shown in Fig. 2. The various bands are best identified with the aid of image of myofibrils more heavily labeled with phalloidin. This image clearly shows that there are two bright overlap bands (O-bands) in a center of each sarcomere (i.e. fluorescence does not originate from the I-bands) and that each is separated by a dark I-band.

Number of fluorophores/photon rate per fluorophore

Data is collected from a circular area (Detection Area, DA) by the microscope. The diameter of this area is equal to the resolution of the microscope ($\sim 0.3 \mu\text{m}$, $\text{NA}=1.2$, $\lambda_{\text{exc}}=470 \text{ nm}$). The question arises how many fluorophores are in this area when a myofibril is labeled with 0.01 nM RP+10 μ M UP? The theoretical estimation, based on the predicted number of actin molecules in a half sarcomere, leads to a nonsensical answer. We have therefore estimated this number experimentally: The visual inspection of the lightly labeled myofibril showed that there are 58 ± 10 molecules in the O-band. The area of the O-band is $\sim 1 \mu\text{m}^2$. This is 14 times greater than the DA, suggesting that we detect fluorescence from ~ 4 molecules. To decrease this number further, the shutter admitting the laser beam was left open for a few minutes in order to photobleach some molecules. The number of remaining ones is best estimated by monitoring photobleaching of fluorescence from the detection area. The intensity suddenly dropped at $\sim 35 \text{ s}$

to a level characteristic of the background – a distinguishing feature of single molecule detection. This was the case for most spots in the myofibril.

Measurement of duty cycle

As illustrated above, it is possible to measure one or two fluorophores i.e: one or two cross bridges when the myofibril is labeled with 0.01nM RP + 10 μ M UP. We then attempted to study the cross bridge kinetics in both Tg-WT and D166V muscle. In an attempt to determine t_s , we studied the contracting and rigor WT and D166V muscle using TIRFM attached to a Hamamatsu ImageEM CCD camera. We analyzed in detail 48 experiments as illustrated in Fig. 3. The theoretical upper and lower limits were set by the bounds of variation due to random noise $N \pm \sqrt{N}$ (mean \pm square root of mean). These are drawn as red lines and black lines respectively. It is clear that these limits were rarely exceeded for the background noise (bottom trace). In contracting muscle, on the other hand, the limits were often exceeded (top trace). Actin was judged to contain bound cross bridge when this limit was exceeded by at least 100%. The arrows indicate full width at half-height (fwhh) of the impulses which satisfied this condition. The histograms of duration of the ON and OFF states in 17 experiments on Tg-WT muscle is plotted in Fig 4. The average duration of the high intensity, corresponding to the ON time of the cross-bridge was $t_s = 2.0$ sec (left panel). The average duration of the cycle was $t_c = 2.6$ sec (right panel). The fraction of time the cross-bridge is attached to actin during isometric contraction of cardiac transgenic papillary WT myofibrils was therefore $t_s/t_c = 0.76$. The rotation of cross-bridges from mutated (D166V) transgenic papillary muscle was measured. Fig 5 illustrates the time course of a change of actin orientation in Tg-D166V myofibrils. As expected, the cross bridge spent a longer time attached to actin as observed by the longer ON and OFF times. The

histograms of these durations in 19 different experiments have been plotted in Fig. 6. The average duration of the high intensity, corresponding to the ON time of the cross-bridge was $t_s=4.0$ sec (left panel). The average duration of the cycle was $t_c=6.2$ sec (right panel). These results have been summarized below:

Table 1: Rate of duty cycle in transgenic WT and D166V muscle fibers:

Muscle	Tg-WT	Tg-D166V
t_s (sec)	2.0 ± 0.35	4.0 ± 2.06
t_c (sec)	2.6 ± 0.54	6.2 ± 3.51
Ψ	0.76	0.64

Because the error in measurements of Tg-D166V is large (SD $\sim 50\%$ of the mean), the Micro Time 200 (PicoQuant GmbH, Berlin, Germany) and ISS-Alba-FCS (ISS Co, Urbana, IL) confocal systems were used to confirm these results.

Fig. 7 shows a typical signal of contracting muscle. The perpendicular (I_{\perp}) and parallel (I_{\parallel}) intensities (to the axis of the myofibril) are shown in the red and blue, respectively. The data output is very similar for WT muscle. Although photobleaching experiment with lightly labeled myofibrils fixed the average number of observed molecules at 1-2, it is impossible to perform such experiment on the actual spot selected for experimentation, because no fluorescence is left after complete photobleaching. The number of detected molecules in each experiment was instead estimated from signal intensity. The average photon counts from rigor myofibrils, as well as averages from adjacent area were similar to the contracting muscle.

Autocorrelation of polarized fluorescence of contracting muscle

It is obvious by inspection that fluctuations are larger during contraction than during rigor (the data is quantified by comparing histograms of fluctuations in rigor and contraction). In principle, when the number of observed molecules is as small as two, it should be possible to distinguish individual impulses by inspection of the intensity trace. In practice, as seen in Fig 7, this was not possible. If we observed one molecule this perhaps would have been possible; as it is, the signal was too noisy. However, signal contributed by 2-4 molecules falls well within mesoscopic regime when stochastic fluctuations become important. A convenient way to extract contribution of individual molecules from stochastic variations is to compute correlation function of the fluctuations. Correlation function at a given delay time τ is a sum of the products of a signal multiplied by a signal shifted by a delay time τ . Thus if τ is small and there is any correlation between signal and its value at time τ later, the correlation function will be large. As the value of τ increases, however, the signal will drift from the original point so that it is of the opposite sign and the product will be negative. As a consequence, the correlation function will be small. If there is no correlation between signal and its value at time τ later, the correlation function will be zero. Thus the shape of correlation function reveals the shape of the underlying event.

To reveal periodic processes underlying polarized fluorescent signals of Fig. 7, the correlation function of the signals were computed. We used either one of the orthogonal polarized components because anisotropy signal was too noisy (it is a ratio of two noisy orthogonally polarized components). This is justified, because polarized components behave just like anisotropy. To compute the correlation functions, the signals were fitted to the exponential function, the exponential was subtracted from the data to get zero average value and correlation

function was computed. The correlation functions corresponding to the signals in Fig. 7 A & B are shown in Fig. 8A & B. There was a significant difference between the contraction profile in WT and D166V myofibrils (Fig.8C). In order to get correlations only between corresponding points, padded zeros have been added before the correlation calculation. 1000 points averaging was used. The two times were extracted from the correlation function: the first was from time 0 until the correlation function first changed slope (t_{ON}), and the second was the time from the changing of slope to the next maximum (t_{OFF}).

Histogram of changes of polarized intensity

Fig. 9 shows a typical histogram of polarization values during contraction (A) and rigor (B) in WT and D166V muscle fibers. The t_{ON} and t_{OFF} times were tabulated for all 45 independent experiments for WT and 57 independent experiments for D166V. The average duration of the ON time corresponding to the time the myosin remained bound to actin was 0.74 in WT and 2.46 in Tg-D166V muscle while the OFF time in WT and D166V was 2.74 and 5.8 respectively. Table 2 summarizes that the OFF time was approximately twice as long as the ON time.

Table 2: Ton and Toff times of transgenic WT and D166V muscle fibers:

Muscle	Tg-WT	Tg-D166V
ts (sec)	0.74 ± 0.09	2.46 ± 0.19
tc (sec)	2.74 ± 0.16	5.8 ± 0.17

Fig. 10 shows that t_{ON} is the time when the polarization signal is high, and t_{OFF} when the polarization is low. The sequence of events during isometric contraction of muscle can now be interpreted as follows: When a cross-bridge strongly attaches to actin the anisotropy is high (assumed here to be 1) because during the ON-time (t_{ON}) the rotational freedom of a cross-bridge is inhibited as demonstrated by the high anisotropy of cross-bridges in rigor. Phosphate release is followed by generation of tension, dissociation of ADP and the onset of rigor. Its end is marked by the binding of a fresh molecule of ATP, detachment of myosin from actin and the associated decline of the anisotropy signal because during the OFF-time (t_{OFF}) the rotational freedom is restored, as demonstrated by the low anisotropy of relaxed muscle. Finally, ATP is hydrolyzed to ADP and phosphate, and the cycle repeats with a period $t_{ON} + t_{OFF}$.

RESULTS:

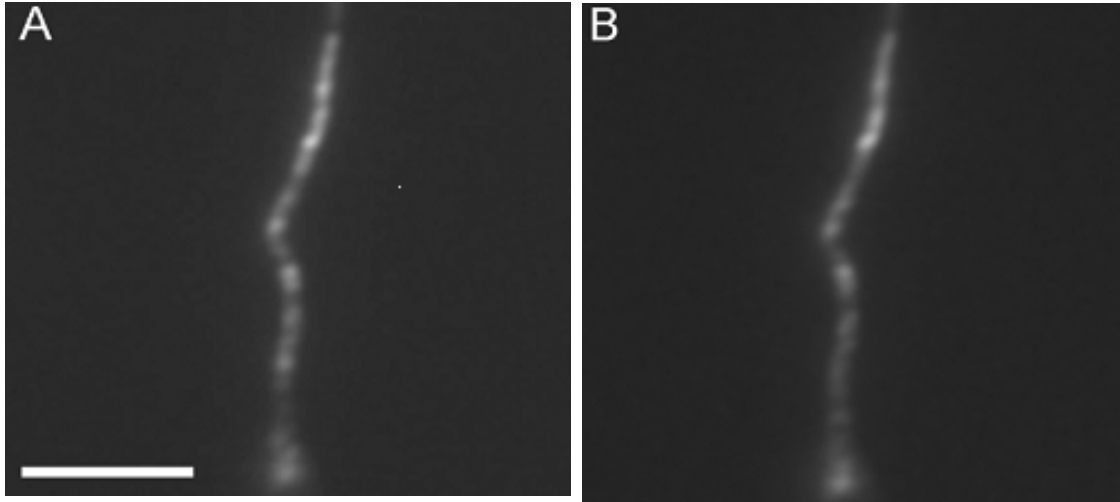


Fig 1: A typical Tg-D166V cardiac myofibril labeled with 1 nM RP at the beginning (A) and the end (B) of isometric contraction. Bar is 10 μ m. Notice that a sarcomere contains two I-bands.

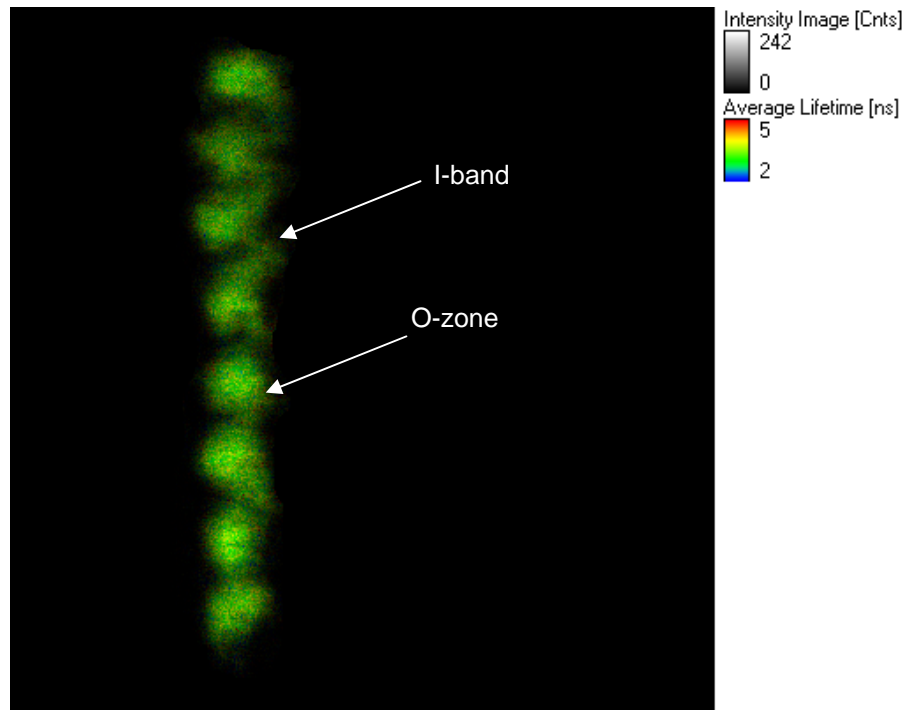


Fig 2: The image of a myofibril in rigor labeled with fluorescent phalloidin. The location of various bands is indicated by white arrows. Myofibril irrigated with 0.1 nM Alexa488-phalloidin + 10 μ M unlabeled phalloidin.

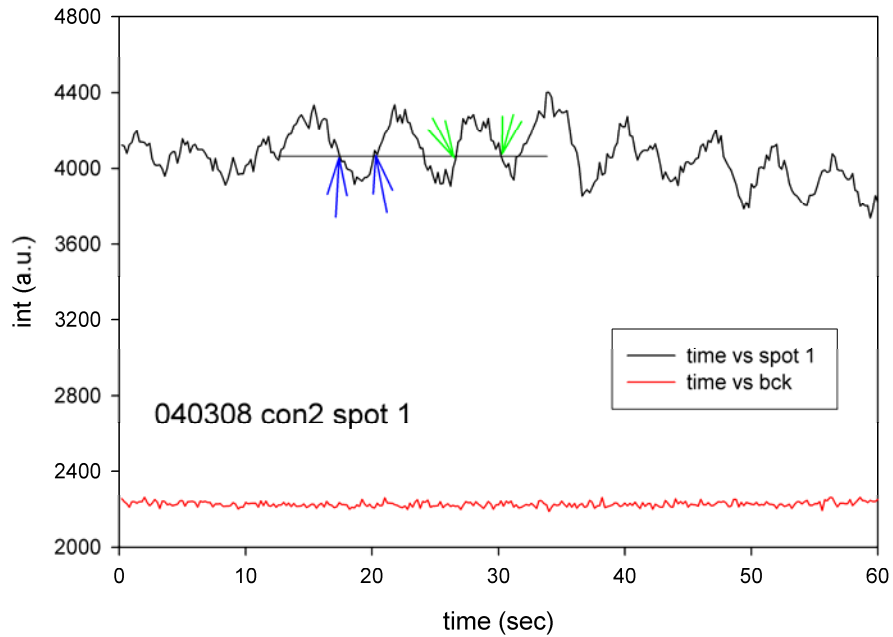


Fig. 3: Oscillation of fluorescence intensity of a single actin molecule in contracting cardiac myofibril. Intensity is high when the cross-bridge binds to actin, and low when it detaches from it. The duration of the ON state is defined as Full-Width-at-Half-Height (FWHH) of the impulses such as indicated by the green arrows. The duration of the OFF state (t_d) is defined as indicated by the blue arrows. Top trace: contracting muscle. Bottom trace (red): the background. Cross-linked myofibrils labeled with 1 nM RP. Note that the trace (top) is “sinusoidal” rather than a square wave.

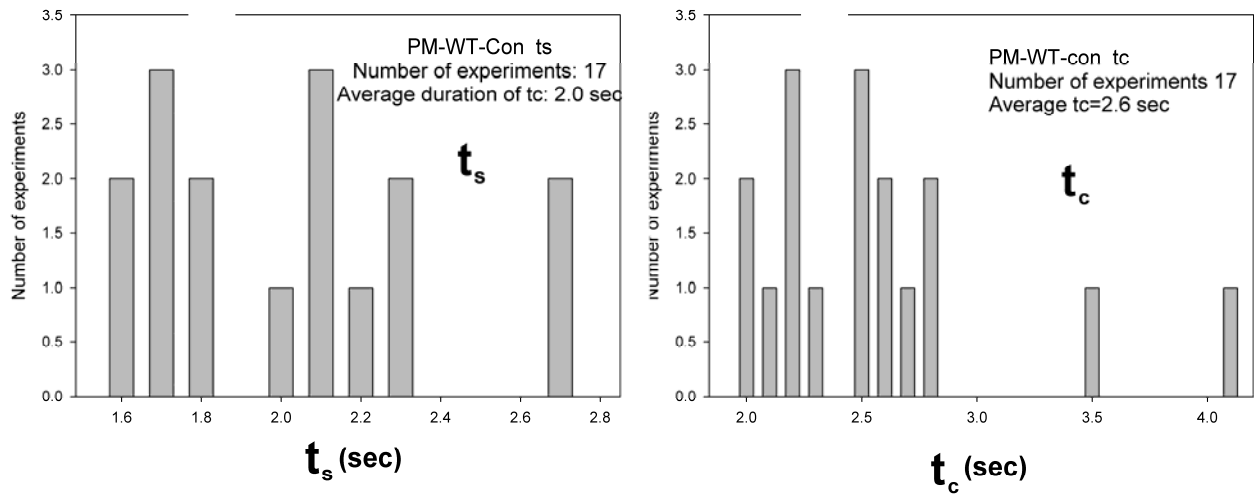


Fig 4: Left panel: Histogram of the times during which the intensities were high in contracting muscle. The mean t_s was defined as $\sum t_s N / \sum N$, where t_s is a given ON time and N is the number of measurements with this time. $SD=0.35$ sec. The total number of measurements was 17; the mean time was 2.0 sec. Right panel: The histogram of the durations of cycle. The mean duration was defined as $\sum t_c N / \sum N$, where t_c is a given duration and N is the number of measurements with this duration. $SD=0.54$ sec. The total number of experiments was 17. The average t_c was 2.6 sec.

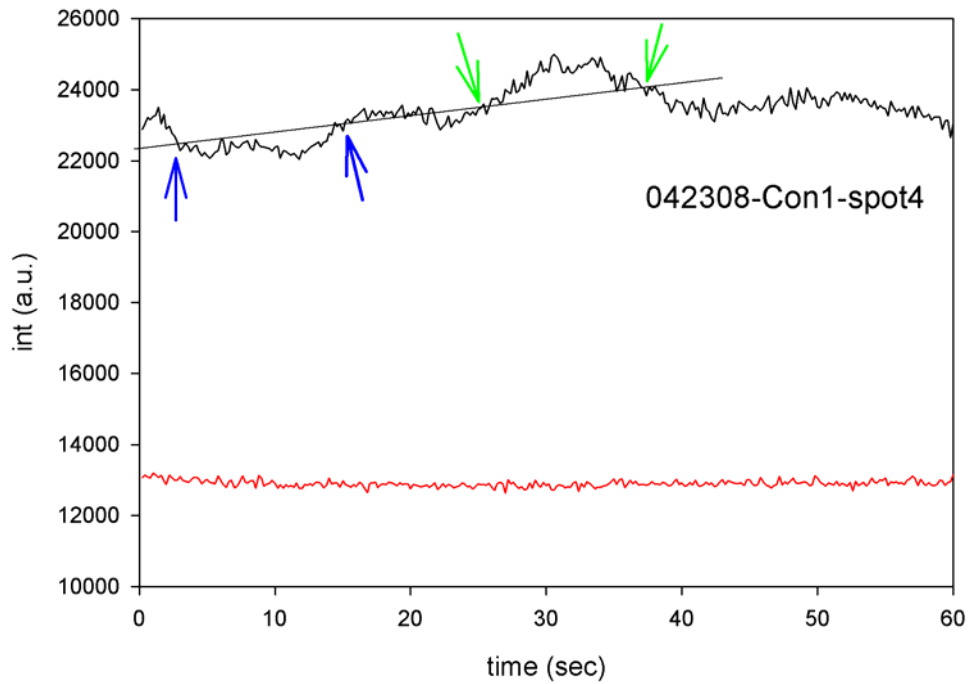


Fig. 5: Oscillation of intensity of single actin molecule in contracting Tg-D166V cardiac myofibril. The duration of the bound state, defined as FWHH as before, is indicated by the green arrows. The duration of the OFF state is indicated by the blue arrows. Top trace: contracting muscle. Bottom trace (red): the background. Cross-linked myofibrils.

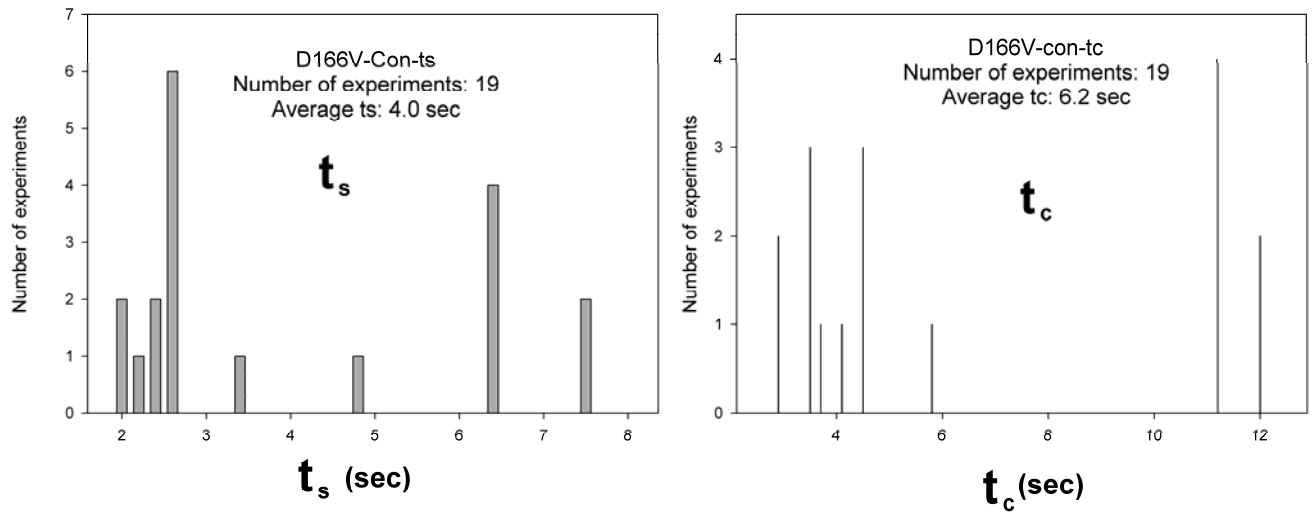


Fig. 6. Left panel: Histogram of the times during which the intensities were high in contracting transgenic mutated heart. The mean t_s were defined previously. $SD=2.06$ sec. The total number of measurements was 19; the mean time was 4.0 sec. Right panel: The histogram of the durations of cycle. $SD=3.51$ sec. The mean duration was defined previously. The total number of experiments was 19. The average t_c was 6.2 sec.

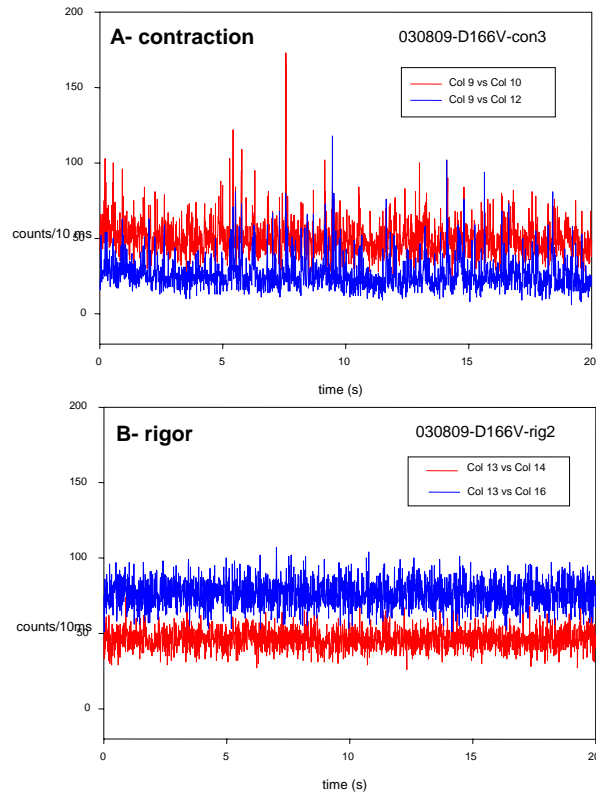


Fig. 7: The time course of polarized intensity of contracting (A) and rigor (B) myofibril. The data was collected every 10 μ s. The vertical scale is the number of counts during 1 ms. Note that the scale in both panels is the same. Myofibrillar axis is vertical on the microscope stage. Laser polarization is vertical on the microscope stage. Ch1 (red) and ch2 (blue) are the fluorescence intensities polarized perpendicular and parallel to the myofibrillar axis, respectively. Excitation 532 nm. Confocal pinhole was 50 μ m. The laser was polarized vertically (on the microscope stage). Myofibril was also vertical. Data collected with ISS Alba.

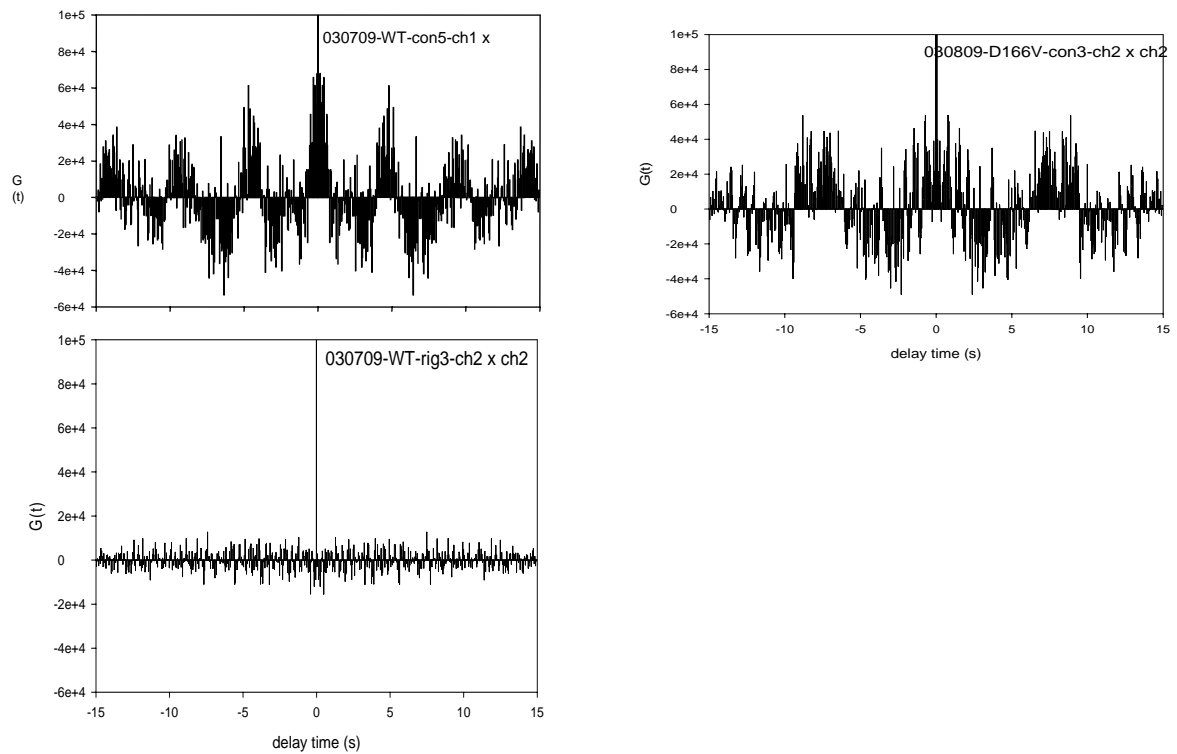


Fig. 8: The correlation function of contracting (A) and rigor (B) myofibril in WT myofibrils. Data was fitted to the exponential function, the exponential was subtracted from the data to get zero average value and correlation function was computed. In order to get correlations only between corresponding points, padded zeros have been added before the correlation calculation. 1000 points averaging was used. (c) Correlation function of contracting myofibril in D166V myofibrils.

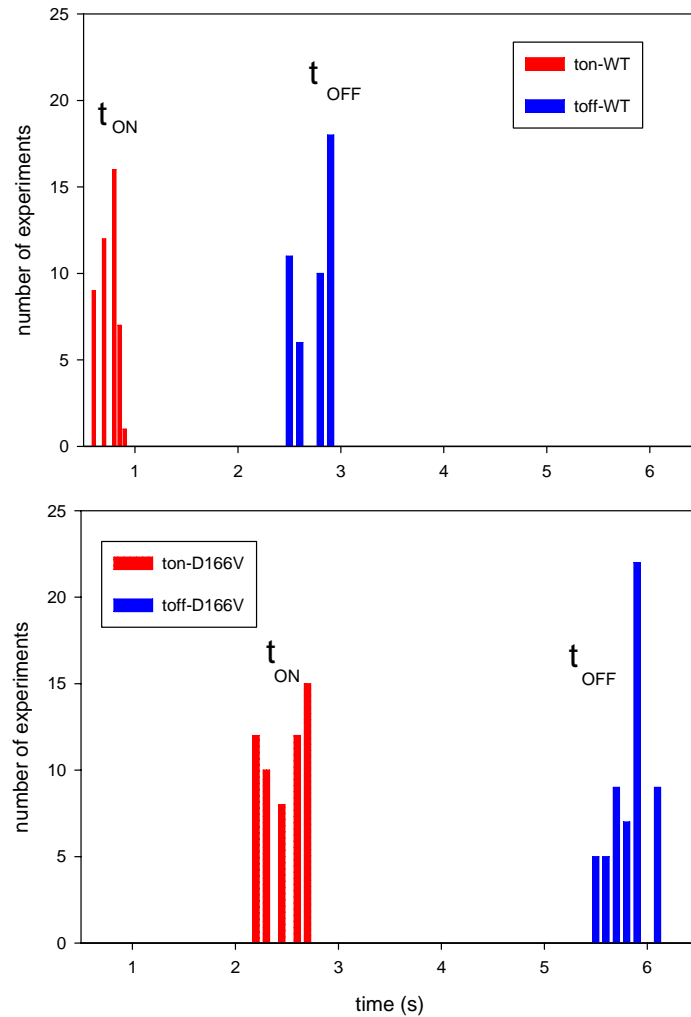


Fig 9: Histogram of the ON-OFF times in Tg-WT and D166V muscle. Upper panel: Histograms of the times during duty cycle in contracting Tg-WT heart muscle fibers: The total number of measurements was 45. T_{OFF} is 2.74 with a SD of 0.16 and T_{ON} is 0.74 with a SD of 0.09. . Lower panel: Histograms of the times during duty cycle in contracting transgenic mutated heart muscle fibers: The total number of measurements was 57. T_{OFF} is 5.8 with a SD of 0.17 and T_{ON} is 2.46 with a SD of 0.19.

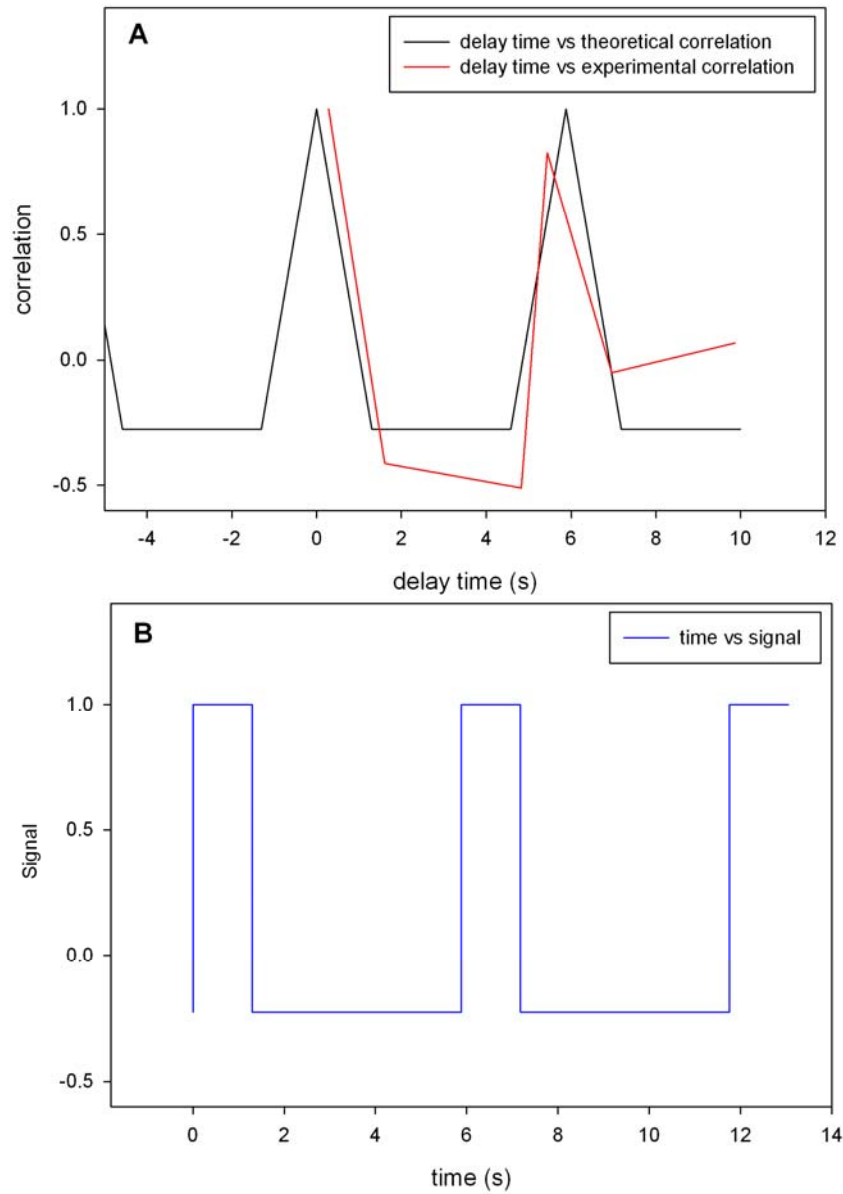


Fig.11. (A) - The best fit of the experimental autocorrelation function to the ideal saw tooth function (black). B - Blue signal is a result of deconvolution of saw tooth function.

Discussion:

Number of detected fluorophores: The fluorescent molecules remaining after the majority of fluorophores were bleached out; could not be destroyed in a few seconds. This fits our purpose well, because undiminished fluorescence for at least 10-20 sec is required to perform the experiment. The remaining molecules are probably located further from the focus of the laser beam than the bleachable ones. Although the photobleaching experiments mentioned previously fixed the average number of observed molecules at 1-2, it is impossible to perform such experiments on the actual spot selected for experimentation, because no fluorescence is left after complete photobleaching. The number of detected molecules in each experiment was instead estimated from signal intensity. This number varied between 1 and 4 and agreed within order-of-magnitude with the one determined from normalized $G(0)$.

The theoretical calculation of the number of detected molecules, based on the known ratio of phalloidin to actin, underestimates the number of fluorescently labeled actins: The length, width and height of a typical half-sarcomere (HS) are 1, 1, & 0.2 μm so its volume is $0.2 \mu\text{m}^3 = 2 \times 10^{-16}$ L. Since the concentration of actin in muscle is 0.6 mM, this volume contains ~80,000 actin monomers. Myofibril is labeled with 0.1 nM RP + 10 μM UP, i.e. only one actin in 10,000 carries fluorescent phalloidin. Therefore there are, on average, 0.08 fluorophores per HS. This is clearly a nonsensical value, because visual inspection of the image of myofibril labeled with 0.01nM RP + 10 μM UP shows more fluorophores per HS. The possible reasons are the overestimation of the concentration of filamentous actin in muscle and overestimation of myofibril concentration. Other possible reasons, not supported by independent evidence, include cooperativity of binding of phalloidin and “beacon” effects whereby myofibril captures light emitted by neighboring myofibrils.

The original signal can be retrieved from a correlation function by performing deconvolution of correlation. Fig. 11 shows the best least square fit of the experimental correlation function to a piecewise linear train of triangles (black lines). Such a train of triangles is the correlation function of a train of rectangular waves. The rectangular signal was calculated from the fitted triangle train. The calculation has two solutions. The most positive signal seems to be the more feasible than largely negative signal. The result is shown in Fig. 11B. The nomenclature assigned in Fig. 8 now becomes clear. Fig. 9 shows that t_{ON} is the time when the polarization signal is high and t_{OFF} when the polarization is low.

The t_c of cross-bridges of muscle carrying the D166V mutation in RLC are approximately 2.2-fold slower than corresponding times of Tg-WT. This hypothesis is supported by the measurements of ATPase activity. It is believed that splitting of one molecule of ATP leads to a single impulse. In vitro evidence, based on observation of the individual steps of smooth myosin, myosin V, myosin VI and kinesin, suggests that it is indeed so under unloaded conditions. But this does not necessarily have to be so in isometrically working muscle where a significant external load is applied to cross-bridges and where no gross mechanical work is performed. Here, splitting of one ATP molecule could lead to multiple mechanical cycles. Conversely, the energy of hydrolysis could be used for purposes other than performance of mechanical work. Our results suggest that this is indeed the case, because the observed average rate of change of actin orientation was much smaller than myofibrillar ATPase activity. The ATPase activity was seen to be increased in D166V as compared to WT.

In a parallel study, skinned and intact papillary muscle fibers from Tg-D166V mice were examined using a Guth Muscle Research System and the effects of the D166V mutation compared to Tg-WT and NTg (non-transgenic) mice (personal communication of Dr. D.

Szczesna-Cordary). A large increase in the Ca^{2+} sensitivity of force and ATPase ($\Delta p\text{Ca}_{50}$ higher than 0.25) measured simultaneously under isometric conditions was determined in skinned muscle fibers from Tg-D166V mice compared to control NTg and Tg-WT mice. This D166V mediated increase in the Ca^{2+} sensitivity of force and ATPase was shown to be due to a large decrease in the cross-bridge dissociation rate (g), expressed as the ratio of fiber ATPase/concentration of cross-bridges attached at all levels of force activation. This supports our hypothesis that the D166V mutation must be introducing more bulkiness near the protein backbone and put restrictions in the conformations that the main chain can adopt, which leads to alterations in myosin cross-bridge kinetics, thus affecting the duty cycle. The slow force relaxation rate of the fibers could potentially result in diastolic dysfunction of the D166V mutated myocardium. Abnormal diastolic filling of the heart could also lead to a decreased stroke volume causing systolic dysfunction. These changes if severe enough would ultimately result in compensatory hypertrophy and could lead to sudden cardiac death as observed in the individuals harboring the D166V mutation.

CHAPTER VI

SPECIFIC AIM 3

Specific Aim 3: Developing methods to improve imaging in muscle.

Rationale

In the second specific aim, we studied the RLC D166V mutation which was over-expressed at 90% in the Tg myocardium. In general, however, it is essential to have a technique capable of monitoring single molecules. Human patients are normally heterozygous for FHC mutations, so their myosin containing thick filaments are composed of wild type myosin heads interspersed with FHC mutant heads. Any large observational volume thus contains a mixture of WT and FHC molecules, making the comparison between kinetics of healthy and diseased muscle impossible. Therefore, the unambiguous determination of myosin cross-bridge kinetics requires that the experiments are carried out at the level of a single molecule to avoid averaging over ensembles of molecules with different kinetics.

In this specific aim, we work towards developing new technologies to aid studying single molecules in a biological system. In order to obtain information from individual molecules, it is necessary to collect data from an extremely small volume, small enough to contain a single molecule. To collect data from a small volume with sufficiently high signal-to-noise (S/N) ratio requires that the rate of photon detection per molecule be high, which necessitates illuminating

the muscle with an intense laser beam. This in turn leads to rapid photobleaching of the fluorophores used in labeling. In this specific aim, we explore ways to minimize the detection volume (sub aim 1) and the ways to decrease photobleaching (sub aim 2 and 3).

a) Surface Plasmon Coupled Emission (SPCE)

Introduction

Muscles contract due to interactions of myosin cross-bridges with actin. It is important to study dynamics of this interaction in muscle, because behavior of proteins *in vivo* may be quite different than *in vitro*. In solution proteins are loosely packed, whereas *in vivo* they are crowded. Molecular crowding influences protein solubility and conformation (67). The effect of crowding is particularly severe in muscle, where the concentration of actin and myosin are 0.6 mM and 0.24 mM, respectively (7). Actin and myosin are meant to operate in such crowded environments, as evidenced by the fact that their K_m is in the μM range, but crowding may impose constraints affecting both their structure and function so that their properties in dilute solutions may be different than in muscle (4).

In addition, myosin cross-bridges act asynchronously i.e. at any time during muscle contraction each is in a different part of a mechanochemical cycle. Therefore measurement taken at any time during contraction is an average value. There are two ways to overcome this problem. The first way is to synchronize many crossbridges by a rapid step of tension or length. The time course of relaxation back to equilibrium is then followed (14, 15, 50). However, application of transient itself disturbs steady-state. The second was to follow rotation of a single cross-bridge during steady-state contraction. In this paper we describe a novel method of doing this in skeletal muscle.

To be able to obtain information from individual molecules in muscle, it is necessary to collect data from an extremely small volume, small enough to contain few molecules. The observational volume of conventional wide-field microscopes is much too large ($\sim 10^{-9}$ L). The introduction of small observational volumes defined by diffraction-limited laser beams and confocal detection made it possible to limit the observational volume to a femtoliter (10^{-15} L) and eliminate much background noise (36). However, such volumes are still too large. If molecules are to be observed at μM concentrations, the volume must be of the order of attoliters (10^{-18} L).

Here we describe a technique combining the principles of Confocal TIR (Total internal reflection) and Surface Plasmon Coupled Emission (SPCE) methods. SPCE has been described in free standing configuration and has been used to detect single molecules. Recently, it has been applied to a microscope. In the current application of this technique, the observational volume is made shallow by placing a sample on a thin metal film and illuminating it with the laser beam at Surface Plasmon Resonance (SPR) angle. The laser beam is able to penetrate the metal and illuminate a myofibril. Excitation light produces an evanescent wave on the aqueous side of the interface. The concept is shown in Fig. 1. The thickness of the detection volume is a product of evanescent wave penetration depth and distance-dependent coupling with surface plasmons. It is further reduced by a metal quenching of excited fluorophores at a close proximity (below 10 nm). As a result, the detection volume is ~ 50 nm thick. The fluorescent light is emitted only at an SPCE angle (on a surface of a cone in 3D). A confocal aperture inserted in the conjugate image plane of the objective reduces lateral dimensions of the detection volume to ~ 200 nm.

Results

Demonstration of SPCE in the microscope

It has been demonstrated here the ability to image muscle in aqueous solution by SPCE microscopy. 20 ml of a suspension of myofibrils in rigor solution was placed on an Olympus high refractive index coverslip coated with a 48-nm layer of gold. The fluorescence was observed at different angles of incidence. The sample was illuminated by collimated beam of 532-nm light at an angle defined by the turn of a TIRF attachment micrometer screw. Fig. 2 demonstrates the enhancement of fluorescent signal caused by the SPCE phenomenon. The angle varied between 30° (corresponding to ~ 12 reading of the micrometer screw) to 70° (corresponding to 30 reading of the micrometer screw). The angle was initially set at 70° , too large to enter the back aperture of the TIRF objective. The resulting intensity was equal to the background. The angle was then progressively decreased, which caused an increase of intensity. At $\sim 50^\circ$, a faint image of myofibrils appeared, indicating that the TIRF angle had been reached. When the SPR angle was reached at $\sim 60^\circ$, the intensity increased sharply to a peak, indicating SPCE excitation. Further decrease in angle caused the intensity to decline, indicating epifluorescence excitation. This phenomenon manifests itself under the microscope in a spectacular way. When the angle of a laser beam incidence is high, above the SPR angle, the viewing area under the microscope is dark. With the angle change, the strong glaze appears. With further angle decrease, the glaze vanishes, as is shown in sequential photographs in the top of Fig. 2.

Fig. 3 shows an SPCE image of a myofibril labeled with $0.1 \mu\text{M}$ fluorescein phalloidin. Despite the fact that phalloidin attaches to actin, the I-bands are not well labeled. This is consistent with earlier observation that in skeletal muscle (in contrast to cardiac muscle)

phalloidin first labels the ends of actin filaments. Several hours are needed for the I-bands to label uniformly. Because the current experiment was done ~15 min after labeling, the fluorescence originates mostly from the overlap zone. The SPCE image is well resolved, as would be expected from the near-field technique. Most likely background suppression by gold contributed to this effect. With a high-NA (=1.65) objective, the image can be obtained with both 488 and 532 nm excitation, on cover slips covered with gold and silver, on high-refractive-index cover slips made by Olympus, and on cover slips made from sapphire.

Comparison of TIRF and SPCE images of muscle

We compared images of myofibrils on glass and high refractive index cover slips from Olympus. One set was coated with a 48 nm layer of silver and a 2 nm layer of silicon, the second set was coated with a 48 nm layer of gold, and the third set was left uncoated. We used a 100X (NA=1.65) objective from Olympus and n=1.78 (Cargill) oil, 1 mg/ml myofibrils were labeled with 0.1 μ M fluorescein-phalloidin and observed in rigor solution (not dry). The same myofibril could not be observed (because we used three different cover slips), but each myofibril came from the same batch. Subjective impression (Table 1) was that the SPCE image was better on gold than on silver.

Coverslip Excitation	Glass uncoated	Quartz uncoated	Sapphire uncoated	Olympus uncoated	Sapphire coated with gold	Olympus coated with gold	Olympus coated with silver
TIRF	+++ ^a	+++	+++	++	++ (dim)	++ (dim)	++ (dim)
EPI	++ ^b	++	++	++	++	+	-
SPCE	NP ^c	NP	NP	NP	+++	+++	++

Excitation was with Argon laser at 488 nm. a: +++ very good, ++ good, + fair, - inferior.

b: images are good because myofibril is thin (~0.5 μ m). c: Not Possible.

The quality of image of myofibrils was comparable in TIRF and EPI, no doubt because myofibrils are very thin. In the case of SPCE, the intensity of images was greater with p-polarization, in accordance with theoretical.

The thickness of the detection volume

Consider a slab-shaped material interposed between the glass and water interfaces. The metal (~ 20 nm for Al, 50 nm for Au or Ag) film is characterized by a complex dielectric constant. Incident light (TIR) transmits through the glass/metal interface, undergoes multiple reflections between the metal/water and glass/metal interfaces, and then emerges as a refracted ray in the water medium. At the SPR angle, the light impinging from the prism induces surface plasmons. The plasmon resonance strengthens the electric field in the excitation evanescent wave, as shown in Fig. 4. Insertion of the metal film dramatically perturbs the $z = 0$ field intensities in the water medium. The film reflects or absorbs s polarized incident light, permitting negligible light transmission for all incidence angles. Similarly, the film reflects or absorbs p-polarized incident light, permitting negligible transmission for almost all angles. However, a dramatic enhancement of transmission occurs in a narrow peak for incidence angle $\Theta_{\text{SPR}} \sim 57^\circ$, an angle larger than the critical $\Theta_{\text{critical}} \sim 50.32^\circ$. Angle Θ_{SPR} is the surface plasmon angle where transmission enhancement results from the resonant excitation of electron oscillations (surface plasmons) propagating along the water/metal interface. This phenomenon occurs at interfaces where constituent materials have real parts of the dielectric constants of opposite signs. Like the evanescent field for p-polarized incident light in TIRF, polarization is elliptical but approximates linear polarization along the z-axis, and intensity decays exponentially in the distance z from the interface (6, 94). Both polarization and field depth depend on incidence angle. Hellen and

Axelrod pointed out that for a fluorophore under steady illumination, the dissipated power must equal the absorbed power, implying that a fixed-power, rather than a fixed-amplitude, dipole radiator is the appropriate model for probe emission near an interface. An important consequence of this model, observed for cells adsorbed to metal-coated glass (47), is that the metal film totally quenches fluorescence from probes within ~ 10 nm of the interface.

To calculate the power flow into the objective, we define the polar angle of the fluorophore transition moment (Θ) and the azimuthal angle (ϕ) as usual (Fig. 5, top). The bottom part shows the average power of SPCE emission versus the distance of the fluorophore from the metal for two orientations of the fluorophore transition moment. The metallic layer considered here is a 48-nm-thick layer of gold deposited on high-refractive-index glass ($n=1.78$). The refractive index of medium was taken as 1.37 to mimic that of muscle. The excitation was at 633, and emission at 670 nm. The distance dependence is no longer exponential. The half-widths of the SPCE fluorescence volumes are 70 nm and 40 nm for orthogonal and parallel dipoles, respectively. Because fluorescence is totally quenched from the volume within 10 nm from the interface, we estimate that fluorescence is originating from the 50-nm- and 20-nm-thick layers. This translates to a detection volume of ~ 2 attoL.

Sensitivity to the rotational motion

SPCE is particularly useful in measuring rotational motion. This is because coupling of fluorescence to surface plasmons dramatically depends on the orientation of the molecule transition moment. The coupling is very efficient for the orthogonal dipole orientation (p-polarization) and not efficient for dipole orientation in the plane of metal surface (s-polarization). Consider the simple three-layer system shown in Fig. 6 (top panel). For such a system, transition

moments orthogonal to the metal surface will preferentially couple to surface plasmons, and only p-polarized SPCE can be observed. The decay times, the probability that an emitted photon goes into the objective, and the percentage of the photons in the glass prism that are p-polarized depend on the fluorophore position and transition moment orientation. The dependence is quantified in Fig. 6 (bottom). It is seen that TIRF illumination yields 5.3 times more power into the objective for vertical than horizontal orientation of the transition dipole. In contrast, SPCE illumination yields 18.6 times more power into the objective for vertical than horizontal orientation of the transition dipole. The average sensitivity is therefore 3.5 times greater for the SPCE than for TIRF.

Number of observed molecules

Data were always collected from the overlap zone of a myofibril. Fig. 7 (left) shows the projection of the confocal aperture on the overlap zone. Because ~20% of muscle weight is actin, the concentration of actin in a solution of 1 mg/ml myofibrils is ~4.6 μM . We used 0.1 μM of fluorescent phalloidin (together with 9.9 μM nonfluorescent phalloidin), i.e., there were ~9 phalloidin molecules per actin filament. If the phalloidin was uniformly distributed, the 0.2 μm -wide detection volumes would have contained ~2 phalloidins /filament. However, because of nonhomogeneous distribution of phalloidin (Fig. 3), most of the fluorophores are located in the distal ~1/3 of a filament. We therefore detect signal from ~6 phalloidins / filament. Spacing between actin filaments is ~30 nm (7). Because the thickness of the detection volume is ~50 nm, we observe ~2 layers of thin filaments. We conclude that we observe ~12 actin monomers labeled with phalloidin.

Confocal SPCE signal from a myofibril.

The projection of the confocal aperture was placed over the overlap zone. Typical signal obtained from a voxel located in the overlap zone is shown in Fig. 8 A. The signal/noise (S/N) ratio is determined by the rate of detection of fluorescent photons per molecule of the dye in one bin width $\delta\tau$. Bin width is defined as the time interval into which the data collection time is subdivided. The necessary data collection time is determined by the characteristic time for relatively slow hydrolysis, i.e., ~ 0.5 s. During this time we wish to measure at least five data points, i.e., $\delta\tau \sim 100$ ms. Each step corresponds to bleaching of one molecule. We detect ~ 40 – 80 photons/molecule/bin (Fig. 9 B). Assuming Poisson-distributed shot noise as the sole noise source, the S/N ratio is ~ 7 .

FIGURES

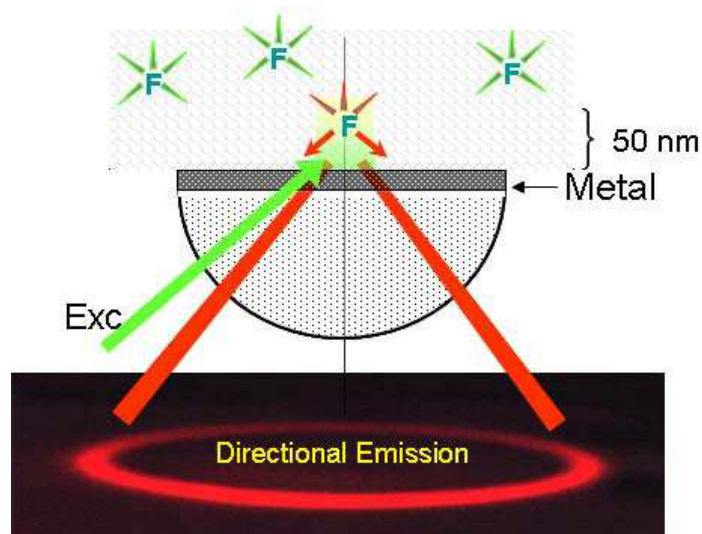


Fig. 1. Concept behind confocal SPCE microscope. The fluorophores are placed on metal coated cover slip and excited with green light at an SPR angle. The excitation energy couples to the surface plasmons and radiates to the glass prism (red) as a surface of a cone with half angle equal to SPCE angle. Metal can be a thin layer of Al (20 nm thick) or Ag or Au (50 nm thick). The picture of the directional emission is taken from the real experiment.

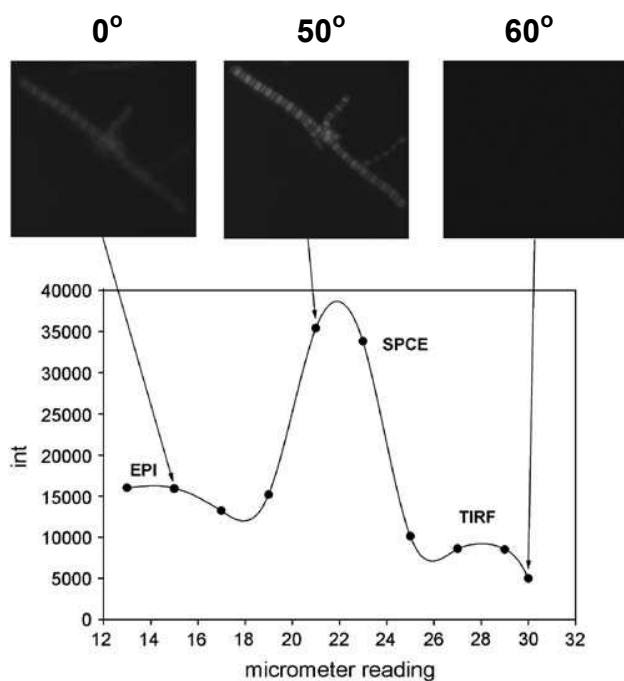


Fig. 2: SPCE signal from skeletal myofibrils as a function of the illumination angle. The top panel shows photographs taken from the microscope for various illumination angles. Myofibrils labeled with 0.1 μM fluorescein-phalloidin. $\lambda_{\text{ex}} = 488 \text{ nm}$. Images analyzed by ImageJ. The numbers above the panel indicate the micrometer screw angle at which SPCE and TIRF was achieved.

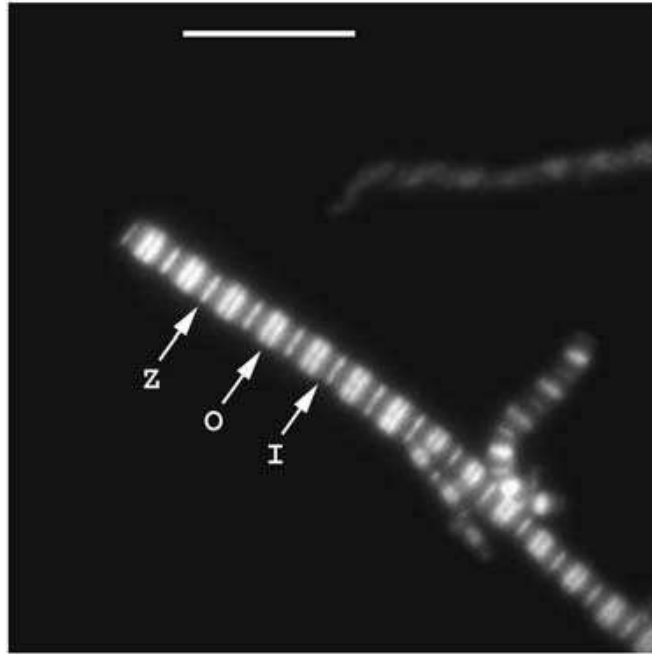


Fig. 3: SPCE image of myofibril in rigor. Myofibril labeled with 0.1 μM fluorescein-phalloidin on gold cover slips. The image was contrast enhanced to emphasize superior resolution of the method: Z is the Z-line, O is the overlap zone, I is the I-band. Bar is 10 μm .

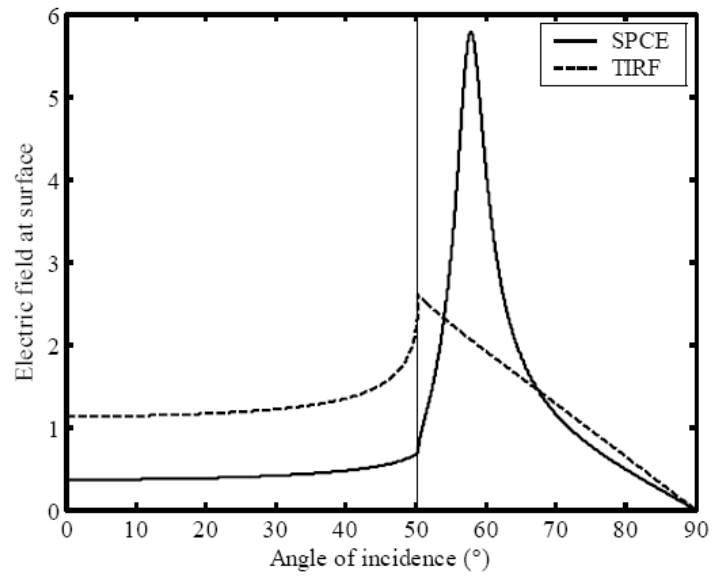


Fig. 4: Electric field of the evanescent wave at the surface. It is normalized to the electric field of the incident wave. Gold layer of 48 nm; excitation wavelength = 633 nm; maximum field at 57.86° ; critical angle is 50.32° ; integral from critical angle to 90° is 63.27 (solid line, SPCE; broken line, TIRF).

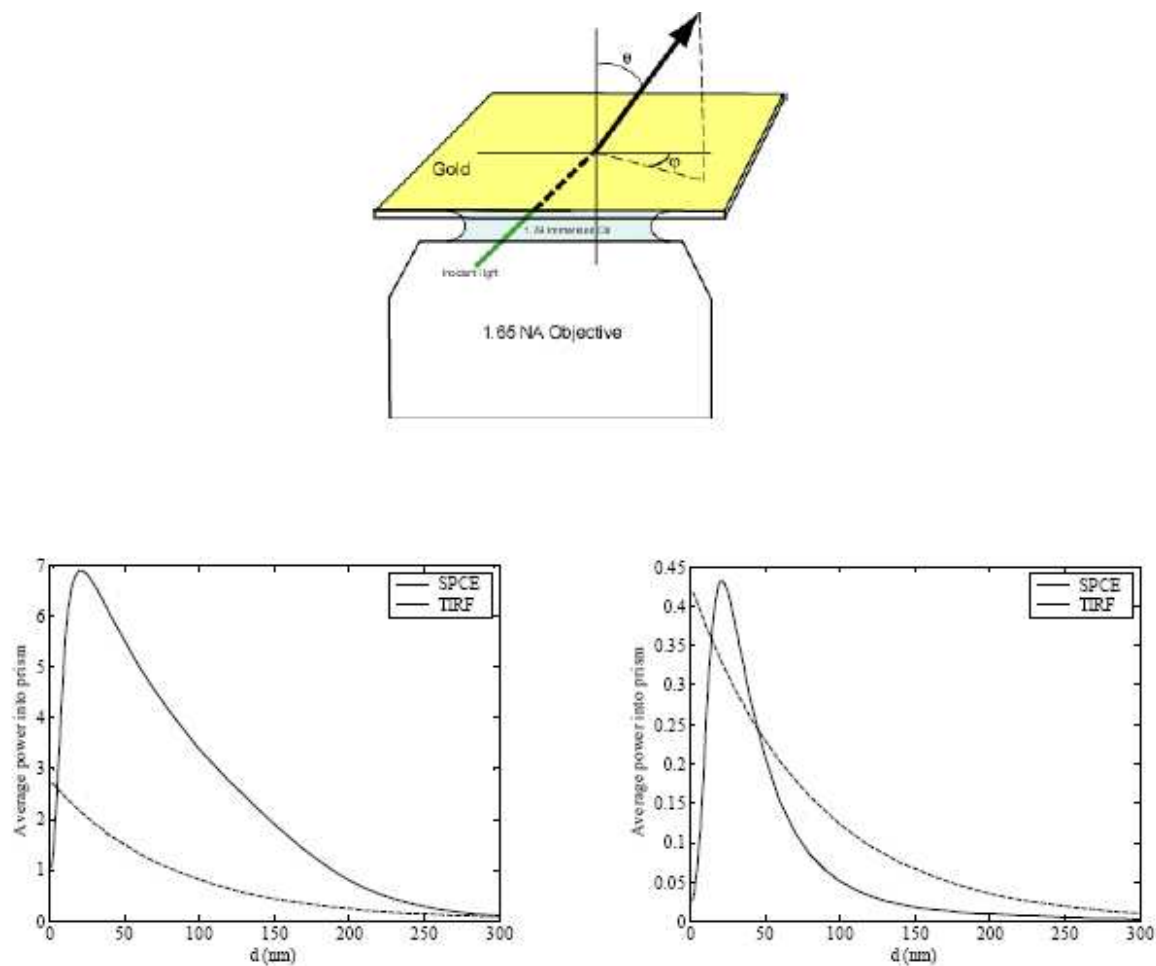


Fig. 5: (Top) Definition of angles. (Bottom) Calculated power flow to the objective in the SPCE experiments for (left) $\theta = 0^\circ$, i.e., p-orientation and (right) $\theta = 90^\circ$, i.e., s-orientation of the transition moment. The time between excitation of the fluorophores is assumed much longer than the emission time. Note that the power of the p-polarization is ~ 10 times greater than that of s-polarization. Gold layer of 48 nm, excitation wavelength = 633 nm, at maximum field (57.86°), emission at 670 nm (solid line, SPCE; broken line, TIRF). The strong dissipation of energy into the metal layer for short distances lowers the power in SPCE but not in TIRF.

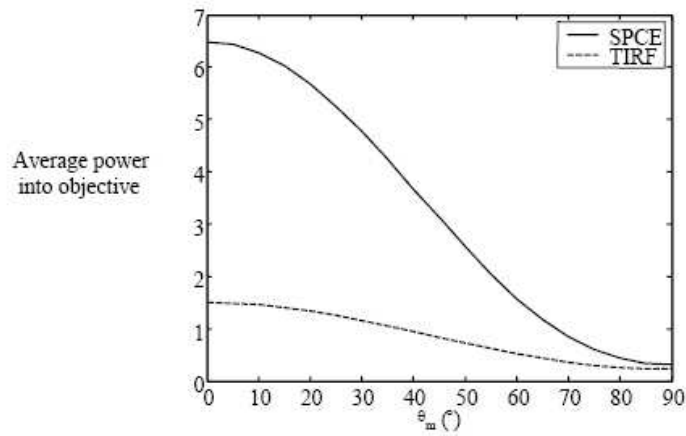
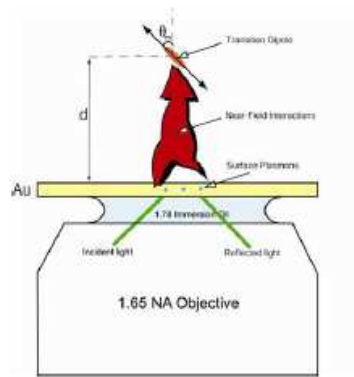


Fig. 6: Coupling of fluorescent dipole moments to surface plasmons (top) and comparison of the dependence of the transition moment angle for TIRF and SPCE (bottom). 48 nm gold layer; $\lambda_{ex} = 633$ nm; maximum field (57.86°); emission at 670 nm; $d = 50$ nm.

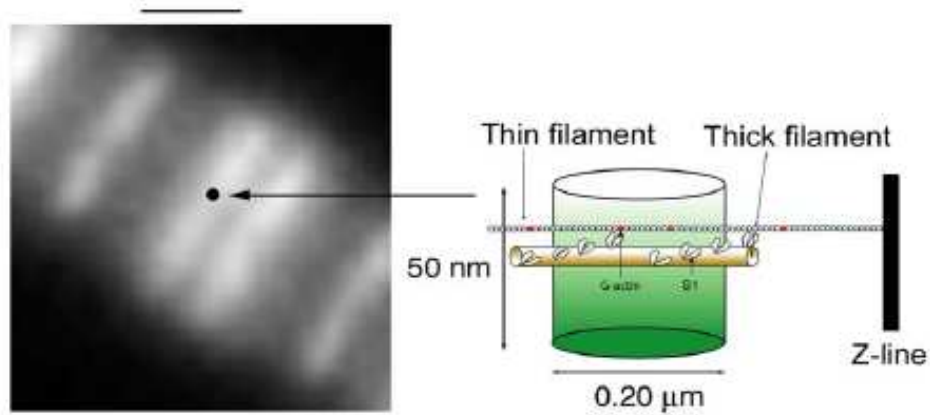


Fig 7: Fluorescent image of the overlap zone. The black dot is a projection of the confocal pinhole on the image plane. Right - Schematic diagram of the voxel. The fluorescently labeled actin monomers are red. The observational volume is ~ 50 nm thick and has a diameter of ~ 200 nm, corresponding to the diffraction limit of the 1.65 NA objective. The resulting detection volume is ~ 2 attoL. Bar = $1 \mu\text{m}$.

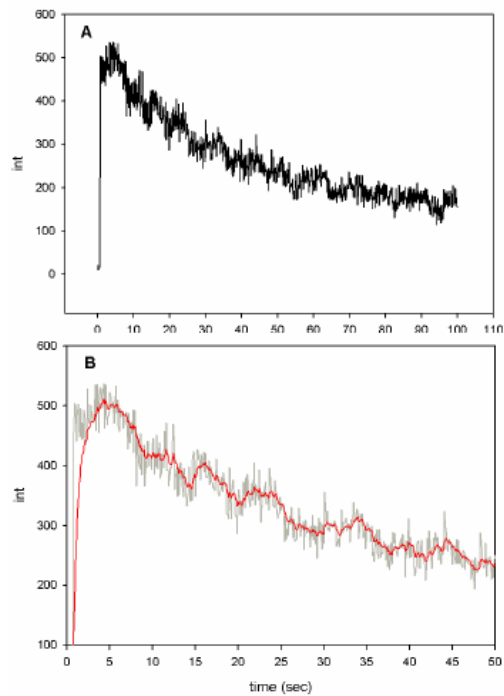


Fig. 8: Confocal SPCE signal from rigor myofibril. The data were collected from the overlap zone. Myofibril labeled with $0.1 \mu\text{M}$ rhodamine phalloidin on gold cover slips. The exciting light was perpendicular to the plane of the coverslip (p-polarization). (A) Fluorescence intensity. (B) Intensity on expanded scale: gray, original signal; red, low-pass filtered.

DISCUSSION

These results make it clear that the long-term objective, to observe a single molecule of a contractile protein during contraction of muscle, is feasible. The fact that the method gives exceedingly small detection volume allows detection of a single molecule of myosin or actin in muscle. In the example used here, we observed 12 actin protomers. The instrument has enough sensitivity to detect labeling with 0.01 μM phalloidin; i.e., a single molecule can be detected.

Because the SPR angle is narrowly defined, only a fraction of the light incident on a sample in TIRF illumination is able to penetrate the gold coating in SPCE. This resulted in a decrease in photobleaching. At the same time, the S/N ratio was not affected much because of resonance plasmon coupling. The dramatic dependence of fluorescence coupling of surface plasmons on the orientation of the molecule transition moment makes the method useful in measurements of orientation changes (Fig. 6). Because muscle contraction involves rotation of myosin cross-bridges (50), and actin monomers (15). SPCE is particularly suited to studies of muscle contraction. The directional character of SPCE enables excellent suppression of unwanted noise. The microscope uses KR configuration, where the observed SPCE signal is almost not perturbed by the DCM background (Fig. 7, right, bottom panel).

The quality of SPCE image was superior to conventional epi illumination (Table 1). One would expect the thickness of the myofibrillar sample to be irrelevant to the quality of the image because myofibrils are only ~ 0.5 μm thick. Apparently, this is not so; myofilament disarray is already evident at the nanometer scale. Particularly impressive was the fact that the break in the overlap zone corresponding to the M-band was clearly seen (Fig. 3). The TIRF image was equally good (Table 1), but advantages of SPCE over TIRF mentioned earlier make SPCE the method of choice for measuring rotation of single molecules. The confocal SPCE signal (Fig.9)

was measured from a rigor myofibril, but signal can easily be obtained in contracting muscle using cross-linking to inhibit shortening (20). Labeling muscle actin with phalloidin is particularly advantageous. First, labeling does not affect enzymatic properties of muscle (28). Second, phalloidin labels the overlap zone, an area where mechanical interaction between actin and myosin occurs (3). Third, the concentration of label is easily controlled by saturating all actins with a mixture of labeled and unlabeled phalloidins. For example, in the current experiments, we always used 0.1 mM fluorescent phalloidin and 9.9 μ M unlabeled phalloidin. Because rotation of actin monomer to which phalloidin is rigidly attached parallels rotation of a cross-bridge, the rotational signal from phalloidin (Fig. 9) is a preferred way to follow cross bridge rotation in muscle.

The steps visible in Fig. 9 could arise from 1) photobleaching of rhodamine, 2), rotational motion of the transition moment, or 3), be simply a result of noise. We think that the first is the case. Rotational motion is an unlikely reason because cross-bridges in rigor muscle do not rotate. Noise is an unlikely reason because we observe steps in nearly all experiments. Also, the number of steps roughly corresponded to the number of fluorophores in the detection volume.

Each step lasted \sim 10 s and led to the loss of \sim 70 cpb (Fig. 9 B), i.e., we observed \sim 7000 photons from a fluorophore before it bleached out. The geometric collection efficiency of the instrument is \sim 2%, i.e., a fluorophore emitted a total of \sim 0.4 \times 10⁶ photons before irreversible bleaching. This is consistent with known photostability of Rhodamine (35).

In general, the SPCE method will find application in experiments where data from large assemblies of molecules complicate interpretation. Examples are single-molecule detection on cell and model membranes, ligand-receptor interactions in live cells (e.g., insulin and galanin binding to receptors), involvement of protein molecules in internalization of bacteria by cells,

monitoring the conformational fluctuations of DNA, diagnosis of prion diseases, behavior of myosin in muscle, and detection of a virus at an early phase of infection. The fact that SPCE quenches fluorescence from a layer ~ 10 nm immediately adjacent to the surface suggests an application to the study of membranes.

b) Silver island films (SIFs)

Introduction

Here we show a way to significantly decrease photobleaching. It is based on the fact that silver island films (SIF) increase brightness of fluorescence and significantly decrease fluorophore fluorescence lifetime. The factors that contribute to the overall brightness are the quantum yield of a fluorophore, the strength of the local electromagnetic field, and the quenching. In conventional fluorescence, the changes in quantum yield (Q) or fluorescence lifetime (τ) always occur by modulation of the nonradiative rate constant (k_{nr}), be it by solvent relaxation, nonradiative decay, quenching by the solvent, or transfer of the energy to an acceptor. The radiative rate constant Γ remains constant. Thus an increase of quantum yield

$$Q = \Gamma / (\Gamma + k_{nr})$$

always results from a decrease of the rate of nonradiative decay k_{nr} . Similarly, a decrease in k_{nr} always causes an increase of fluorescence lifetime:

$$\tau = 1 / (\Gamma + k_{nr})$$

In contrast, the proximity of fluorophores to metallic particles provides an opportunity to modify radiative rate Γ (58). For example, suppose that the metallic particles result in γ -fold increase in the radiative decay rate to $\Gamma_{mod} = \gamma\Gamma$. The fluorescence becomes brighter because quantum yield now becomes $Q = \gamma\Gamma / (\gamma\Gamma + k_{nr})$, i.e., it becomes closer to the maximum value of

1. But in contrast to the conventional case, the fluorescence lifetime is decreased, because it now becomes $\tau = 1/(\gamma I + k_{nr})$.

The most important consequence of the increase of brightness and the decrease of lifetime is decrease of photobleaching. Increase of brightness effectively decreases photobleaching because, to collect a given number of photons, the sample can now be illuminated with a weaker laser beam. An additional benefit of the weaker excitation power is a lower level of the emissive background. Decrease in fluorescence lifetime has the effect of decreasing photobleaching because bleaching occurs when a fluorophore is in the excited state. The decrease of lifetime minimizes the probability of attack by oxygen during the time that the molecule is in the excited state.

Results

Increase of brightness

To study increase in brightness, myofibrils were placed on glass cover slips or SIF coated glass cover slips and illuminated with a 5-mW laser beam at 532 nm. SIF coating of the coverslip results in the enhancement of fluorescence (Fig. 9). The fluorescence was recorded with Nikon Coolpix 995 camera through a 540-nm long wave pass glass filter. The average intensity of fluorescence was 4.5 times greater on SIF than on glass. In parallel, the emission spectra were recorded by placing the plane of the microscope slide at 45° angle with respect to the direction of the laser beam. As expected, no difference in the emission spectra was detected. This is consistent with earlier results using Texas red-labeled bovine serum albumin (60). The intensity of fluorescence at 575 nm was enhanced 4 times. The difference from the value of 4.5 obtained by direct measurement is most likely due to the reflections associated with front-face

illumination. Fig. 10 shows confocal images of the same myofibrils on glass (Fig. 10A) and SIF (Fig. 10B). The fluorescence originates from the overlap zones because phalloidin originally attaches to the ends of thin filaments of skeletal muscle (3). Several hours are needed for the I bands to label uniformly (18). Since the present experiment was done ~15 min after labeling, the fluorescence originates mostly from the overlap zone (O-bands).

As shown in Figs. 10A and 10B the silver coating may lead to denser attachment of myofibrils compared to glass. However the overall brightness increase is due not exclusively to the density effect but also to increased brightness of individual fibrils. To demonstrate this, we compared brightness of the O-bands of the individual myofibrils. Fig. 11 is a representative gallery of images of myofibrils on glass (left column) and SIF coated glass (right column) using TIRF illumination. To prevent the images on SIF from being saturated, the gain of the camera was kept small and constant. The SIF decreased the quality of images due to refraction by silver particles, but it was sufficiently good to resolve striations. The average fluorescence intensity of the O-bands of myofibrils on glass was 56 (min = 20, max = 128). The average fluorescence intensity of the O-bands of myofibrils on glass covered with SIF was 224 (min = 51, max = 246), a four fold enhancement.

Decrease of fluorescence lifetime

As mentioned before, the distinguishing feature of modification of radiative rate by the proximity of fluorophores to metallic surfaces is the fact that the fluorescence lifetime is decreased (58, 63). To determine whether the fluorescence lifetime of myofibrils indeed becomes smaller in the presence of SIF, we compared lifetime of myofibrils on the respective surfaces. Fig. 12 shows that SIF causes the fluorescence lifetime to significantly decrease. The decay of

fluorescence of myofibrils on glass was best fitted by three exponentials with lifetimes $\tau_1 = 3.607 \pm 0.032$, $\tau_2 = 1.486 \pm 0.025$ and $\tau_3 = 0.254 \pm 0.014$ ns with the relative contributions to the total intensity of 51.93, 38.35, and 9.72%, respectively. The exponentials decaying with the slow lifetimes (τ_1 and τ_2) contributed 90.28% of the total intensity. The remaining 9.72% was contributed by the fast decay (τ_3). The exponentials decaying with slow and fast lifetimes contributed 51.27 and 48.73% of the total amplitude. The amplitude weighted average lifetime was 1.275 ns. The decay of fluorescence of myofibrils on SIF was best fitted by four exponentials with lifetimes $\tau_1 = 3.612 \pm 0.028$, $\tau_2 = 1.171 \pm 0.027$, $\tau_3 = 0.128 \pm 0.0043$ and 0.018 ± 0.00024 ns with the relative contributions to the total intensity of 39.93, 18.62, 11.40, and 30.06%, respectively. In contrast to the decay of fluorescence on glass, the exponentials decaying with the slow lifetimes (τ_1 and τ_2) contributed only 58.55% of the total intensity. The remaining 41.45% was contributed by the fast decay (τ_3 and τ_4). The exponentials decaying with the slow and fast lifetimes contributed 1.51 and 98.49% of the total amplitude. The amplitude weighted average lifetime was 0.056 ns.

Decrease of photobleaching

Both a decrease in τ and an increase in Q lead to a significant decrease of photobleaching. As noted before, decrease in τ diminishes bleaching because the shorter the excited state, the smaller the opportunity of free oxygen to damage the fluorophore, while the increase in Q diminishes bleaching because it allows a decrease of the exciting light intensity needed to maintain the same signal intensity. The overall decrease in photobleaching results from combination of these two factors and is shown in Fig. 13. The thickness of the evanescent wave (~200 nm) and the projection of the confocal aperture on the image plane (50 $\mu\text{m}/60$

magnification of the objective = $\sim 0.9 \mu\text{m}$) defined the confocal volume as 150–200 attoL. This is comparable to the volume of half-sarcomere. The glass and SIF signals decayed with the rates of 3.22×10^{-2} and $1.65 \times 10^{-2} \text{ s}^{-1}$, respectively. In 12 separate experiments, the average rate for myofibrils on glass and on glass coated with SIF was $0.0239 \pm 0.0008 \text{ s}$ and $0.0131 \pm 0.0012 \text{ s}^{-1}$ (mean \pm SE; estimated by Mathematica 5.2) respectively, showing that photobleaching on glass is slowed by SIF on average 1.8-fold.

Particles of silver in SIF display curious “blinking,” even in the absence of the fluorophore (72). Fortunately, blinking is rare. In the area defined by the projection of the $50 \mu\text{m}$ confocal aperture, we have detected on average only three or four events during 100 s.

Decrease of bleaching in single molecule detection experiments

In SMD measurement on muscle, we used a high-aperture (NA = 1.65) high-magnification objective and $4 \mu\text{m}$ confocal aperture. This decreases the depth of the detection volume (equal to the depth of the evanescent wave) to $\sim 65 \text{ nm}$. The X-Y dimension of the detection volume is equal to the diameter of the confocal aperture divided by the magnification of the objective. With a $4 \mu\text{m}$ aperture and 100X objective it is equal to the diffraction limit of NA 1.65 objective = $\sim 0.25 \mu\text{m}$ giving the detection volume of $12 \times 10^{-18} \text{ L}$ (19). Actin concentration in muscle (0.6 mM) implies that there are ~ 4500 actin protomers in this volume. The ratio of fluorescent phalloidin to nonfluorescent phalloidin was fixed at 1:1000, suggesting that the signal was contributed by about four or five actin molecules.

The high NA objective requires the use of high-refractive-index cover slips. We compared photobleaching on sapphire and on sapphire coated with SIF. The top panel of Fig. 14 illustrates how signal from a myofibril was measured. The O-band was positioned over the

projection of the confocal aperture on the image plane by maneuvering the myofibril by X-Y piezo stage as described in (19). The bottom panel compares photobleaching of the O-band of myofibrils on sapphire (green) and on sapphire coated with SIF (red) as seen through the confocal aperture illustrated in the top panel. The signal is weaker and more noise is present because 4-5 rather than hundreds of molecules were observed. It takes longer to obtain SIF signal than sapphire signal, because the SIF alters the TIRF angle and it takes a few minutes to find the proper SIF-TIRF angle. Photobleaching during this extra time is responsible for the fact that the SIF signal is not enhanced over sapphire signal. In six separate experiments, the average rate for myofibrils on sapphire and on sapphire coated with SIF was 0.0191 ± 0.0012 s and 0.0025 ± 0.0012 s⁻¹ (mean \pm SE), respectively, showing that photobleaching on sapphire is slowed down by SIF on average 7.5-fold.

We observed that the suppression of bleaching was more effective on Olympus cover slips than on pure sapphire. Fig. 15A compares a typical time course of signal from the overlap zone of myofibrils on Olympus coverslip (green) and Olympus coverslip coated with SIF. Fig. 15B shows the same signals on an expanded time scale. In six separate experiments, the average rate for myofibrils on Olympus cover slips and on Olympus cover slips coated with SIF was 0.0432 ± 0.0052 s and 0.0013 ± 0.0009 s⁻¹ (mean \pm SE), respectively, showing that photobleaching on Olympus cover slips is slowed down by SIF by more than 30-fold. In two experiments, we observed no decay of SIF signal at all during 100 s.

FIGURES

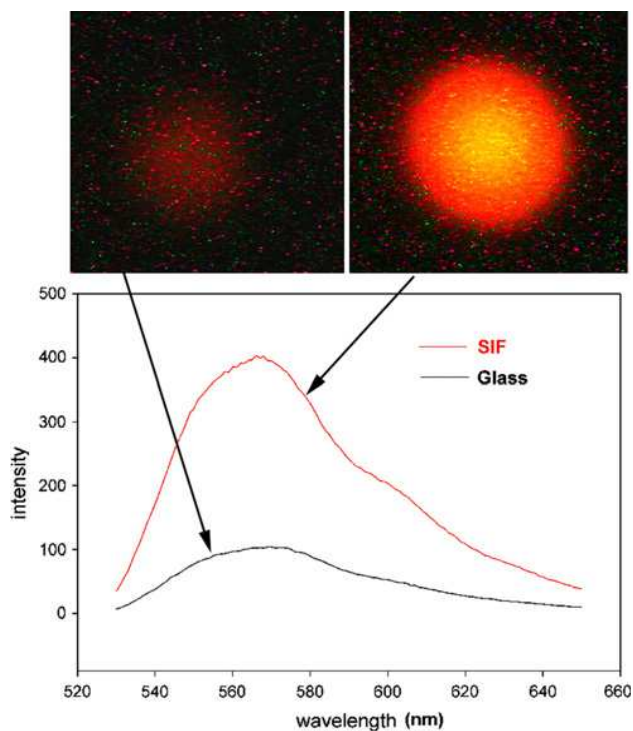


Fig. 9. Enhancement of fluorescence by SIF. Myofibrils (1 mg/mL) labeled with 0.1 μ M Rh-phalloidin were placed on a glass coverslip (top left) and on a coverslip coated with SIF (top right). The spectra were measured at a 45° angle in a Varian Eclipse spectrofluorometer. The vertical scale is in arbitrary units (a.u.). The spectrum of SIF in the absence of muscle is less than 10 a.u. at all wavelengths.

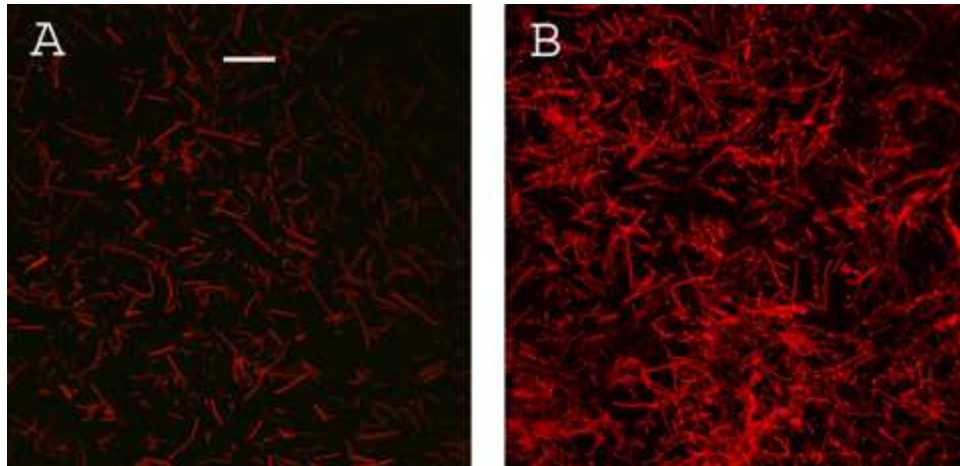


Fig.10. Confocal image of myofibrils contributing to fluorescence. (A) – myofibrils on glass coverslip; (B) – myofibrils on glass covered with SIF. Bar is 10 μm . Exposure is the same in each panel.

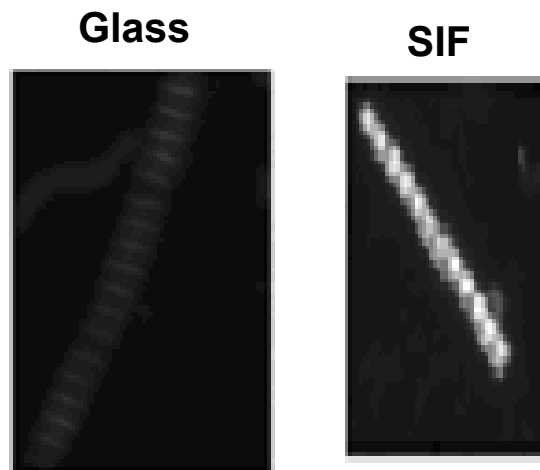


Fig. 11. Enhancement of fluorescence by SIF using TIR fluorescence. Myofibrils were placed on glass coverslip (left column) or on glass cover slips coated with SIF and detected by TIRF. The representative images, from the faintest to the most intense, are shown. Exposure times and camera gain are the same for each panel.

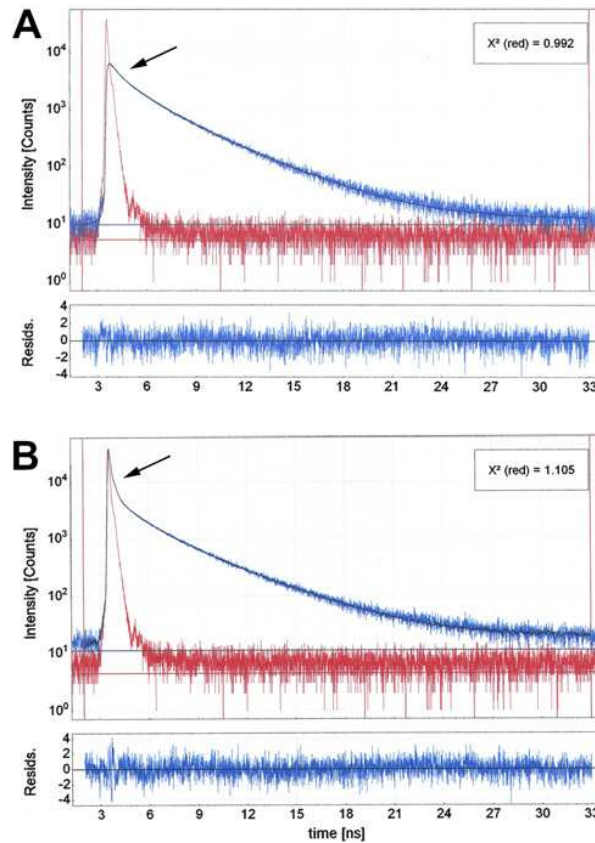


Fig. 12. Comparison of lifetime signals from myofibrils on glass (A) and on SIF (B). The solid line in (A) is best fitted by three exponentials with lifetimes $\tau^1 = 3.607$, $\tau^2 = 1.486$; and $\tau^3 = 0.254$ ns and relative contributions to the total intensity of 51.93, 38.35, and 9.72%, respectively. The bottom panel is the residual to the fit to all 4129 data points analyzed. The solid line in (B) is best fitted by four exponentials with lifetimes $\tau^1 = 3.612$, $\tau^2 = 1.171$, $\tau^3 = 0.128$ and $\tau^4 = 0.018$ ns and the relative contributions to the total intensity of 39.93, 18.62, 11.40, and 30.06%, respectively. The exponentials decaying with the slow lifetimes (τ^1 and τ^2) contributed 58.55% of the total intensity. The remaining 41.45% was contributed by the fast decay (τ^3 and τ^4). The bottom panel is the residual to the fit. All 4037 data points analyzed. The red signal is the excitation diode profile. The arrows point to a fast decay component.

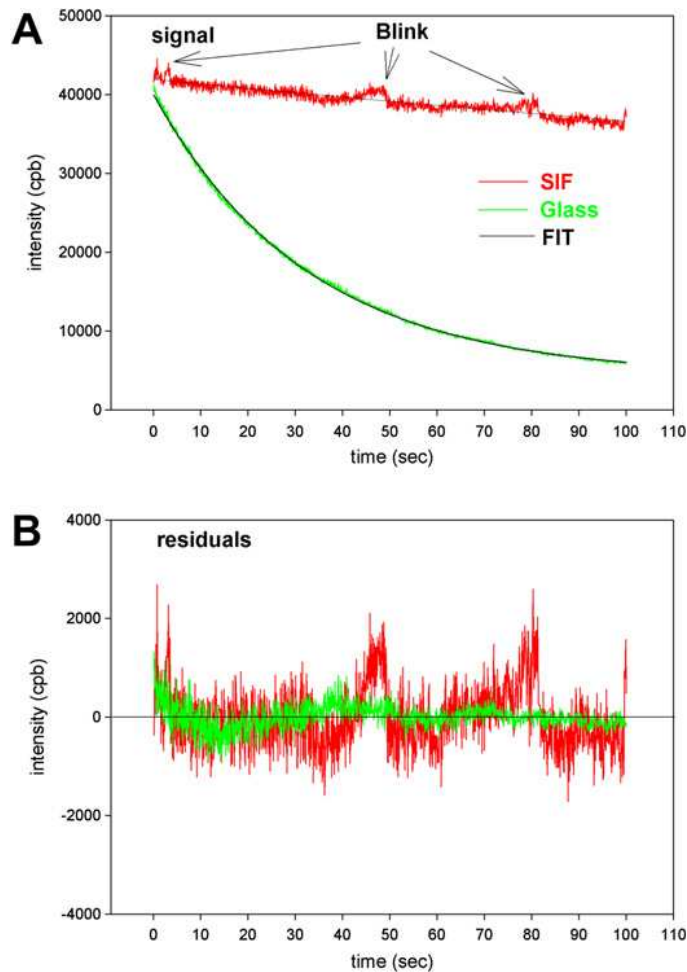


Fig. 13. Comparison of the rate of photobleaching of the myofibrillar overlap zone on uncoated glass (green) and on the on glass coated with SIF (red) (A). Myofibrils (1 mg/mL) were labeled with 0.01 μM Rh-phalloidin + 9.99 μM unlabeled phalloidin. The overlap zone of a myofibril was viewed in TIRF mode by SMD microscope through a 50 μm confocal aperture. The glass and SIF signals decayed with the rates of 3.22×10^{-2} and $1.65 \times 10^{-2} \text{ s}^{-1}$, respectively. The intensities at time = 0 were equalized by attenuating illumination of the myofibrils on SIF with 0.9 O.D neutral density filter. Arrows point to the increase of fluorescence caused by blinking. NA=1.45 objective. The lower panel shows the blinking effect on an expanded scale (B). CPB is counts-per-100 ms bin.

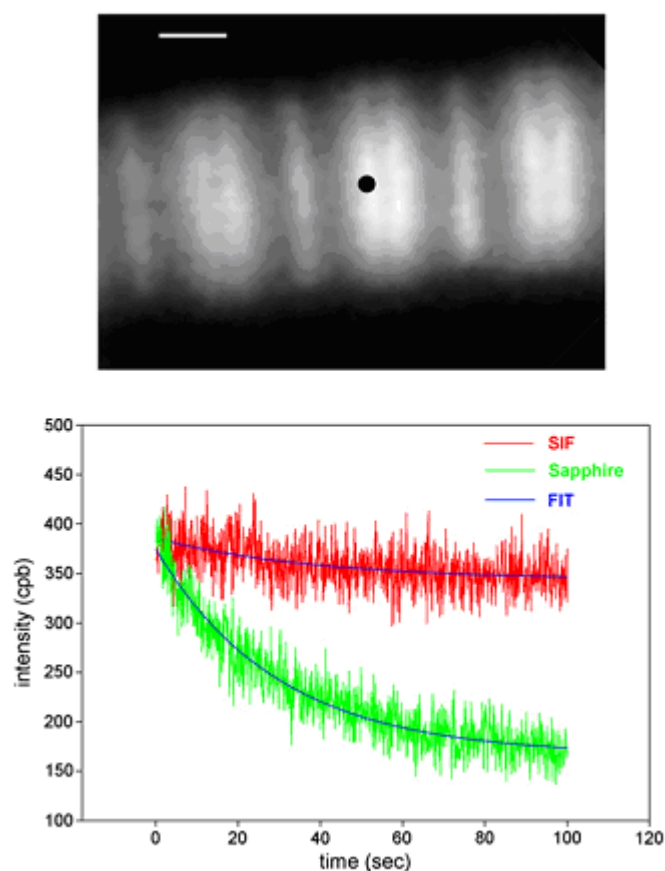


Fig. 14. Comparison of the rate of photobleaching of the myofibrillar overlap zone on uncoated sapphire (green) and on sapphire coated with SIF (red). Myofibrils (1 mg/mL) were labeled with 0.01 μM Rh-phalloidin + 9.99 μM unlabeled phalloidin. The overlap zone of a myofibril was viewed in TIRF mode by SMD microscope through a 4- μm confocal aperture, whose projection (black dot) on the image plane is shown in the top panel. The bar is 1 μm . The three parameter exponential fits are in blue. NA = 1.65 objective. CPB is counts-per-100 ms bin.

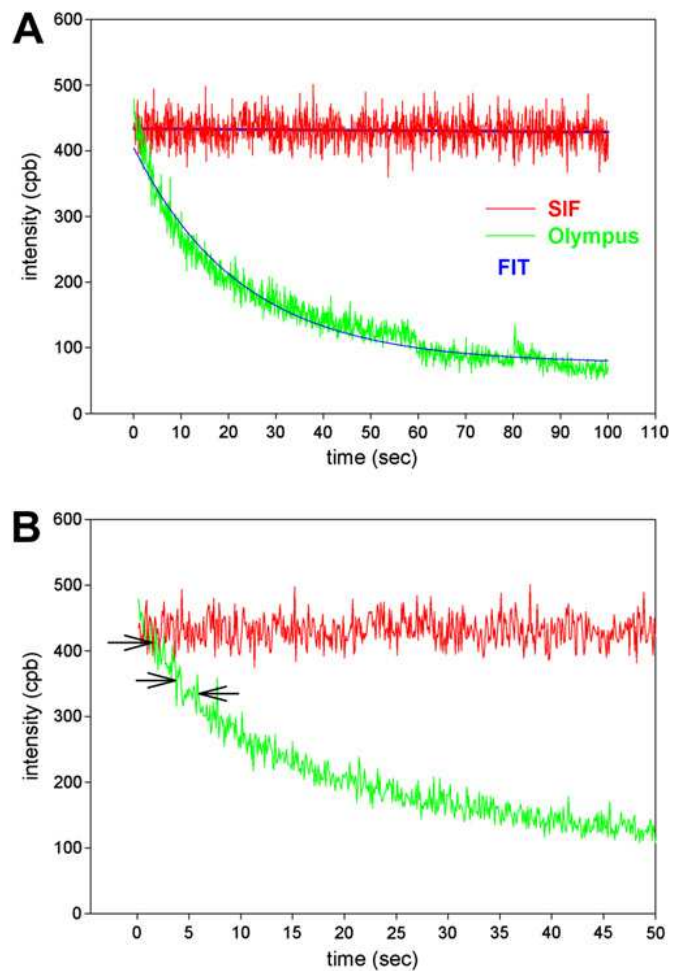


Fig. 15. Comparison of the photobleaching of myofibrillar overlap zone on uncoated Olympus TIRF cover slips (green) and on Olympus TIRF cover slips coated with SIF (red) (A). B shows the same on an expanded scale. Arrows point to possible photobleaching events.

Discussion

The observed increase of brightness can be caused by the (i) increase of rhodamine quantum yield, (ii) the decrease in self-quenching (42), or (iii) the enhancement of the local electromagnetic field (60).

Quantum yield: The quantum yield of rhodamine on SIF substrate cannot exceed 1. On glass it equals 0.7, so the maximum increase of quantum yield caused by SIF cannot exceed 43%. This increase must be caused by increase in the radiative rate, as evidenced by the fact that silver islands significantly decreased fluorescence lifetime: the amplitude weighted fluorescence lifetime of myofibrils on SIF decreased on average 22.7 fold in comparison with lifetime of myofibrils on glass. That SIF has dramatic effect on the lifetime is best illustrated by the relative contributions of slow and fast decays: The transition from glass to SIF decreased contribution to the total fluorescence intensity of the slow-decaying components by a third (from ~90 to ~59%). The same transition increased contribution of the fast-decaying components four times (from ~10 to ~41%). The effect on decay of fluorescence amplitude was even more dramatic. The transition from glass to SIF decreased contribution to the total fluorescence amplitude of the slow-decaying components ~50-fold (from ~51 to ~1%). The same transition increased contribution of the fast-decaying components 2 fold (from ~49 to ~98%). There was no picosecond decay of fluorescence of myofibrils on glass, whereas it contributed nearly a third of the total intensity on SIF.

Quenching: It is obvious that self-quenching plays no role in our experiments, because rhodamine molecules are separated by a distance of at least 30 nm (7).

Enhancement of local field: The bulk of the increase must be due to the enhancement of the local field. This increase occurs despite the fact that silver islands may locally quench fluorescence at

a close proximity (<5 nm) to the fluorophore (63, 45). The increase of brightness was not caused by the increase of the number of fluorophores bound to the silver film because this number was fixed by taking measurements only from the myofibrils.

The ability of SIF to decrease photobleaching should make SMD measurements on muscle possible. Photobleaching complicates measurements because interesting changes due to the mechanical activity of myosin cross bridges are superimposed on changes due to bleaching. The fact that SIF decreased the rate of photobleaching on Olympus cover slips more than 30-fold will make SMD measurements of myofibrils on high refractive-index substrates particularly attractive. It is not clear to us why Olympus cover slips are better than sapphire slips. Olympus would not reveal the composition of their material.

We have shown earlier that surface plasmon coupled emission (SPCE) leads to the enhancement of excitation because of the increase in the local field at the metal–buffer interface (19). The present work demonstrates that SIF leads to an enhancement of emission. Combination of SPCE and SIF should result in enhancement of both excitation and emission.

c) Nanoparticles of silver monolayers (NML)

Introduction

In the earlier work, we were able to decrease photobleaching by making measurements on cover glasses coated with nanoparticles known as surface island films (SIF). As a consequence of SIF-induced field enhancement and decrease of lifetime, the rate of photobleaching of rhodamine-phalloidin-labeled actin in a myofibril placed on glass coverslips coated with SIF decreased approximately twofold in comparison with that of myofibrils placed on uncoated coverslips (69). The price of the reduction in bleaching, however, was a loss of

optical resolution and loss of nonuniformity of illumination, because SIF refracted the exciting and fluorescent light, and because nanoparticles were distributed randomly on the surface of a coverslip. This is a severe disadvantage of the use of SIF in SMD, because maximal optical resolution is important in resolving single molecules. Optimal resolution allows accurate definition of the region of interest (ROI) within a cell, a requirement crucial for determining a function of a specific sub cellular organelle. For example, in studying the function of skeletal muscle myofibrils, it is important to place the ROI exactly at the area where actin and myosin filaments interact to produce contractile force (19). This area, known as the overlap zone, spans a distance of 0.7–0.3 μm in resting-length myofibrils, and its length is comparable to the maximal resolution of an optical microscope (43).

Results

AFM and SEM images of NML surfaces.

Fig. 16 shows representative SEM images of a small, mixed, and large-sized NML deposited on glass. The median diameters were 60 ± 21 , 50 ± 10 , and 71 ± 0.20 nm (median \pm SD), respectively. The average ratios of diameters in the xy plane for small, mixed, and large nanoparticles were 1.1 ± 0.2 , 0.8 ± 0.08 , and 1.3 ± 0.4 , respectively. Fig. 2 shows representative AFM images of small, mixed and large NMLs deposited on glass. The average heights of small, mixed, and large NMLs were 40 ± 6 nm, 42 ± 9 nm, and 74 ± 10 nm (mean \pm SD), respectively. The average axial ratios of small, mixed, and large NMLs were 1.5, 1.2, and 0.9, respectively. The thickness of myofibrils was estimated from AFM images by measuring the distance from the cover glass to the highest point of elevation of the O-band (Fig.17). In 12 measurements on

phalloidin-labeled myofibrils, the average height of a myofibril was 97 ± 4 nm and the average width was 1.68 ± 0.22 μ m (mean \pm SEM).

Quality of images

Fig. 18 shows representative examples of myofibrils on glass. The images are of good quality, as evidenced by the fact that the Z-bands (arrowheads) and the H-zones (arrows) are well resolved. Myofibrils are particularly favorable objects for testing optical resolution, because the widths of Z-lines and H-zones are ~ 0.25 μ m, approximately equal to the optical resolution of the NA 1.45 objective using green light. Fig. 19 shows representative examples of myofibrils on mixed NMLs. Fig. 20 (magnification of Fig. 19, lower right) shows that the resolution of the Z-bands (arrowheads) and the H-zones (arrows) is as good as that for myofibrils on glass. The intensity is larger in Fig. 19 than in Fig. 18, consistent with the fact that colloids increase brightness (see below).

Increase of brightness

Bulk measurements:

The diameter of the excitation beam was ~ 1 mm and the thickness of the sample was ~ 100 nm, giving a detection volume of $\sim 10^{-10}$ L. For myofibrils labeled with 0.1 μ M fluorescent phalloidin 9.9 μ M nonfluorescent phalloidin, this means we observed $\sim 10^6$ – 10^7 molecules of the dye. Fig. 21.A compares emission spectra of myofibrils on glass cover slips coated with NML with spectra of myofibrils on plain glass. No differences in the emission spectra were detected. Fig. 21 B compares peak intensities of myofibrils labeled with Rh- (left) or Fl-phalloidin (right). The peak fluorescence intensity of Rh-phalloidin-labeled myofibrils on small- and large-NML-

coated cover slips was enhanced ~7 and 13 times, respectively, compared with that on plain glass cover slips. The peak fluorescence intensity of Fl-phalloidin labeled myofibrils on small and large NML coated cover slips was, respectively, 18 and 33 times that on plain glass cover slips (Table 1).

Table 1: Effect of NML on enhancement of fluorescence

		Intensity (Fold over glass)	
		Rhodamine	Fluorescein
Bulk	Glass	1	1
	Mixed	-	-
	Small	7	18
	Large	13	33
SMD	Glass	1	-
	Mixed	84±18	-
	Small	540±81	-

SMD measurements

Because the myofibril is <100 nm thick, it makes no difference as far as the number of excited molecules are concerned, whether SMD experiments are carried out using transmitted or TIRF illumination. The signal from a myofibril was measured by positioning the O-band over the projection of the confocal aperture on the sample plane, as described in Borejdo et al (19). The focused laser spot was previously positioned over this projection. The detection volume is $\Pi \times (D/2)^2 \times H$, where H is the average thickness of a myofibril. The average thickness was ~100 nm. The detection volume was $\sim 20 \times 10^{-18}$ L. Actin concentration in muscle (0.6 mM) implies

that there were ~ 7200 actin protomers in this volume. The ratio of fluorescent phalloidin to nonfluorescent phalloidin was fixed at 1:1000, suggesting that the signal was contributed by, on average, seven to eight actin molecules. In five experiments, enhancements were 84 ± 18 and 540 ± 81 for mixed and small colloids, respectively (Table 1).

Decrease of fluorescence lifetime

Bulk measurements (Myofibrils were labeled with fluorescein-phalloidin)

Glass: The decay of fluorescence of myofibrils on glass (Fig. 22 A) was best fitted by two exponentials with lifetimes $\Gamma_1=3.596$ and $\Gamma_2=1.420$ ns with the relative contributions to the total amplitude of 55.3% and 44.7%, respectively. The amplitude weighted average lifetime was 2.498 ns.

Mixed NML: The decay on mixed NML was considerably different (Fig. 22 B). The decay of fluorescein was now best fitted by three exponentials with lifetimes $\Gamma_1=3.396$ ns, $\Gamma_2=1.420$ ns, and $\Gamma_3=0.146$ ns, with relative contributions to the total amplitude of 13.5%, 16.3%, and 70.2%, respectively. The amplitude-weighted average lifetime decreased to 0.791 ns. Thus, the application of NML caused the appearance of an ultra short component contributing $>70\%$ to the signal amplitude, and caused the amplitude-weighted average lifetime to decrease more than threefold.

Small NML. Fig. 23 A shows that the addition of small NML caused the fluorescence lifetime to decrease. The lifetime signal from myofibrils on small NML was best fitted by three exponentials with lifetimes $\Gamma_1=3.448$ ns, $\Gamma_2=1.225$ ns, and $\Gamma_3=0.168$ ns, with relative contributions of 18.5%, 21.5%, and 60.0%, respectively, to the total amplitude. The amplitude-weighted average lifetime was 1.006 ns. Thus, the application of small NML caused the

appearance of an ultra short component contributing >60% to the signal amplitude, and caused amplitude-weighted average lifetime to decrease more than twofold.

Large NML. Addition of large NML (Fig. 23 B) augmented the fast decay of fluorescein-labeled myofibrils even more (arrow). The decay was best fit now by four exponentials with lifetimes $\Gamma_1=3.983$ ns, $\Gamma_2=1.787$ ns, $\Gamma_3=0.256$ ns, and $\Gamma_4=0.014$ ns, with relative contributions of 0.4%, 0.8%, 1.7%, and 97.1%, respectively, to the total amplitude. The amplitude-weighted average lifetime decreased to 0.048 ns. The application of large NML caused the appearance of an ultra short component contributing >97% to the signal amplitude, and caused the amplitude-weighted average lifetime to decrease >48-fold. Lifetime data is summarized in Table 2.

Table 2: Effect of NML on lifetime

		Lifetime(ns)	SD	%Contribution
Bulk	Glass	3.596	0.038	55.3
		1.138	0.050	44.7
	Mixed	3.396	0.024	13.5
		1.420	0.028	16.3
	Small	0.146	0.005	70.2
		3.448	0.095	18.5
	Large	1.225	0.061	21.5
		0.168	0.020	60.0
	Large	3.983	0.063	0.4
		1.787	0.018	0.8
		0.256	0.013	1.7
		0.014	0.002	97.1

Standard deviations from 67% confidence intervals were determined by FluoFit software.

To fit the data accurately in the presence of the monolayer of silver nanoparticles, it was necessary to use a more complex decay model (three exponents for mixed and small NMLs and four exponents for large NMLs). In these decays, the contributions of short-lived components were very high, the biggest being for large NML (97%). It is often a difficult task to resolve such short components, especially when their contribution to the total decay is weak. However, in the case of a very high contribution, the resolution is much more reliable, as can be seen in Table 2 (SD column).

SMD measurements

Lifetimes were only measured in the bulk. We do not yet have the ability to measure lifetimes with a microscope.

Decrease of photobleaching

As in the case of the increase of brightness, the decrease of photobleaching was different in bulk and SMD measurements.

Bulk measurements

Fig. 24 shows the decay of fluorescence in a bulk sample. The sample was positioned in front-face configuration inside the fluorometer chamber. Excitation was at 475 nm and observation was through a monochromator at 575 nm. Time 0 was after exposing the sample to the laser light for 10 s. Consecutive readings were taken every 60 s for a total of 1000 s. The

half-time of photobleaching for the sample on glass was ~ 300 s, and that for the sample on small and large NMLs was ≥ 2000 s.

SMD measurements

Fig. 25 compares the rate of photobleaching of the myofibrillar overlap zone on glass and on cover slips coated with NML. Small NML is shown as an example. The signal from the myofibril (light gray) was enhanced 90-fold compared with the signal on glass (gray). The average halftime of decay was at least 200 s. We were unable to determine exactly the rate of photobleaching, because it depended critically on the choice of baseline: the lower the baseline, the slower the decay. For example, if the baseline in Fig. 25 was chosen to be 10,000, the rate for NML was approximately equal to the rate for glass. The average halftimes for mixed and large colloids were 56 ± 22 s and 69 ± 25 s (Table 3).

Table 3: Effect of NML on half-times of bleaching

Half-time of bleaching (s)		
Bulk	Glass	300
	Mixed	-
	Small	At least 200
	Large	At least 200
SMD	Glass	11 ± 4
	Mixed	56 ± 22
	Small	At least 200
	Large	69 ± 25

Bulk measurements were done on 1 mg/mL myofibrils labeled with 10 nM fluorescein-phalloidin + 10 μ M unlabeled phalloidin. SMD measurements were done on 1 mg/mL myofibrils labeled with 10 nM Rhodamine phalloidin + 10 μ M unlabeled phalloidin.

FIGURES:

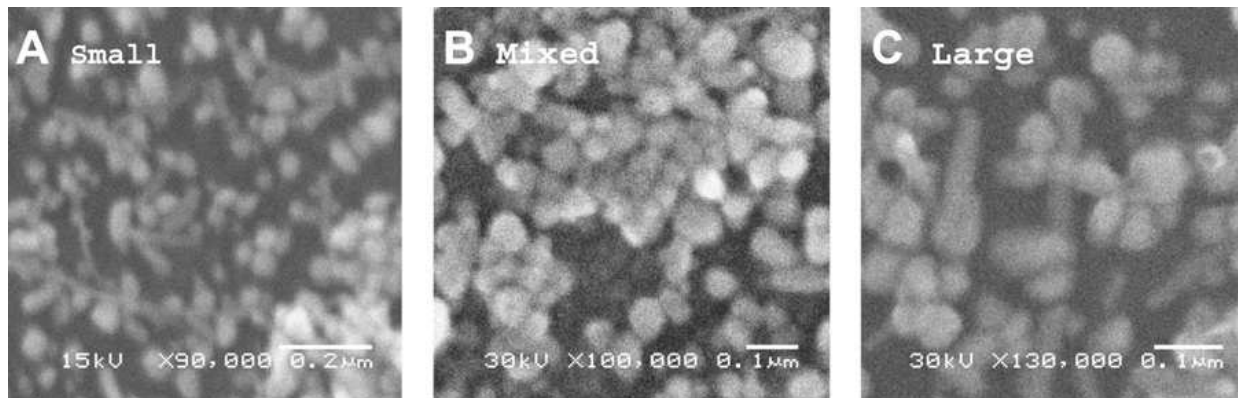


Fig. 16: SEM Images. NML surfaces with median diameters of 60, 50, and 70 nm, respectively, for small- (A), mixed- (B), and large-sized (C) particles.

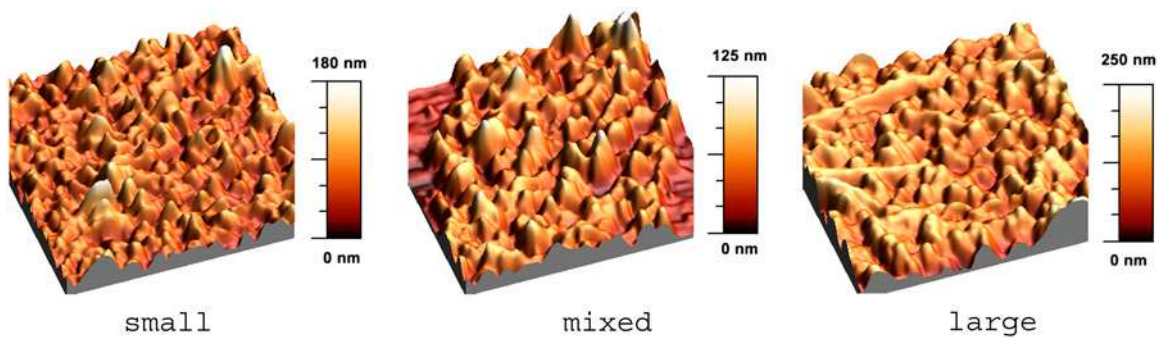


Fig. 17: AFM images of the NML surface. All images are $2.5 \times 2.5 \mu\text{m}$.

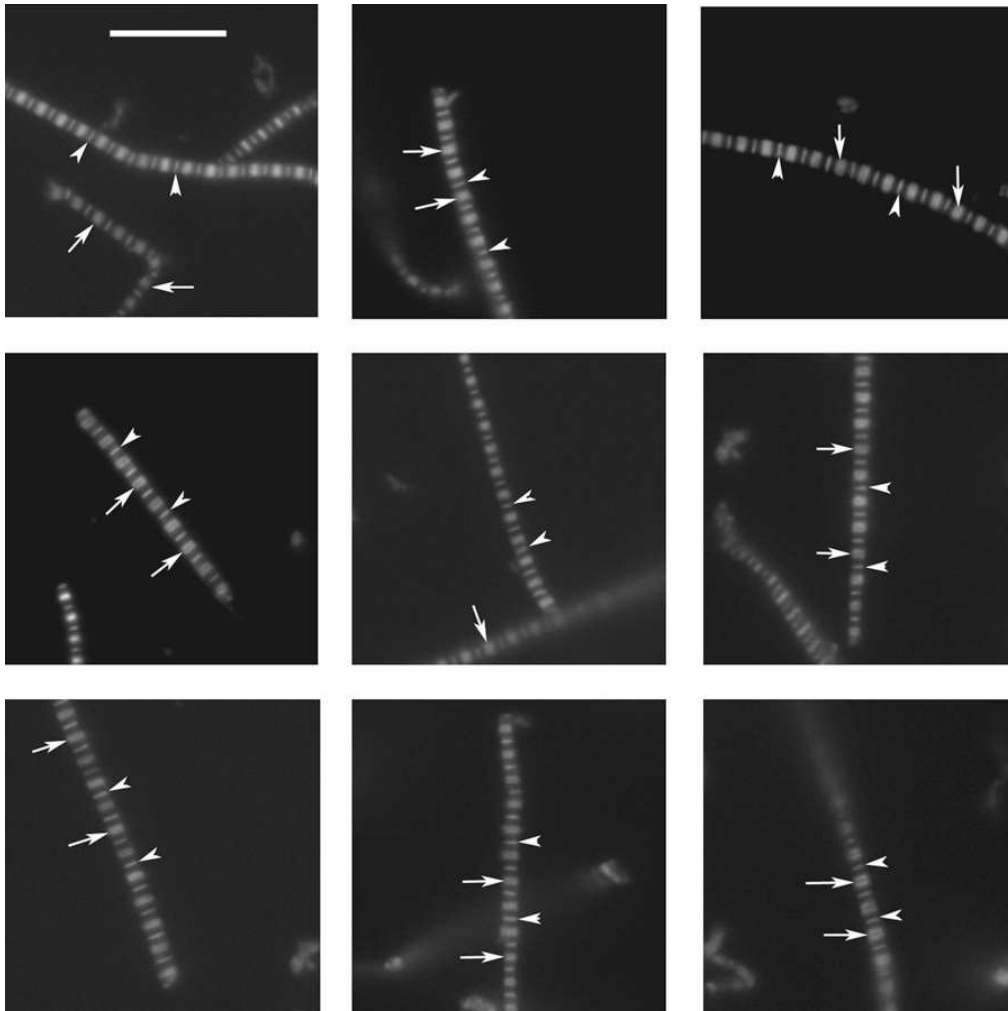


Fig. 18: Representative images of myofibrils on glass. Arrowheads point to the Z-lines and arrows point to the H-zones. Myofibrils were labeled with 0.1 μM rhodamine phalloidin + 9.9 μM unlabeled phalloidin. Scale bar, 10 μm . TIRF excitation.

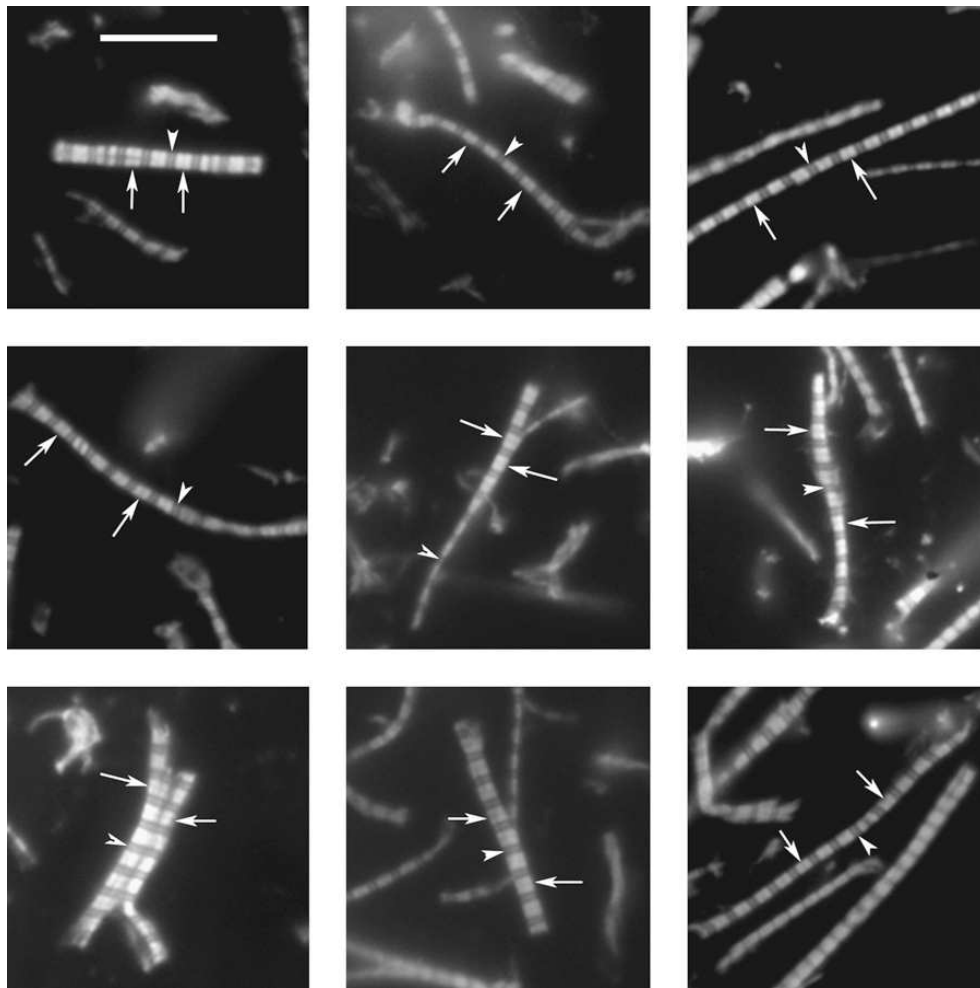


Fig. 19: Demonstration that the quality of images is not degraded by the presence of colloid. The quality of images is as good as in the absence of colloid (Fig. 3). Arrowheads point to the Z-lines and arrows point to the H-zones. Myofibrils were labeled with 0.1 μM rhodamine phalloidin + 9.9 μM unlabeled phalloidin. Scale bar, 10 μm . TIRF excitation.

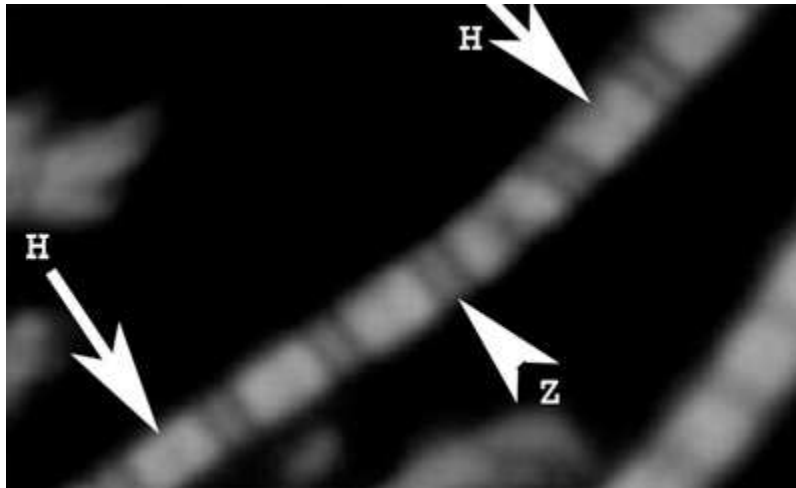


Fig. 20: Image of myofibrils on NML. The resolution is as good as on glass, as evidenced by the fact that both H-zones (arrows) and Z-lines (arrowhead) can be seen. TIRF excitation.

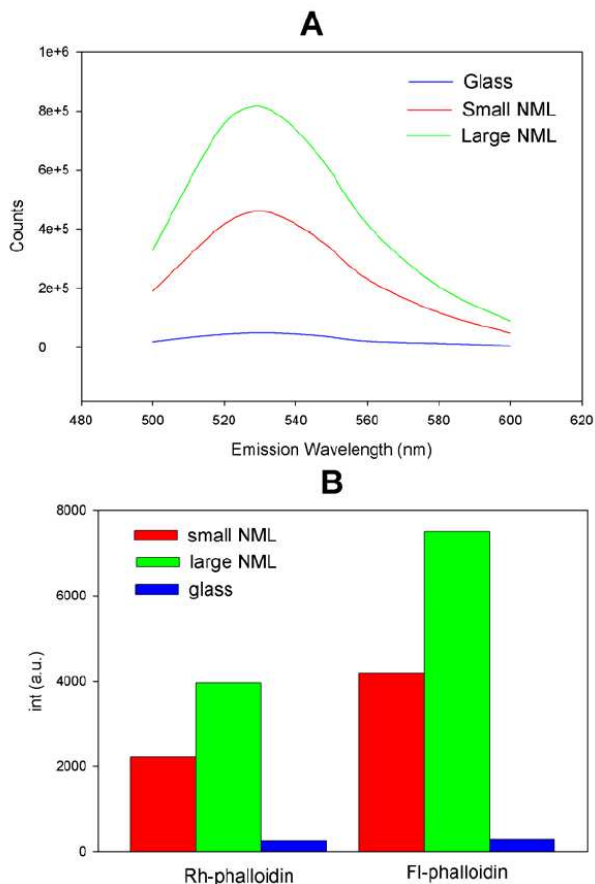


Fig. 21: Enhancement of fluorescence by colloid monolayers. (A) Spectra of myofibrils (1 mg/mL labeled with 0.1 μ M fluorescein-phalloidin) on glass coverslip coated with monolayers containing large (green) and small (red) colloids. Spectra were measured at a 45° angle in a Varian Eclipse spectrofluorometer. Excitation wavelength was 475 nm. The spectrum of glass alone is in blue. The spectrum of colloid monolayer in the absence of muscle was comparable to glass alone. (B) Fluorescence intensities of myofibrils (1 mg/mL) labeled with 0.1 mM rhodamine-phalloidin (left) and 0.1 mM fluorescein-phalloidin (right). Myofibrils were on glass (blue) cover slips or on glass coated with monolayers containing large (green) and small (red) colloids. The intensities were measured at an orthogonal excitation, at 560 nm (left) and 530 nm (right) in a Varian Eclipse spectrofluorometer. Excitation wavelength was 475 nm.

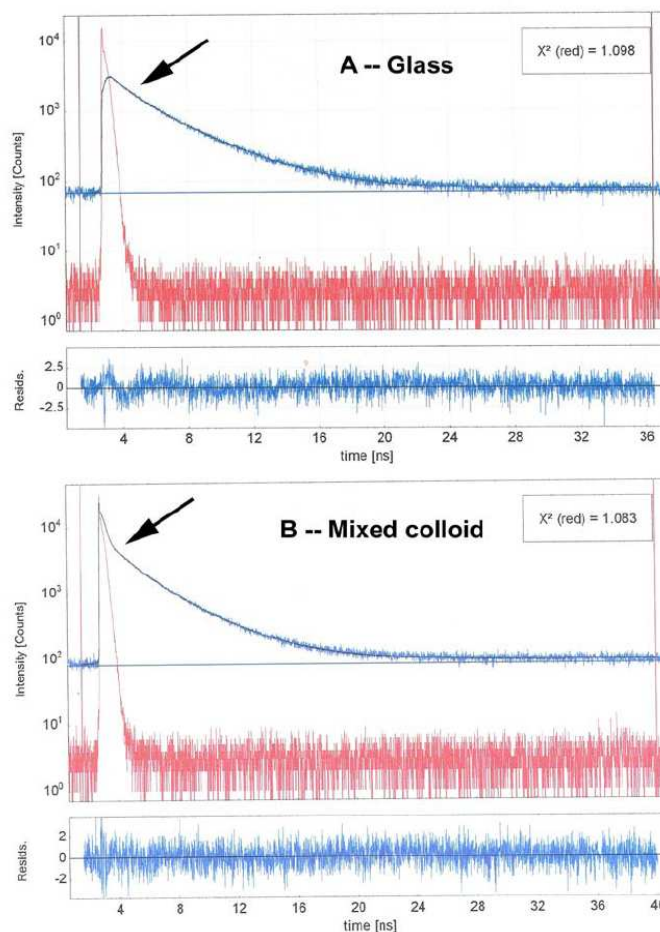


Fig. 22: Decrease of fluorescence lifetime by mixed-size NML. (A) Lifetime signal from myofibrils on glass (blue). The signal is best fitted (black line) by the two exponentials with lifetimes $\tau_1=3.596$ and $\tau_2=1.138$ ns, with relative contributions to the total amplitude of 55.3% and 44.7%, respectively. The red signal is the exciting pulse from the diode laser. The bottom panel shows the residual fit to all 8767 data points. (B) Lifetime signal from myofibrils on glass coated with a mixed-size SIF monolayer (blue) is best fitted (black line) by three exponentials with lifetimes $\tau_1=3.396$ ns, $\tau_2=0.1420$ ns, and $\tau_3=0.146$ ns, with relative contributions to the total amplitude of 13.5%, 16.3%, and 70.2%, respectively. The arrows point to the fast decay of fluorescence. The red signal is the exciting pulse. The bottom panel shows the residual fit to all 9604 data points. The 1 mg/mL myofibrils were labeled with 0.1 μ M fluorescein-phalloidin.

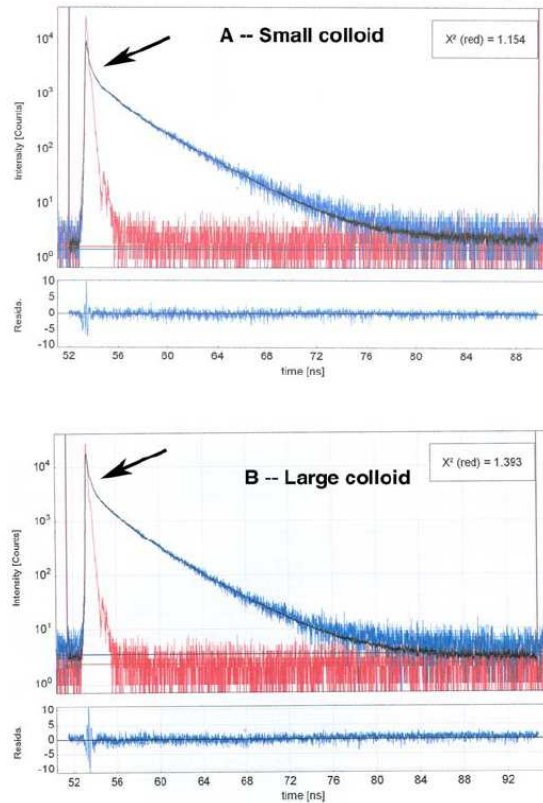


Fig. 23: Decrease of fluorescence lifetime by small and large NML. (A) Lifetime signal from myofibrils on the small NML (blue). The signal is best fitted (black line) by three exponentials with lifetimes $\tau_1=3.448$ ns, $\tau_2=1.225$ ns, and $\tau_3=0.168$ ns, with relative contributions to the total amplitude of 18.5%, 21.5%, and 60.0%, respectively. The red signal is the exciting pulse from the diode laser. The bottom panel shows the residual fit to all 9445 data points. The arrow points to the fast decay of fluorescence. (B) Lifetime signal from myofibrils on the large NML (blue). It is best fitted (black line) by four exponentials with lifetimes $\tau_1=1.787$ ns, $\tau_2=0.256$ ns, $\tau_3=3.983$ ns, and $\tau_4=0.014$ ns, with relative contributions to the total amplitude of 0.8%, 1.7%, 0.4%, and 97.1%, respectively. The arrow points to the fast decay of fluorescence. The gray signal is the exciting pulse. The bottom panel shows the residual fit to all 10828 data points. Myofibrils labeled with 0.1 μ M fluorescein-phalloidin + 9.9 μ M unlabeled phalloidin. TIRF illumination was used on 1-mg/mL myofibrils labeled with 0.1 μ M fluorescein-phalloidin.

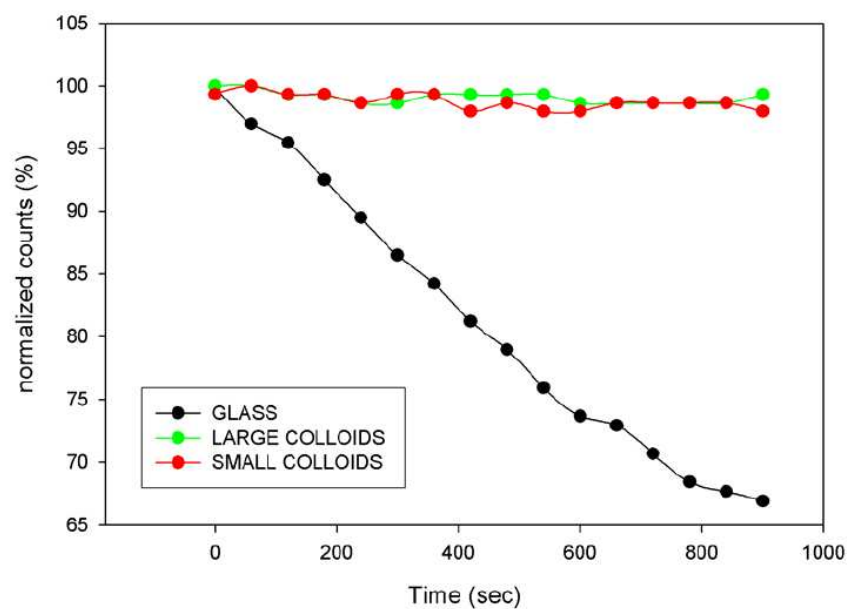


Fig. 24: Photobleaching of myofibrils in the bulk solution. The sample was positioned in front-face configuration inside the fluorometer chamber. λ_{exc} was 475 nm and λ_{em} was 575 nm. Time 0 is after exposing the sample to light for 10 s. Consecutive readings were taken every 60 s, for a total of 1000 s. The 1 mg/mL myofibrils were labeled with 0.1 μM fluorescein-phalloidin.

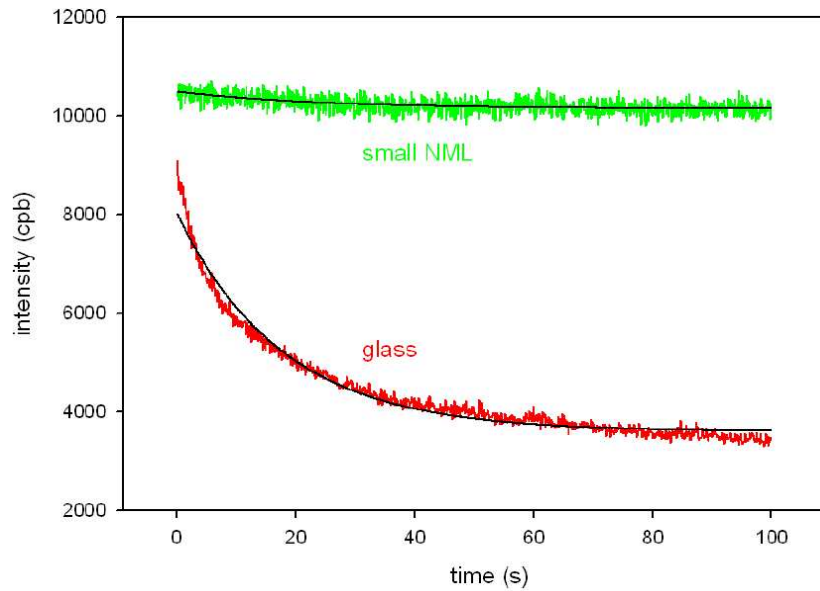


Fig. 25: Comparison of the rates of photobleaching of the myofibrillar overlap zone on small NML. Myofibrils (1 mg/mL) were labeled with 0.01 μM rhodamine-phalloidin + 9.99 μM unlabeled phalloidin. The overlap zone of a myofibril was viewed by SMD microscopy through an 8 μm confocal aperture. The three-parameter single-exponential fits for glass and NML are shown in black. NA=1.45 objective. CPB is counts-per-100 ms bin. **A)** Signal from myofibril on glass (red) and on small colloid (green). Colloid enhanced signal ~ 90 times. **B)** residuals of the 3 parameter exponential fit $3,596 + 4,449e^{-5.67e-3xt}$ for glass and $10,142 + 345e^{-4.25e-3xt}$ for NML. TIRF excitation.

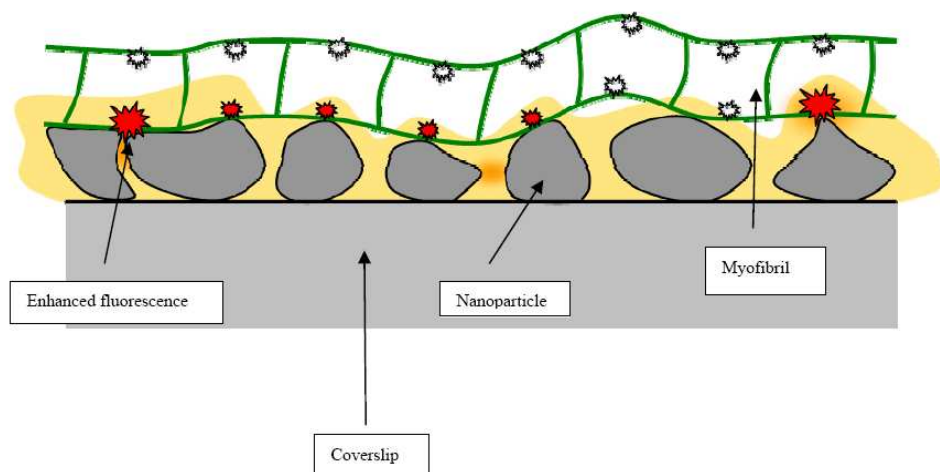


Fig. 26: Schematic diagram of a myofibril on a glass coverslip with NML-coated surface.

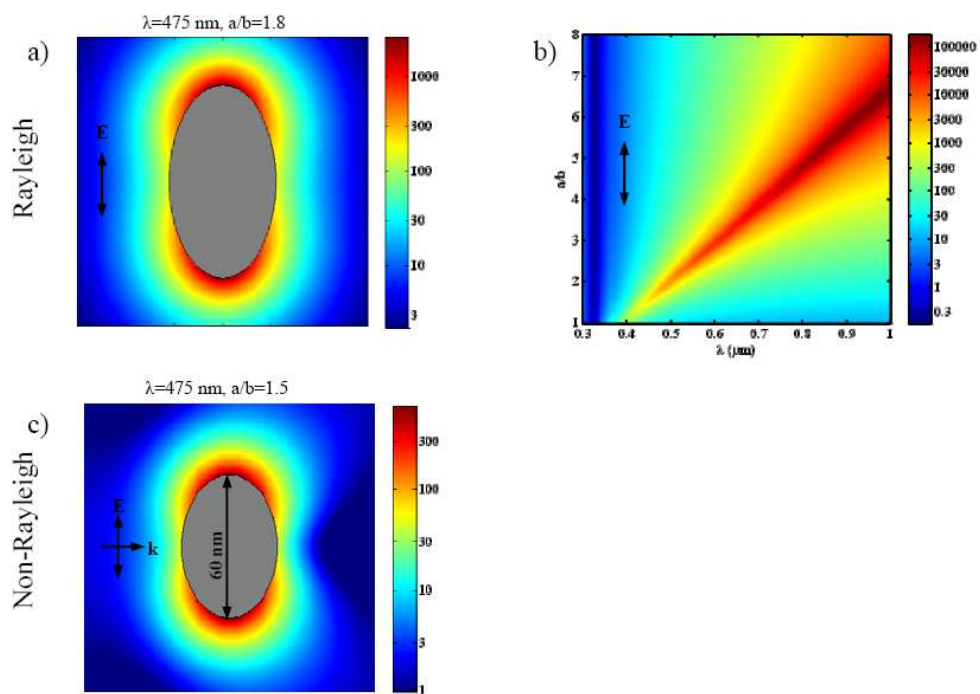


Fig. 27: Intensity enhancement of silver spheroid particles in water. (A) The intensity enhancement is in the Rayleigh limit, i.e., the particles are small compared to the wavelength. (B) The intensity enhancement at a spheroidal tip versus wavelength and axial ratio. (C) The intensity enhancement around a spheroid. The Rayleigh limit is not assumed. The calculations are exact using spheroidal wave functions.

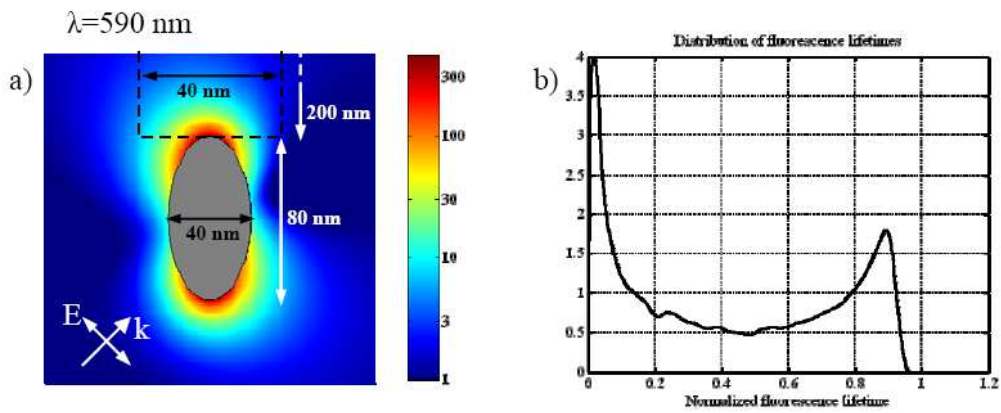


Fig. 28: Calculations to mimic the experimental setup, showing (A) the intensity enhancement, and (B) the distribution of lifetimes of fluorophores within the box.

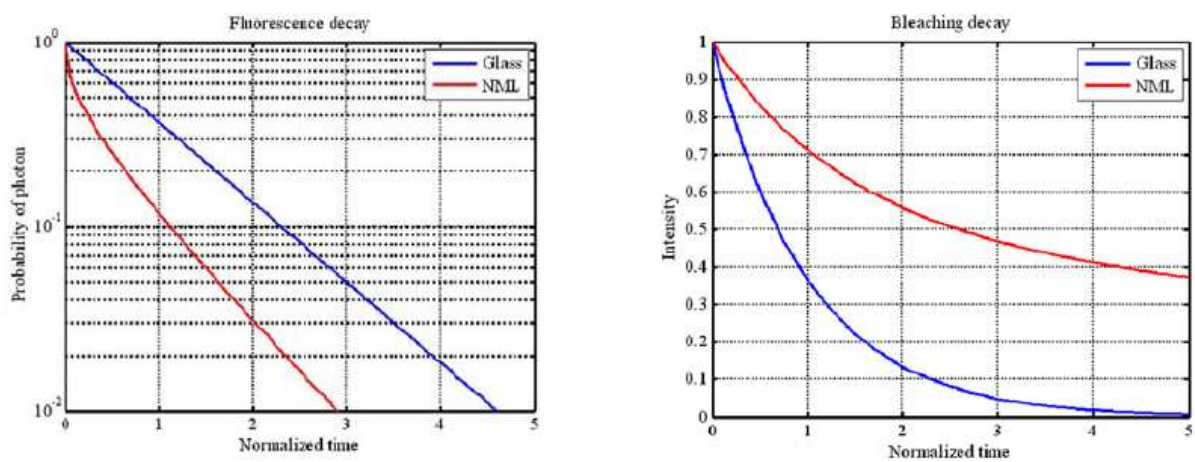


Fig. 29: The calculation of fluorescence (left) and bleaching (right) lifetimes using spheroidal wave functions at a couple of thousands points equally distributed within a box defined in Fig. 13.

DISCUSSION

The large enhancement of the excitation field made possible illumination with a weaker laser beam, which leads to a reduction of photodamage. The interactions between the LSPs and the fluorophores led to a significant increase of the spontaneous radiative rate of a fluorophore (58). Such enhancement is well known in surface plasmon resonance signals (71). The intensity enhancement around a spheroid is calculated analytically below assuming the Rayleigh limit. We also make accurate calculations (not assuming the Rayleigh limit) by the use of vector prolate spheroidal functions (30). Fig. 26 schematically illustrates the experimental arrangement. Nanoparticles and myofibrils are deposited on a glass coverslip. The Z-dimension of nanoparticles is comparable to the size of the myofibrils (69). We assume that nanoparticles are spheroid. The equation to be solved is

$$\nabla^2 V=0,$$

where V and $\epsilon(\delta V/\delta\alpha)$ are continuous at the spheroidal surface and $V \rightarrow Ez$ at infinity. E is the magnitude of the applied electric field and ϵ is the permittivity. Prolate spheroidal coordinates (α,β,Φ) are used:

$$x = f \sinh(\alpha)\sin(\beta)\cos(\varphi)$$

$$y = f \sinh(\alpha)\sin(\beta)\cos(\varphi)$$

$$z = f \cosh(\alpha)\sin(\beta)\cos(\varphi)$$

f is a parameter regulating the size of the spheroid, and the spheroidal surface is determined by the equation $\alpha = \alpha_0$ for some constant α_0 .

Solving the differential equation gives the analytic solution

$$V = Ef(\cosh(\alpha) + AQ_1(\cosh(\alpha)))\cos(\beta)$$

$$A = \frac{(\epsilon_i - \epsilon_o) \cosh(\alpha_o)}{\epsilon_i \cosh(\alpha_o) Q'_1(\cosh(\alpha_o)) - \epsilon_o Q_1(\cosh(\alpha_o))}$$

ϵ_i is the permittivity inside the spheroid (in this case, silver, and it is complex), and ϵ_o is the permittivity outside (in this case, water, with a value of 1.332). Q_l is a Legendre function of the second kind, and Q'_l is its derivative. Q_l is given by

$$Q_l(u) = \frac{u}{2} \ln \frac{(u+1)}{(u-1)} - 1$$

Fig. 27 shows the results of calculations of intensity enhancement of silver spheroids in water: the enhancement depends sharply on the values of axial ratio (a/b) and wavelength. In general, the enhancement increases with a/b and decreases with λ . Fig. 27 B shows that for $\lambda = 530$ nm and $a/b = 1.5$, the enhancement is ~ 1000 , in good agreement with the experiment (540-fold, Table 1). The fact that the enhancement was smallest for mixed particles (Table 1, SMD) is consistent with the theory, because large nanoparticles were the most symmetrical. Fig. 27 A shows that 1000-fold enhancement stretches at least to 10 nm beyond the limit of the nanoparticles, which is consistent with the idea that fluorophores nearest to the surface contribute the most to the enhancement (Fig. 26). The fact that enhancement in the bulk is smaller than in SMD may be due to the fact that the incident angle of the exciting wave is different in each case.

In the non-Rayleigh limit procedure, a series of vector spheroidal wave functions is used that is in principle similar to the Mie series for spheres, but more complicated. This case is described in Calander and Willander (30).

To calculate the influence of nanoparticles on the bulk fluorescence lifetime, we assume that the lifetime of a fluorophore is inversely proportional to the electromagnetic intensity enhancement, due to the reciprocity of energy flow. The intensity enhancement is calculated (by spheroidal wave functions) at a couple of thousand points equally distributed within a box at the

spheroid surface (40 x 40 x 200 nm, Fig.28.A). The enhancements at these points are used to calculate the distribution of lifetimes of fluorophores within the box (Fig. 28.B). It can be seen that, in agreement with experiment, the short lifetime is now the most prominent. The overall combined fluorescence intensity enhancement is 2.6 (assuming the same enhancement for emission and excitation), consistent with a small intensity enhancement observed in bulk (Table 1). At very strong field enhancements, one may speculate that resonance fluorescence may occur, making emission and excitation combine to give higher fluorescence intensity enhancement (up to a limit of 94.9 in this case). The very high enhancement found experimentally in some cases may be due to this. One may also speculate that dipole-dipole interactions between the LSPs further increase the enhancement (9).

Fig. 29 shows the calculations of fluorescence (left) and bleaching (right) lifetimes using the above-described methods. The bleaching is inversely proportional to the time spent in the excited state, i.e., the fluorescence lifetime. Fig. 29 left clearly shows the appearance of a short lifetime component due to the increase in radiative rate. Experimentally, the effect was most dramatic when the relative contributions of the slow and fast-decay components of fluorescence intensity were considered. There was no picosecond decay on glass, whereas on mixed, small, and large NML, such decay constituted ~70%, 60%, and 97%, respectively, of the amplitude.

Preservation of the optical resolution is important in SMD, because it allows accurate definition of the ROI within a cell. In the example used here, skeletal muscle myofibrils, it is important to place the ROI exactly at the area where myosin cross-bridges interact with actin. This interaction occurs within the area where cross-bridges of thick, myosin containing filaments overlap with thin, actin-containing filaments. The area spans the distance, which depends on the

resting length of the muscle but is typically of the order of the optical resolution of the microscope (43, 44).

Taken together, the data presented in this specific aim demonstrate that surface plasmon coupled emission can be used to decrease the detection volume while silver island films and metal nanoparticles can be used to study single cross bridge in muscle as they significantly decrease photobleaching.

CHAPTER VII

CONCLUSION

Familial hypertrophic cardiomyopathy (FHC) is a genetic disease characterized by left ventricular (LV) hypertrophy and myofibril disarray (5). LV diastolic dysfunction is common and contributes importantly to congestive heart failure. This is known to occur because the ventricles become relatively rigid. Due to this, the ventricles cannot relax completely during diastole, and as a result the ventricles may not fill to the maximum capacity, causing blood to accumulate in the body's organs (primarily the lungs). This abnormal stiffening of the ventricles, and the resulting abnormal ventricular filling during diastole, is referred to as diastolic dysfunction. When diastolic dysfunction is sufficient to produce pulmonary congestion (that is, a damming up of blood into the lungs), diastolic heart failure is said to be present. The diagnosis of diastolic heart failure, unfortunately, is often missed by physicians. This is due to the fact that once the patient presenting with diastolic heart failure has been stabilized, unless the doctor looks specifically for evidence of diastolic dysfunction on the echocardiogram, the heart can appear entirely normal.

This study was designed to examine the molecular and functional consequences of the D166V mutation in the human ventricular myosin RLC, which has been shown to cause malignant FHC phenotype. This mutation was the last identified RLC mutation associated with FHC, and it has never been studied *in vitro* or in transgenic animal models. The mutation occurs at the last amino acid residue of the human cardiac RLC, and the negatively charged and polar aspartic acid residue is replaced by the hydrophobic valine. The mutation lies in the “elbow” of the myosin lever arm, the region of the myosin heavy chain that in the crystal structure makes a

sharp bend and interacts with the N and C termini of RLC. It is well accepted that the role of the myosin lever arm is to amplify the small conformational changes that occur at the nucleotide- and/or actin-binding sites of the myosin head into the large changes that ultimately result in directed movement, sarcomeric shortening, and force generation in muscle.

Transgenic mouse cardiac myofibrils were examined during contraction to study the influence of this mutation on the cross bridge kinetics. Due to its simplified and organized nature, skeletal myofibrils were first used to study the rotation of actin monomers and the duty cycle (the fraction of the total cross-bridge cycle that myosin spends attached to actin in a force generating state). Based on the experiments, it was established that individual molecules can be studied in working muscle. Also, it was proven that observation of actin orientation was an accurate way of measuring cross bridge kinetics. Experiments on duty cycle determined the fraction of the total cross-bridge cycle that myosin spent attached to actin in a force generating state. The results suggested that in isometrically working muscle, cross-bridges spend about half of the cycle time attached to actin. It was seen that $1/tc$ was much smaller than ATPase rate suggesting that the bulk of the energy of ATP hydrolysis was being used for purposes other than performance of mechanical work. Further experiments on cardiac myofibrils from transgenic wild type and mutated mice revealed a stark contrast in the cross bridge cycle between the two. The functional consequences of the D166V mutation was seen to be manifested in the skinned ventricular muscle fibers by largely affecting the kinetics of myosin cross-bridges and slowing the rate of dissociation of the myosin heads from actin.

One can hypothesize that the lever arm swing is inhibited by steric interference originating from the valine residue that replaces the negatively charged aspartate in the mutant heart muscle. Being hydrophobic and C- β branched, valine introduces more bulkiness near the

protein backbone and puts restrictions in the conformations the main chain can adopt. Perhaps the negative charge of the aspartic acid is necessary for the elbow of the myosin lever arm to efficiently execute its swinging motion, enabling the power stroke, and replacement of this residue with a bulky valine prevents the efficient interaction of myosin with actin. Consistent with this notion, the measurements of maximal ATPase showed a large decrease in the mutant fibers compared with controls.

Interestingly, data from another group from the University of Miami revealed that the aspartate to valine substitution resulted in a decreased level of RLC phosphorylation (81). This could be due to a decrease in Ca^{2+} binding to the D166V RLC mutant compared with the WT. Studies on another mutation in the regulatory light chain, E22K, showed a similar decrease in Ca^{2+} binding (38). This consistent behavior among RLC mutations leads one to the hypothesis that perhaps the Ca^{2+} -free conformation of the RLC decreases the accessibility of serine 15, the residue on RLC that is the site for myosin light chain kinase (MLCK) phosphorylation. As proposed in another study, a proper balance of RLC phosphorylation is required for proper cardiac function and is a major determinant of the stretch activation response in the heart (92). Earlier studies indicate that RLC phosphorylation affects cardiac muscle contractility by significantly accelerating the stretch activation response (90). Perhaps the aspartate to valine substitution alters the stretch activation response by decreasing the phosphorylation of RLC.

As has been shown in this proposal, the D166V mutation dramatically decreased the kinetics of myosin cross bridges. This change may be subsequently communicated to the thin filament proteins, leading to a large increase in the myofilament calcium sensitivity. One can speculate that a slower relaxation rate of the myosin cross-bridges would promote the strongly bound state and facilitate the movement of tropomyosin and troponin on actin, promoting the

“close” to “open” transition and the interaction of myosin with actin. A decrease in cross bridge kinetics would, therefore, directly result in increased calcium sensitivity.

The model by Huxley and coworkers state that the central function of the myosin cross-bridge is to undergo a conformational change that move actin past myosin – the “power stroke” (43). According to their study, the crystal structures of the myosin cross-bridge fall into two classes depending on whether the relay helix has a kink at its middle point or not. The kink produced in the relay helix leads to a rotation of the distal end of the relay helix that rotates the attached converter domain through about 60°. The rotation of the converter in turn leads to a 60° rotation of the lever arm. Removing the kink causes the lever arm to rotate back by 60°, which is the elementary structural event in the power stroke. Conversely, creating the kink is the priming action necessary to reach the start of the power stroke. They establish the fact that the hydrolysis of ATP powers the cyclical interaction of the cross-bridge with the actin filament. Physiological studies established that the cross-bridges work as independent force generators and that the stroke of each rowing action was about to 10nm.

In agreement with the model of Huxley and coworkers, we show that the myosin cross bridges can directly affect the regulation of force development in the heart muscle. Consequently, any mutation that would affect the cross-bridge kinetics by increasing or decreasing the rate of cross-bridge dissociation from actin would result in changes in the regulation of force development and cardiac muscle contraction. One can also anticipate that these mutation-induced alterations in cross-bridge kinetics most likely trigger a series of pathological responses resulting in abnormal regulation of cardiac muscle contraction (changes in myofilament calcium sensitivity and/or force). Depending on the location of the FHC mutation in the myosin head and the type of mutation (change in charge, hydrophobicity, and others), the

end effect on cross-bridge kinetics could be different for different amino acid replacements and in some cases contrary effects could be observed.

As explained above, there are a few potential molecular mechanisms by which the D166V mutation in RLC could decrease myosin cross-bridge kinetics, and these include a charge effect of the FHC mutation (replacement of aspartic acid with a bulky valine) and/or a mutation-dependent decrease in RLC phosphorylation. Several potential D166V mediated factors could contribute to FHC. First, the slow force relaxation rate of the fibers could cause one contraction to start to fuse with the next contraction when heart rates are high, contributing to diastolic dysfunction. Second, a large increase in Ca^{2+} sensitivity could contribute to decreased ventricular filling at high heart rates when the tail end of the first Ca^{2+} transient begins to fuse with the second. If severe enough, these two factors could affect diastolic filling of the heart sufficiently to result in systolic dysfunction, *i.e.*, a decrease in stroke volume. This ultimately would cause the heart to compensate by increasing wall thickness (hypertrophy). The third factor that could result in hypertrophy is a decrease in force per cross-section of muscle caused by a decrease in force per cross-bridge (systolic dysfunction). This would also cause the heart to compensate by increasing wall thickness (hypertrophy). Unfortunately, there is no clinical information available on the individuals affected by the D166V mutation to confirm or disprove the above. However, poor prognosis of patients with the disease and multiple cases of sudden cardiac death reported for the D166V-positive patients suggest that the profound functional and histopathological changes found in transgenic D166V myocardium could account for a malignant FHC phenotype associated with this mutation. The physiological alterations found in the Tg-D166V myocardium will have to be further confirmed *in vivo* to fully understand the D166V-mediated detrimental outcome of FHC.

Future studies would involve exploring other mutations to understand the reason they could lead to the observed pathological symptoms. Studying other mutations would give a broader insight into this disease. Detection of single protein molecules in muscle could help study the rate of Ca^{2+} attachment or detachment, the phosphorylation states of RLC, cross bridge kinetics and the role of ATP in contraction. Small bursts of ATP could be provided using caged ATP that can be dissociated using a UV diode laser and the role of ATP could be observed over time. Application of the above techniques to human patients to aid early detection is a particularly striking advantage of this proposal. Biopsy, not necessarily from the heart, but from any other part of the body would enable one to detect this particular malignant form of the disease.

In the third specific aim, assays were developed to use the information obtained in the first two specific aims for an easier and efficient detection of any mutation mediated change in cross bridge kinetics in human samples. Human patients are normally heterozygous for FHC mutations, so their myosin containing thick filaments will be composed of wild type myosin heads interspersed with FHC mutant heads. Any large observational volume will thus contain a mixture of WT and FHC molecules, making the comparison between kinetics of healthy and diseased muscle impossible. Therefore, the unambiguous determination of myosin cross-bridge kinetics requires that the experiments should be carried out at the level of a single molecule with higher accuracy and efficiency. The use of surface plasmon coupled emission, silver island films and metal nanoparticles were studied to achieve the same. It was seen that surface plasmon coupled emission would aid in easier analysis of cross bridge kinetics as it decreased the detection volume while enhancing the image quality. Both silver island films and metal nanoparticles had an added advantage of decreasing the fluorescence lifetime and decreasing

photobleaching. This would enable longer observation period for a single fluorophore. Development of methods to image a single fluorophore in tissue, along with its application in studying cross bridge kinetics, would have numerous implications in the biological field. It would help monitor ligand-receptor interactions in live cells, involvement of protein molecules in internalization of bacteria by cells, conformational fluctuations of DNA, diagnosis of prion diseases and also in detection of viruses at an early phase of infection.

REFERENCES

1. Aeschbacher, B., Hutter, D., Fuhrer, Weidmann, P., Delacretaz, E and Allemann, Y. (2001). Diastolic dysfunction precedes myocardial hypertrophy in the development of hypertension. *Am J Hypertens.* 14: 106–113.
2. Andersen, P., Havndrup, O., Bundgaard, H., Moolman-Smook, J.C., Larsen, L., Mogensen, J., Brink, P., Børglum, A.D., Corfield, V., Kjeldsen, K., Vuust, J and Christiansen, M.(2001). Myosin light chain mutations in familial hypertrophic cardiomyopathy: phenotypic presentation and frequency in Danish and South African populations. *J Med Genet* 38:e43.
3. Ao, X. and S.S. Lehrer. (1995) Phalloidin unzips nebulin from thin filaments in skeletal myofibrils. *J Cell Sci.* 108: 3397-403.
4. Arakawa, T and Timasheff, S.N. (1985) Theory of protein solubility. *Methods Enzymol.* 114: 49-77.
5. Ashrafian, H., Redwood, C., Blair, E and Watkins H. (2003) Hypertrophic cardiomyopathy:a paradigm for myocardial energy depletion. *Trends in Genetics.* 19: 263-268.
6. Axelrod, D., E.H. Hellen, and R.M. Fulbright. (1992) Total internal reflection fluorescence. *Topics in Fluorescence Spectroscopy: Biochemical Applications.* 3: 289-343.
7. Bagshaw, C.R. *Muscle Contraction*, Chapman & Hall, London, 1982.
8. Baker, J. E., Brosseau, C., Joel, P. B., and Warshaw, D. M. (1992) The biochemical kinetics underlying actin movement generated by one and many skeletal muscle myosin molecules. *Biophys. J.* 82 (4), 2134–2147.

9. Barnett, A., E. Matveeva, I. Gryczynski, Z. Gryczynski, and E. Goldys. 2007. Coupled plasmon effects for the enhancement of fluorescent immunoassays. *Physica B (Amsterdam)*. 394:297–300.
10. Bejsovec A, Anderson P. Functions of the myosin ATP and actin binding sites are required for *C. elegans* thick filament assembly. *Cell*. 1990;60:133–140.
11. Bejsovec A, Anderson P. Myosin heavy-chain mutations that disrupt *caenorhabditis elegans* thick filament assembly. *Genes Dev*. 1988;2:1307–1317.
12. Berger, C.L., J.S. Craik, D.R. Trentham, J.E. Corrie, and Y.E. Goldman, Fluorescence polarization of skeletal muscle fibers labeled with Rhodamine isomers on the myosin heavy chain. *Biophys. J.*, 1996. 71: p. 3330-3343.
13. Binder J et al. (2006) Echocardiography-guided genetic testing in hypertrophic cardiomyopathy: septal morphological features predict the presence of myofilament mutations. *Mayo Clin Proc* 81: 459–467.
14. Borejdo, J. and I. Akopova, Orientational Changes of Cross-Bridges During Single Turnover of ATP. *Biophys. J.*, 2003. 84: p. 2450-2459.
15. Borejdo, J., A. Shepard, D. Dumka, I. Akopova, J. Talent, A. Malka, and T.P. Burghardt, Changes in orientation of actin during contraction of muscle. *Biophys. J.*, 2004. 86: p. 2308-2317.
16. Borejdo, J., A.A. Shepard, I. Akopova, W. Grudzinski, and J. Malicka, Rotation of the lever-arm of myosin in contracting skeletal muscle fiber measured by two photon anisotropy. *Biophys. J.*, 2004. 87: p. 3912-3921.
17. Borejdo, J., and Akopova, I. (2003) *Biophys. J.* 84, 2450-2459.
18. Borejdo, J., Assulin, O., Ando, T., and Putnam, S. (1982) *J. Mol. Biol.* 158, 391-414.

19. Borejdo, J., Gryczynski, Z., Calander, N., Muthu, P., and Gryczynski, I. (2006) *Biophys. J.* 91, 2626-2635.
20. Borejdo, J., J. Talent, I. Akopova, and T. P. Burghardt. 2006. Rotations of a few cross-bridges in muscle by confocal total internal reflection microscopy. *Biochim. Biophys. Acta.* 1763:137–140.
21. Borejdo, J., S. Putnam, and M.F. Morales, Fluctuations in polarized fluorescence: evidence that muscle cross-bridges rotate repetitively during contraction. *Proc. Natl. Acad. Sci.*, 1979. 76: p. 6345-6350.
22. Borejdo, J., Shepard, A. A., Akopova, I., Grudzinski, W., and Malicka, J. (2004) *Biophys. J.* 87, 3912-3921.
23. Borejdo, J., Ushakov, D. S., and Akopova, I. (2002) The essential light chains 1 and 3 rotate differently during muscle contraction. *Biophys. J.* 82, 362a.
24. Borejdo, J., Z. Gryczynski, N. Calander, P. Muthu, I. Gryczynski. Application of Surface Plasmon Coupled Emission to Study of Muscle, *Biophys. J.* 91 (2006) 2626–2635.
25. Born, M. and E. Wolf, *Principles of Optics*. 1975, Oxford: Pergamon Press.
26. Brenner, B., Chalovich Kron, S. J., and Spudich, J. A. (1986) Fluorescent actin filaments move on myosin fixed to a glass surface. *Proc. Natl. Acad. Sci. U.S.A.* 83, 6272–6276.
27. Brenner, B., Chalovich, J. M., and Yu, L. C. (1995) Distinct molecular processes associated with isometric force generation and rapid tension recovery after quick release. *Biophys. J.* 68 (4 Suppl.), 106S–111S.
28. Bukatina, A.E., F. Fuchs, and S.C. Watkins. (1996) A study on the mechanism of phalloidin-induced tension changes in skinned rabbit psoas muscle fibres. *J Muscle Res Cell Motil*, 1996. 3: 365-71.

29. Burghardt, T. P., Charlesworth, J. E., Halsetad, M. F., Tarara, J. E., and Ajtai, K. (2006) *Biophys J* 24, 24.
30. Calander, N., and M. Willander. 2002. Theory of surface-plasmon resonance optical-field enhancement at prolate spheroids. *J. Appl. Phys.* 92:4878–4884.
31. Charron, P., Dubourg, O., Desnos, M., Isnard, R., Hagege, R., Millaire, A., Carrier, L., Bonne, G., Tesson, F., Richard, P., Bouhour, J., Schwartz, K., Komajda, M. (1997) Diagnostic value of Electrocardiography and Echocardiography for Familial Hypertrophic Cardiomyopathy in a Genotyped Adult Population. *Circulation.* 96:214-219.
32. De La Cruz, E., and Pollard, T. D. (1994) *Biochemistry.* 33, 14387-92.
33. Dunn, R.C (1999). Near-field scanning optical microscopy. *Chem .Rev.* 99: 2891-927.
34. E.H. Hellen and D. Axelrod. (1987) Fluorescence emission at dielectric and metal-film interfaces. *Journal of the Optical Society of America B.* 4: 337-350.
35. Eggeling, C., J. Widengren, R. Rigler, and C.A.M. Seidel, Photobleaching of Fluorescent Dyes under Conditions Used for Single-Molecule Detection: Evidence of Two-Step Photolysis. *Anal. Chem.*, 1998. 70: p. 2651-2659.
36. Eigen, M. and R. Rigler. (1994) Sorting single molecules: application to diagnostics and evolutionary biotechnology. *Proc Natl Acad Sci.* 91(13): 5740-7.
37. Eisenberg, E., Hill, T. L., and Chen, Y. (1980) *Biophys J* 29, 195-227.
38. Elliott, P., Blanes, J.R., Mahon, N., Poloniecki, J and McKenna, W. (2001). Relation between severity of left-ventricular hypertrophy and prognosis in patients with hypertrophic cardiomyopathy. *The Lancet.* 357: 420-424.

39. Enjuto, M., Francino, A., Lopez, F., Viles, D., Pare, J and Ballesta, A. (2000) Malignant Hypertrophic Cardiomyopathy Caused by the Arg723Gly Mutation in β -Myosin Heavy Chain Gene. *Journa of Molecular and Cellular cardiology*. 32:12.
40. Fatkin, D., Michael, E., Aristizabal, C.O., McConnell, B., Srinivasan, S., Schoen, F., Seidman. C., Turnbull, D and Seidman, J. (1999). Neonatal cardiomyopathy in mice homozygous for the Arg403Gln mutation in the α cardiac myosin heavy chain gene. *J. Clin. Invest.* 103: 147-153.
41. Forkey, J. N., Quinlan, M. E., Shaw, M. A., Corrie, J. E., and Goldman, Y. E. (2003) *Nature* 422, 399-404.
42. Geddes, C.D., A. Parfenov, I. Gryczynski, J.R. Lakowicz, Luminescent Blinking from Silver Nanostructures, *J. Phys. Che. B* 107 (2003) 9989–9993.
43. Gordon, A. M., A. F. Huxley, and F. J. Julian. 1966. Tension development in highly stretched vertebrate muscle fibres. *J. Physiol.* 184:143–169.
44. Gordon, A. M., A. F. Huxley, and F. J. Julian. 1966. The variation in isometric tension with sarcomere length in vertebrate muscle fibres. *J. Physiol.* 184:170–192.
45. Gryczynski, Z., I. Gryczynski, and J. Lakowicz, Simple apparatus for polarization sensing af analytes. *Opt. Eng.*, 2000. 39(9): p. 2351-2358.
46. Hecht, B., S. B., U.P. Wild, V. Deckert, R. Zenobi, and O.J.F. Martin. (2000) Scanning near-field optical microscopy with aperture probes: Fundamentals and applications. *Journal of Chemical Physics*. 112: 7761-74.
47. Hellen, E.H., K. Ajtai, and T.P. Burhgardt, Myosin head rotation in muscle fibers measured using polarized fluorescence photobleaching recovery. *J. Fluorescence*, 1995. 5: p. 355-367.

48. Higuchi, H., and Goldman, Y. E. (1995) Sliding distance per ATP molecule hydrolyzed by myosin heads during isotonic shortening of skinned muscle fibers. *Biophys. J.* 69 (4), 1491–1507.
49. Hollman, A., Goodwin, J.F., Teare, D., Renwick, J.W. (1960) A family with obstructive cardiomyopathy (asymmetrical hypertrophy). *Br Heart J.* 22:449–456.
50. Hopkins, S.C., Sabido-David, C., Corrie, J.E., Irving, M and Goldman, Y.E. (1998) Fluorescence polarization transients from rhodamine isomers on the myosin regulatory light chain in skeletal muscle fibers. *Biophys J.* 74: 3093-110.
51. Houdusse, A., A.G. Szent-Gyorgyi, and C. Cohen, Three conformational states of scallop myosin S1. *Proc Natl Acad Sci U S A*, 2000. 97(21): p. 11238-43.
52. Hughes, S., McKenna, W. (2005) New insights into the pathology of inherited cardiomyopathy . *Heart.* 91:257-264.
53. Hunter, J., and Chien, K., (1999) Signaling Pathways for Cardiac Hypertrophy and Failure. *NEJM.* 341 (17) 1276-1283.
54. Huxley, A. F. (1957) A hypothesis for the mechanism of contraction of muscle. *Prog. Biophys. Biophys. Chem.* 7, 255-318
55. Ishiwata, S., Shimamoto, Y., Suzuki, M., and Sasaki, D. (2007) Regulation of muscle contraction by Ca²⁺ and ADP: focusing on the auto-oscillation (SPOC). *Adv. Exp. Med. Biol.* 592, 341–358.
56. Itakura, S., H. Yamakawa, Y.Y. Toyoshima, A. Ishijima, T. Kojima, Y. Harada, T. Yanagida, T. Wakabayashi, and K. Sutoh, Force-generating domain of myosin motor. *Biochem Biophys Res Commun*, 1993. 196(3): p. 1504-10.
57. Kron, S. J., and Spudich, J. A. (1986) *Proc. Natl. Acad. Sci USA* 83, 6272-6276.

58. Lakowicz, J. R., J. Malicka, I. Gryczynski, Z. Gryczynski, and C. D. Geddes. 2003. Radiative decay engineering: the role of photonic mode density in biotechnology. *J. Phys. D. App. Physics.* 36:R240–R249.
59. Lowey, S., Waller, G.S and Trybus, K.M. (1993) Function of skeletal muscle myosin heavy and light chain isoforms by an in vitro motility assay. *J. Biol. Chem.* 27: 20414-20418.
60. Lukomska, J., J. Malicka, I. Gryczynski, J.R. Lakowicz, (2004) Fluorescence enhancements on silver colloid coated surfaces, *J. Fluoresc.* 14: 417–423.
61. Lymn, R.W.T., E.W., Mechanism of adenosine triphosphate hydrolysis by actomyosin. *Biochemistry*, 1971. 10: p. 4617-24.
62. Magde, D., E.L. Elson, and W.W. Webb, Fluorescence correlation spectroscopy. II. An experimental realization. *Biopolymers*, 1974. 13(1): p. 29-61.
63. Malicka, J., I. Gryczynski, Z. Gryczynski, J.R. Lakowicz, Effects of fluorophore-to-silver distance on the emission of cyanine-dye-labeled oligonucleotides, *Anal Biochem.* 315 (1) (2003) 57–66.
64. Maron, B., Gardin, J., Flack, J., Gidding, S., Kurosaki, T., Bild, D. (1995) Prevalence of Hypertrophic Cardiomyopathy in a General Population of Young Adults. *Circulation.* 92 :785-789.
65. Matveeva, E., Gryczynski, I., Barnett, A., Goldys, E., Akopova, I., Borejdo, J., and Gryczynski, Z. (2007) *Biophys. J.*
66. Mendelson, R., Morales, M.F. & Botts, J., Segmental flexibility of S1 moiety of myosin. *Biochemistry*, 1973. 12 p. 2250-2255. .

67. Minton, A.P., Molecular crowding: analysis of effects of high concentrations of inert cosolutes on biochemical equilibria and rates in terms of volume exclusion. *Methods Enzymol*, 295: 127-149.
68. Mornet, D., R. Bertrand, P. Pantel, E. Audemard, and R. Kassab, Structure of the actin-myosin interface. *Nature*, 1981. 292(5821): p. 301-6.
69. Muthu, P., I. Gryczynski, Z. Gryczynski, J. Talent, I. Akopova, K. Jain, and J.
70. Borejdo. 2007. Decreasing photobleaching by silver island films: application to muscle. *Anal. Biochem.* 366:228–236.
71. Natan, M. J., and A. L. Lyon. 2002. Surface plasmon resonance biosensing with colloidal Au amplification. In *Metal Nanoparticles*. New York: Marcel Dekker. 183–205.
72. Peyser, L.A., A.E. Vinson, A.P. Bartko, R.M. Dickson, Photoactivated fluorescence from individual silver nanoclusters, *Science* 291 (2001) 103–106.
73. Priori, S.G and Napolitano, C (2006) Role of genetic analyses in cardiology: part I: mendelian diseases: cardiac channelopathies. *Circulation* 113: 1130–1135.
74. Prochniewicz-Nakayama, E., Yanagida, T., & Oosawa, F. (1983) Studies on conformation of F-actin in muscle fibers in the relaxed state, rigor, and during contraction using fluorescent phalloidin. *J. Cell Biol.* 97: 1663-1667.
75. Quinlan, M. E., Forkey, J. N., and Goldman, Y. E. (2001) Kinesin-ADP: whole lotta shakin' goin' on. *Nat. Struct. Biol.* 8 (6), 478–480.
76. Quinlan, M. E., Forkey, J. N., and Goldman, Y. E. (2005) Orientation of the myosin light chain region by single molecule total internal reflection fluorescence polarization microscopy. *Biophys. J.* 89 (2), 1132–1142. Epub 2005 May 13.

77. Reedy, M. C. (2000) Visualizing myosin's power stroke in muscle contraction. *J Cell Sci* 113 (Pt 20), 3551-62.
78. Spindler, M., Saupe, K. W., Christe, M. E., Sweeney, H. L., Seidman, C. E., Seidman, J. G., and Ingwall, J. S. (1998) *J. Clin. Investig.* 101, 1775–1783
79. Sweeney, H. L., and Houdusse, A. (2004) *Philos Trans R Soc Lond B Biol Sci.* 359, 1829-41.
80. Sweeney, H. L., Feng, H. S., Yang, Z., and Watkins, H. (1998) *Proc. Natl. Acad. Sci. U. S. A.* 95, 14406–14410
81. Szczesna, D., S.S. Lehrer, (1993) The binding of fluorescent phallotoxins to actin in myofibrils, *J. Muscle Res. Cell Motil.* 14: 594–597.
82. Tajsharghi H. (2008) Thick and Thin Filament Gene Mutations in Striated Muscle Diseases. *Int J Mol Sci.* 2008 June; 9(7): 1259–1275.
83. Takagi, Y., Homsher, E. E., Goldman, Y. E., and Shuman, H. (2006) Force generation in single conventional actomyosin complexes under high dynamic load. *Biophys. J.* 90 (4), 1295–307. Epub 2005 Dec 2.
84. Takagi, Y., Shuman, H., and Goldman, Y. E. (2004) *Philos Trans R Soc Lond B Biol Sci.* 359, 1913-20.
85. Taylor, K. A., Schmitz, H., Reedy, M. C., Goldman, Y. E., Franzini-Armstrong, C., Sasaki, H., Tregear, R. T., Poole, K., Lucaveche, C., Edwards, R. J., Chen, L. F., Winkler, H., and Reedy, M. K. (1999) *Cell* 99, 421-31.
86. Thomas, D.D. and R. Cooke, Orientation of spin-labeled myosin heads in glycerinated muscle fibers. *Biophys J.* 1980. 32: 891-905.

87. Toprak, E., Enderlein, J., Syed, S., McKinney, S. A., Petschek, R. G., Ha, T., Goldman, Y. E., and Selvin, P. R. (2006) Defocused orientation and position imaging (DOPI) of myosin V. *Proc. Natl. Acad. Sci. U.S.A.* 103 (17), 6495–6499. Epub 2006 April 13.
88. Tregear, R. T., and Mendelson, R. A. (1975) *Biophys. J.* 15, 455-467.
89. Uyeda, T. Q., Kron, S. J., and Spudich, A. A. (1990) Myosin step size. Estimation from slow sliding movement of actin over low densities of heavy meromyosin. *J. Mol. Biol.* 214, 699–710.
90. VanBuren, P. W., Waller, G. S., Harris, D. E., Trybus, K. M., Warshaw, D. M., and Lowey, S. (1994) The essential light chain is required for full force production by skeletal muscle myosin. *Proc. Natl. Acad. Sci. U.S.A.* 91, 12403–12407.
91. Wagner, M., Barylko, B and Albanesi, J.P. Tissue distribution and subcellular localization of mammalian myosin I. *The Journal of Cell Biology.* 119: 163-170.
92. Wang, Y., Xu, Y., Kerrick, W. G. L., Wang, Y., Guzman, G., Diaz-Perez, Z., and Szczesna-Cordary, D. (2006) Prolonged Ca and force transients in myosin RLC transgenic mouse fibers expressing malignant and benign FHC mutations. *J. Mol. Biol.* 361, 286–299
93. Warshaw, D. M., Hayes, E., Gaffney, D., Lauzon, A. M., Wu, J., Kennedy, G., Trybus, K., Lowey, S., and Berger, C. (1998) Myosin conformational states determined by single fluorophore polarization. *Proc. Natl. Acad. Sci. U.S.A.* 95 (14), 8034–8039.
94. Warshaw, D. M., Hayes, E., Gaffney, D., Lauzon, A. M., Wu, J., Kennedy, G., Trybus, K., Lowey, S., and Berger, C. (1998) Myosin conformational states determined by single fluorophore polarization. *Proc. Natl. Acad. Sci. U.S.A.* 95 (14), 8034–8039.
95. Weber, W.H. and C.F. Eagen. (1979) Energy transfer from an excited dye molecule to the surface plasmons of an adjacent metal. *Opt. Lett.* 4: 236-238.

96. Wilson, T., *Confocal Microscopy*, ed. e. T. Wilson. 1990, New York: Academic Press. 1-64.
97. Worthington, C. R., and Elliott, G. F. (1996) Muscle contraction: The step-size distance and the impulse-time per ATP. *Int. J. Biol. Macromol.* 18 (1-2), 123–131.
98. Wu J. Modelling concentric contraction of muscle using an improved cross-bridge model. *Journal of Biomechanics.* 32: 837-848.
99. Yanagida, T., and Ishii, Y. (2003) Stochastic processes in nanobiomachines revealed by single molecule detection. *Biosystems* 71: 233–244.
100. Yanagida, T., Ishijima, A., Saito, K., and Harada, Y. (1993) Coupling between ATPase and force-generating attachment-detachment cycles of actomyosin in vitro. *Adv. Exp. Med. Biol.* 332, 339–347.
101. Yildiz, A., and Selvin, P. R. (2005) Kinesin: walking, crawling or sliding along? *Trends Cell Biol.* 15 (2), 112–120.
102. Yildiz, A., Forkey, J. N., McKinney, S. A., Ha, T., Goldman, Y. E., and Selvin, P. R. (2003) Myosin V walks hand-over-hand: single fluorophore imaging with 1.5-nm localization. *Science* 300 (5628), 2061–2065. Epub 2003 June 5.